UAB
Universitat Autònoma de Barcelona

Dynamics in blended electrode materials for Li-ion batteries: coupling electrochemistry and synchrotron based operando techniques

Dimitrios Chatzogiannakis

Universitat Autònoma de Barcelona

Dynamics in blended electrode materials for Li-ion batteries: coupling electrochemistry and synchrotron based operando techniques

Dimitrios Chatzogiannakis

Doctoral thesis

PhD programme in Materials Science

Directors: Montse Casas-Cabanas

M. Rosa Palacín Peiró

CIC energiGUNE

Institut de Ciència de Materials de Barcelona (ICMAB-CSIC)

2024

ICMAB Institut de Ciència de Materials de Barcelona — Excelencia Severo Ochoa

CSIC Consejo Superior de Investigaciones Científicas

destiNY

CIC energiGUNE — Member of Basque Research & Technology Alliance

Dr. Montse Casas-Cabanas, Scientific Director at CIC energiGUNE and Dr. M. Rosa Palacín Peiró, Research Professor at Institut de Ciència de Materials de Barcelona (ICMAB-CSIC)

CERTIFY

That Dimitrios Chatzogiannakis has carried the work entitled "Dynamics in blended electrode materials for Li-ion batteries: coupling electrochemistry and synchrotron based operando techniques" under their direction. This dissertation is presented to be publicly examined for the degree of Doctor awarded by the Universitat Autònoma de Barcelona.

Barcelona, November 5th 2024

Dr. Montse Casas-Cabanas *Dr. M. Rosa Palacín Peiró*

To Ariadne and Athena

Acknowledgements

First and foremost, I would like to express my deep gratitude to Prof. Rosa Palacin and Dr. Montse Casas for their guidance and supervision throughout my thesis journey. I hugely appreciate their scientific insights, but what I value even more is the support they offered during challenging times, which turned my entire PhD experience into a rewarding and enjoyable journey. Thanks to their encouragement, I never once questioned my decision to embark on this path, and I feel truly honoured to have had the opportunity to work alongside such remarkable scientists, mentors, and inspiring women.

Then, I deeply thank the whole DESTINY consortium, not only for the funding but also the connections it helped me make through our meetings and trainings. A large thank you goes to Prof. Christan Mansquelier, Beatrice Messana, Louise Vrand and the rest of scientific and administrative team.

Furthermore, I would like to thank the team from UMICORE, mainly Dr. Violetta Arszelewska, Dr. Pierre-Etienne Cabelguen and Dr. Jeremie Auvergniot for their scientific insights but also for them hosting me in the UMICORE premises in Olen where I got to experience my field from a different perspective.

I also want to extend a special thanks to the two students I had the pleasure of supervising during their internships at ICMAB, Georgia Giannadaki from the University of Crete and Ion Ghilescu from Sorbonne University contributed significantly to Chapter 5 of this thesis, and I am deeply grateful for their hard work. I hope they gained valuable knowledge and positive memories from our collaboration, and I wish them every success in their future plans.

I am deeply honoured to have such esteemed scientists on my jury committee—individuals whose work I have long admired. My heartfelt thanks go to Prof. Jean-Marie Tarascon, Dr. Sandrine Lyonnard, and Dr. Carlos Frontera for dedicating their time to review my work and for accepting to be part of my committee.

I also owe a huge thank you to everyone at CIC and ICMAB who made these past three years in Spain unforgettable and full of joy. Thank you for the shared science, trips, coffee breaks, discussions, meals, and every moment in between. Additionally, I want to express my gratitude to everyone back in Greece who supported me through countless "over the internet" conversations. Your encouragement was invaluable.

Last but not least, I want to thank my family for always being there, supporting my every decision, and guiding me whenever needed. I will never be able to repay them for that. A special apology goes out to little Ariadne and Athena, my nieces, who had their uncle away during the first years of their lives. This thesis is dedicated to them.

Summary

Blending different active materials in the same electrode is an empirically based strategy used in commercial Li-ion batteries for electric vehicles, the aim being to achieve better performance than what can be attained with a single component thanks to the so called "synergistic effects". Yet, fundamental understanding of these synergistic effects has progressed at a slower pace.

The main aim of this thesis has been to get further understanding of interaction between components and specific contributions to the performance of blended electrodes by combining advanced electrochemical methods ("decoupled blend setup" specifically designed which involves the use of a three electrode cell, with two short-circuited working electrodes each containing one of the blend component) to operando (mostly synchrotron X-ray diffraction, XRD and absorption, XAS) characterization. The focus has been placed on both the development of methodologies and experimental protocols and the study of a range of materials already present in commercial batteries, mostly at the positive electrode.

Electrodes comprising equivalent amounts of lithium-ion battery active materials, namely $LiNi_{0.5}Mn_{0.3}Co_{0.2}O_2$ (NMC), $LiMn_2O_4$ (LMO), $LiFe_{0.35}Mn_{0.65}PO_4$ (LFMP) and $LiFePO_4$ (LFP)) have been studied. The distribution of current between blend components was followed during continuous and pulsed charge and discharge processes. Pulsed decoupled electrochemical testing reveals the exchange of charge between blend components during relaxation, which has also been captured through time-resolved operando XRD. The directionality and magnitude of the charge transfer were found to depend on the nature of the components and the cell SoC, being also influenced by temperature. These findings can be rationalized considering both thermodynamics (voltage profile) and reaction kinetics of the blend constituents and contribute to advancing the understanding of internal dynamics in blended electrodes.

Mixtures of LMO and NMC in different amounts have been also studied in more detail, with the composition containing 25% LMO exhibiting the best electrochemical

performance. The effective current load on each blend component can be significantly different from the nominal rate and also varies as function of SoC. Operando studies enabled to monitor the evolution of oxidation state and changes in the crystal structure, which are in agreement with the expected behaviour of the individual components considering the material specific effective current loads.

Blends containing lithium rich manganese rich layered oxides (LRO), which exhibits a significant irreversible capacity upon the first cycle, have been also studied. Mixing with delithiated LFP enables to mitigate this aspect while at the same time improving thermal stability.

Finally, the methodology has been also extended to silicon/graphite blends, which are starting to be implemented at the negative electrode in commercial Li-ion cells. As silicon and graphite exhibit very different capacities, the effective C-rate of graphite can be significantly higher than the nominal rate, especially during the delithiation process.

Since the blend components have different potential vs. capacity profiles, direct reaction between them to reduce/oxidize to achieve equilibrium is possible. Differences in reaction kinetics can lead to complex situations in which both compounds contribute to the overall capacity at a given potential, especially at high rates, and internal lithium redistribution between components takes place during relaxation periods.

The findings reported in this thesis should contribute to achieve a better understanding of lithium dynamics in blended electrodes and help in its rational design and achieve optimal performance to match application requirements.

Table of Contents

1. General Introduction

1.1 Introduction to Lithium-Ion Batteries

Lithium-ion batteries were commercialized by Sony in 1991 [1] and the Nobel Prize in Chemistry was awarded in 2019 for its development to three pioneers in the field (John B. Goodenough, M. Stanley Whittingham and Akira Yoshino). [2] The concept relied on previous research on intercalation chemistry in the 1970s and was a natural evolution from a concept based on the use of lithium metal as the negative electrodes, which turned out to exhibit safety concerns due to dendritic growth of lithium upon sustained cycling under certain conditions.

The structure of a lithium-ion battery is comprised of three main parts: two electrodes (positive and negative) separated by an electrolyte (see Figure 1.1). In the most usual case, the electrolyte of the cell is liquid, and a solid porous separator is also introduced to prevent physical contact between electrodes. Their principle of operation relies on the different redox potentials of the electrodes which also dictate the cell's voltage. During discharge, the chemical species at the negative electrode are oxidized, releasing electrons that can only flow through an external circuit providing electrical current and are consumed by the chemical species at the positive electrode. For every electron that goes through the external circuit, an equivalent amount of positive charge, carried in the form of ions, is consumed in order to balance charges. The amount of charge produced, i.e. the capacity, is usually expressed in Ah.

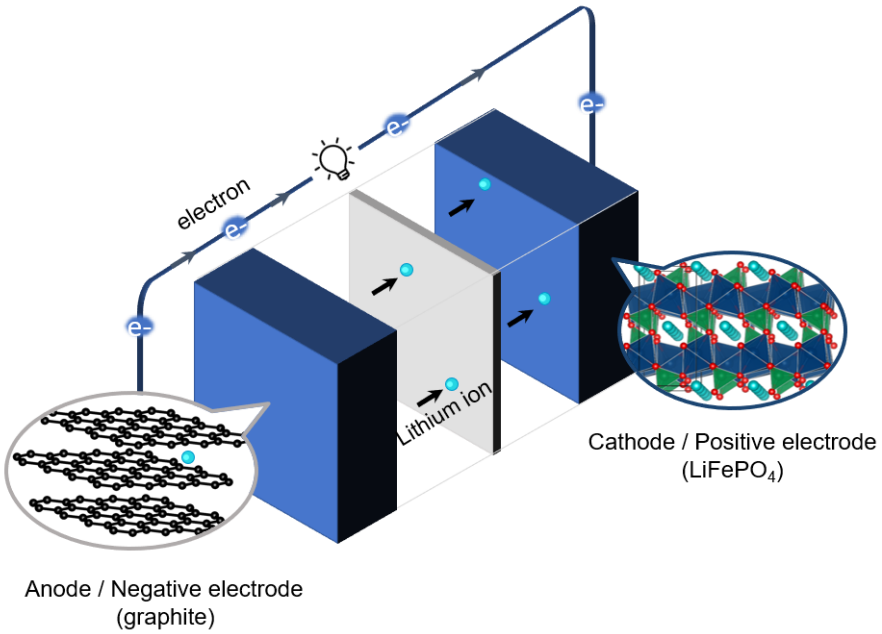

Figure 1.1: Schematic illustration of an LFP Li-ion battery cell.

Nowadays Li-ion batteries are ubiquitous. Since their commercialization, they have been the primary power source of personal electronics such as smartphones, tablets, laptops, and wearables. They are also very popular with small industrial equipment such as cordless tools and in 2021 sales were ca. 440,000 MWh energy with a value of around 76,000 million euros. [3] Besides their application in consumer electronics, they have already entered the field of electric transportation and are now considered for grid storage. The change in application field comes with a change in scale from the ca. 10 Wh of a single cell powering a portable phone or the 50-100 Wh of few cells powering tablets and laptops, to the kWh in electric vehicles or even MWh as the Tesla battery installed in Australia.[4] This brings in additional requirements, not only in terms of performance (capacity, power, etc.), but also with respect to cycle life and cost, and the ability to operate in different environments (e.g. with respect to temperature).

1.2 Electrode Materials and Performance Challenges

In the first generation of cells active materials were $LiCoO_2$ for the positive electrode and coke as the negative one, with a solution of $LiPF_6$ in a mixture of diethyl carbonate and propylene carbonate as the electrolyte.[5] Advances in the field resulted in the substitution of coke by graphite concomitant to the adoption of a new electrolyte formulation where propylene carbonate, that co-intercalated into graphite with lithium causing its exfoliation, was substituted by ethylene carbonate.[6]

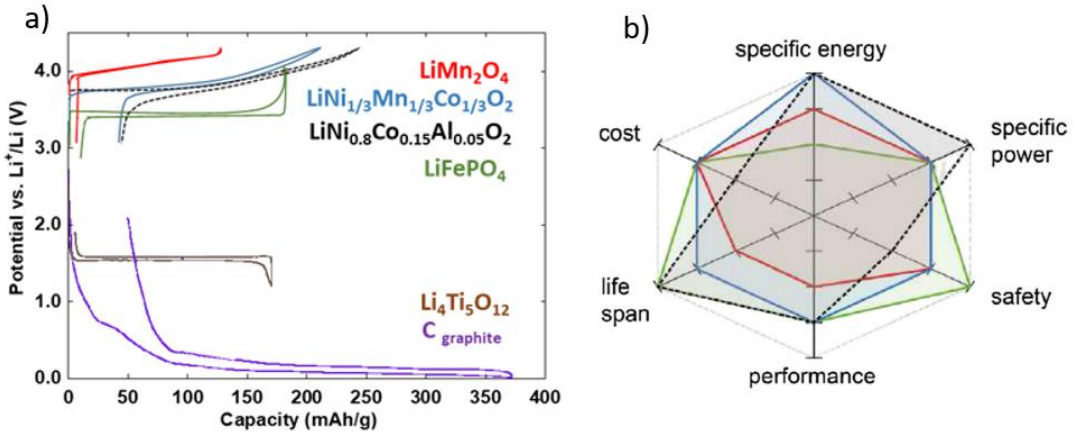

Figure 1.2: (a) Specific capacities and (b) performance comparison of popular electrode materials

Their improvement in performance of Li-ion batteries was fostered by the development of the consumer electronics market, [7] coupled with research in new materials.[8], [9] The spectrum of compounds used in commercial cells has expanded and several families of Li-ion batteries exist, employing different electrode active materials, each with different advantages (see Figure 1.2b).

Graphite still nowadays remains the most widely used negative electrode material in commercial cells, even though the recent addition of a few percent of silicon to enhance capacity is not uncommon. To this day the development of electrodes with large amounts of silicon remains a challenge in the field, as their high capacity (around 3500 mAh/g, associated to the formation of $Li_{15}S_4$) involves important volume changes at each charge/discharge cycle of the battery, which induce significant capacity fading.[10] This

can be alleviated by a number of strategies involving not only electrode formulation aspects [11], [12] but also prelithiation.[13]

On the positive side, the spectrum of materials used commercially is larger, and in all cases involve transition metal oxides for which redox activity is related to topotactic reversible intercalation of lithium ions in the crystal structure, which can proceed through the formation of a solid solution or involve phase transitions. [14]

$LiNi_{1-y-z}Mn_yCo_zO_2$ phases (typically denoted NMCxyz) or $LiNi_{1-y-z}Co_yAlzO_2$ (NCA) are commonly used as an alternative to $LiCoO_2$. They also exhibit a layered crystal structure but are able to deliver larger capacities (over 200 mAh/g) and the lower content of cobalt coupled to the presence of unexpensive manganese contributes to reduce materials costs, which is relevant for some fields of application (e.g. electric vehicles).[15] Alternatively, spinel $LiMn_2O_4$ (LMO) has also been considered as a positive electrode,[16], [17] having the advantage of lower price and toxicity but the drawback of a lower capacity (120 mAh/g) and higher capacity fading due to manganese dissolution, which is promoted by traces of HF that may be present in the electrolyte due to hydrolysis of PF_6^- caused by water impurities.[18], [19] $LiFePO_4$ (LFP) is another material commercially used that, despite its lower operation potential and capacity (see Figure 1.2a) is appealing because of its enhanced stability and lower cost, with partial substitution of iron with manganese ($LiFe_{1-x}Mn_xPO_4$ (LFMP)) resulting in higher average operation potential.[20], [21]Currently, NMC and LFP dominate most of the market share, although there are notable regional differences: in Europe, 99% of the market is covered by NMC, while in China, 58% is held by LF(M)P. This trend is expected to persist into 2030, with growing shares of LF(M)P and Na-ion batteries, particularly in China.[15]

1.3 Emergence of Blended Electrode Materials

With the field of application for Li-ion batteries widening, efforts are being devoted to optimizing performance to match specific use requirements as well as possible. One of the concepts gaining increasing attention for electric vehicle applications is the development of batteries with positive electrodes that consist of a physical mixture (blend) of different electrode active materials. This simple, empirically driven approach, aims to achieve better performance than what can be attained with a single component system by harnessing the "synergies" between multiple materials. While relatively common for primary batteries, its implementation for rechargeable Li-ion cells was suggested for the first time in 2001 by NEC corporation [22] as a way to improve the capacity retention of LMO through mixing with $LiNi_{0.8}Co_{0.2}O_2$*, which would create an alkaline local pH hence preventing manganese dissolution which, as mentioned above, is promoted by acidic impurities. Despite this strategy quickly deserved attention from battery manufacturers, the study of fundamental redox mechanisms for these electrodes did not attract the interest of the scientific community. Even if a few meaningful studies were carried out by relevant groups in the field, mainly addressing the manganese dissolution issue [23], [24], a review published in 2014 [25] by researchers at Ford Motor Company mentions only ca. 15 studies on blends.*

While blends are also commonly used at the negative electrode (typically graphite with a few weight percents of silicon, as mentioned above), this represents a different scenario. The motivation for using blends on the positive side extends beyond enhancing cycle life, as aims also at improving power performance and volumetric energy density. For transport applications, for instance, a common approach is to mix low cost $LiMn_2O_4$*, known for its good power performance, with NMC or NCA, which exhibit slower kinetics but offer higher capacity, come at higher cost and have more limited thermal stability.*

The widespread use of this approach can be inferred from ageing studies reported in commercial cells used in automotive applications. [26], [27], [28] Figure 1.3 depicts some examples of Li-ion cells with different geometries used in a range of different

commercialized electric vehicles in 2018, all using graphite at the negative electrode and binary or even ternary blends at the positive electrode. [29]

Cell format	Cell chemistry		Cell configuration and characteristics				Battery size and range		Cell use
	Anode	Cathode	Capacity (Ah)	Voltage (V)	Specific energy ($Wh\,kg^{-1}$)	Energy density ($Wh\,l^{-1}$)	Energy (kWh)	Driving range (km)	OEM and model[a]
Prismatic cells									
Li Energy Japan	C	LMO–NMC	50	3.70	109	218	16	160	Mitsubishi i-MIEV (2008)
Samsung SDI	C	LMO–NMC	63	3.65	172	312	24	140	Fiat 500e (2013)
Samsung SDI	C	LMO–NCA–NMC	60	3.70	122	228	22	130	BMW i3 (2014)
Samsung SDI	C	LMO–NCA–NMC	37	3.70	185	357	36	300	VW e-Golf (2016)
Samsung SDI	C	LMO–NCA–NMC	94	3.70	189	357	33	183	BMW i3 (2017)
Pouch cells									
AESC	C	LMO–NCA	33	3.75	155	309	24	135	Nissan Leaf (2010)
LG Chem	C	LMO–NMC	16	3.70	-	-	35.5	160	Ford Focus EV (2012)
LG Chem	C	LMO–NMC	36	3.75	157	275	26	150	Renault Zoe (2012)
AESC	C	LMO–NCA	40	3.75	167	375	30	172	Nissan Leaf (2015)

[a]Year in brackets indicates start of production. C, graphite; LMO, $LiMn_2O_4$; NMC, $LiNi_{1-x-y}Co_xMn_yO_2$; NCA, $LiNi_{1-x-y}Co_xAl_yO_2$; OEM, original equipment manufacturer.

Figure 1.3: Overview of LIB cell chemistries and characteristics of cells and batteries for EVs. Adapted from ref. [29]

The lack of fundamental studies in the early days of commercialisation of batteries using blended positive electrodes may be justified by the fact that the study of pure compounds is better suited to elucidate structure-property correlations. Moreover, demonstrating and analyzing the interaction between components can be challenging and had to be inferred from indirect measurements including both electrochemical tests and post-mortem studies. This scenario was improved by the seminal work by Heubner et al. [30] who reviewed the topic from a fundamental point of view and provided not only a background but also new methodologies to assess the study of blended electrodes.

1.4 Study of lithium dynamics

Blended electrodes consist of two (or more) active materials in direct contact, each with different redox potentials and voltage curves, which may interact electrochemically to achieve equilibrium. Clearly distinguishing the contribution of each component to the electrode capacity is only feasible if their redox potentials differ significantly (e.g. hundreds of mV) and low current is flowing through the electrode. However, even for active materials with distinct redox potentials, differences in their reaction kinetics can lead to more complex situations. At high operation rates, both components may contribute to the overall capacity at a given potential, and internal lithium redistribution between components can occur during relaxation periods (see Figure 1.4). [31] This phenomenon, often termed "buffer effect", arises when an active material with fast reaction kinetics will preferentially get oxidized/reduced at high rates, driving the potentials of the two components away from a common equilibrium potential. During relaxation, lithium redistribution will take place to reach equilibrium.

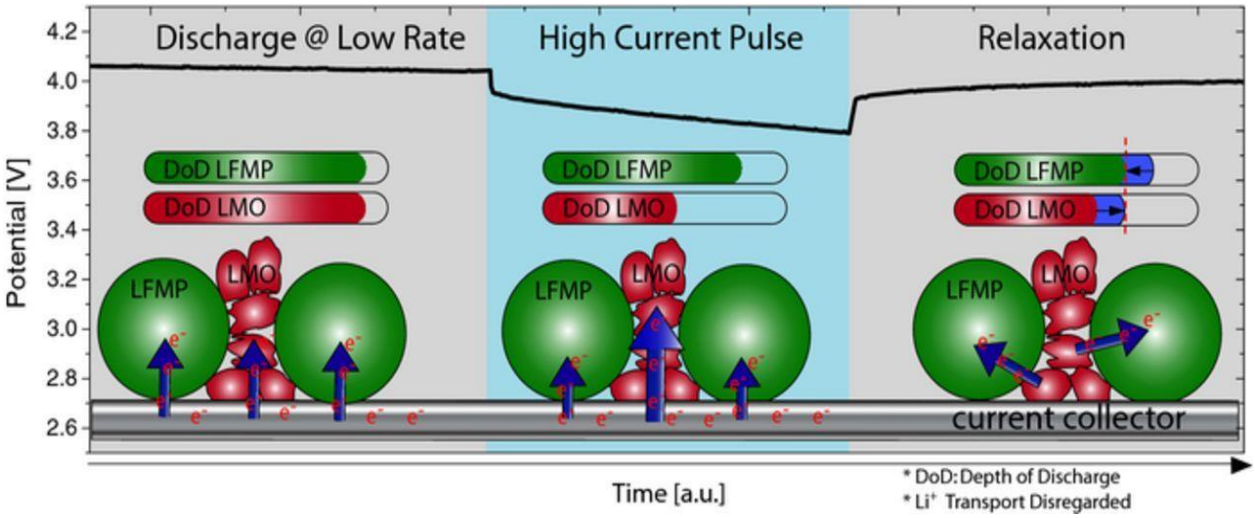

Figure 1.4: Schematics of the buffer effect between LMO and LFMP at different currents. [32]

Exchange of lithium between the blend components takes place within the electrode, as these are in contact. Yet, a very useful setup enabling its direct assessment was developed by Heubner et al. [33] adapted from galvanic corrosion studies, which they termed "model-like blend" and consisted of a three electrode cell, with two short-

circuited working electrodes, each one containing one of the blend components. The current/potential was monitored with a potentiostat between the counter and the working electrodes, while the "short-circuiting" current between the two working electrodes was measured with a Keithley 2100 multimeter (see Figure 1.5). Within the framework of this thesis, it was deemed appropriate to denote the setup as "decoupled blend" instead. Understanding both the contribution of each component to the electrode capacity and the processes of lithium redistribution remain under-researched but is essential for the rational design of blended electrodes.

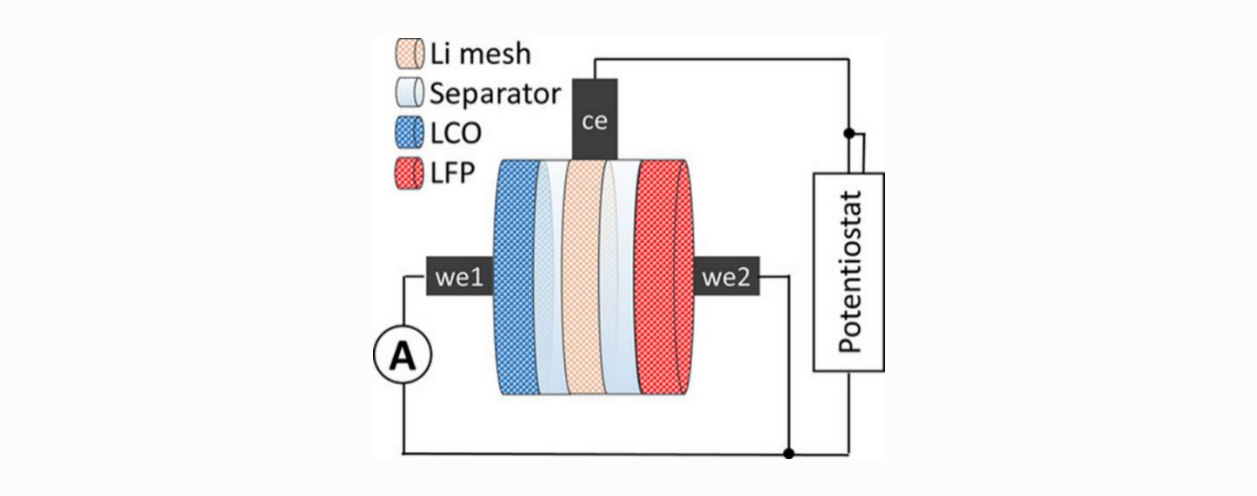

Figure 1.5: Schematic representation of the decoupled blend setup used by Heubner et.al. showing a single counter electrode (orange) against two working electrodes (blue and red).

Aside measuring contributions of each individual blend component to the cell current during operation at different rates and subsequent relaxation, the setup was also used to address thermo-electrochemical behaviour. Indeed, lithium redistribution between blend components can also be triggered by a temperature change.[34] While the Gibbs energies of the two constituents are identical at equilibrium, an increase in temperature will modify them to a different extent, the magnitude being related to the entropy coefficient for each compound. This will result in lithium extraction from the compound with lower Gibbs energy and insertion in the one with higher Gibbs energy. The opposite effect will take place for decreasing temperature, with the magnitude of the current being non negligible (4 mA/g resulting from a 20° temperature change for

LCO/LMO blends for instance), and hence relevant for thermal management in electric vehicles. Indeed, this effect will impact the cell not only during self-heating caused by battery operation but also during parking and related to ambient temperature changes, even when cars are parked. While the magnitude of the current under different operation conditions and different blend compositions remains to be investigated, it is clear that it may have potential implications in cycle as well as shelf life. Moreover, ambient conditions, self-heating of the electrode/battery during operation and/or the use of cooling/heating systems could be much more significant for blended than for single constituent electrodes.

Operando measurements are also useful tool to study blended electrodes. Indeed, and besides the intrinsic advantages in terms of characterizing the materials during real operation in the cell, thus avoiding the risk of materials evolving or being contaminated during cell disassembly and sample preparation procedures [35], they enable the indirect monitoring of the evolution of individual blend components, which can be correlated to operation conditions. X-ray diffraction (XRD) is most useful to that respect, as it enables to follow structural changes associated to redox operation (phase composition and evolution of the cell parameters), with X-ray absorption (XAS) being an ideal complement, probing changes in the transition metal oxidation states. Synchrotron X-ray sources allow performing time-resolved experiments at high rates with good signal-to-noise ratio in only a few minutes, and allow for fast data acquisition probing either a single cell or several cells sequentially. [36] While the influence of the beam in the electrochemical reaction itself is not to be disregarded [37], [38], [39], coupling of different techniques in a multi-modal approach is currently the focus of intense activities with the objective of accelerating progress in battery research [40], one of the main hurdles being data processing. In the case of XRD for instance, Rietveld refinement procedures require manual user intervention and are time consuming. Yet, novel tools are being developed, such as the FullProfApp [41] that enable to accelerate

data analysis beyond the traditional pattern-to-pattern analysis, which will likely become of general use in the near future.

1.5 Objectives and Structure of the Thesis

In the context of the aforementioned state of the art, the PhD project that resulted in the present doctoral thesis was defined in the framework of the DESTINY PhD Programme: "Doctorate Programme on Emerging Battery Storage Technologies Inspiring Young Scientists" (https://www.destiny-phd.eu/ H2020-MSCA-COFUND-2019, GA 945357). This initiative originated from the ALISTORE-ERI (https://www.alistore.eu/), and the present PhD is a collaborative effort between CIC energiGUNE and ICMAB-CSIC, with the participation of UMICORE. The latter provided the applied industrial perspective, hosted the PhD candidate for an internship at their premises and supplied state-of-the-art battery grade pre-commercial materials ("lithium rich, manganese rich" layered oxides, denoted as LRO) giving thus an added practical value to the project outcome.

The main aim of this PhD thesis is to get further understanding of synergistic effects between components and their specific contributions to the performance of blended electrodes. This was achieved by combining advanced electrochemical methods and operando characterization, with a focus on both the development of methodologies and experimental protocols, as well as the study of various materials already present in commercial batteries, mostly at the positive electrode. The research plan involved the specific objectives described below:

i) Develop simplified working protocols to conduct experiments using the methodology developed by Heubner et al.. This will allow experiments to be performed with two channels of the same potentiostat (without the need of an external multimeter other than for validation of procedures). As a result, data can be more easily retrieved, synchronized and processed.

ii) Use operando techniques (mostly XRD) to validate the conclusions derived from the experiments using the "decoupled-blend" setup ensuring that the analysis of

the behaviour of the blend components is representative of the performance in true blended electrodes where the materials are in direct contact.

iii) Apply of the methods developed to study specific blend formulations, with emphasis on positive electrode materials, including blends used in commercial batteries, such as LMO/NMC, as well as new blend formulations which can bring in additional advantages for new materials in the pre-commercial state such as LRO.

iii) Extend the study to negative electrode materials, namely graphite/silicon blends, which are also starting to be used commercially.

This PhD has been carried out in the framework of the Materials Science Doctoral Program at the Universitat Autònoma de Barcelona, and the present thesis is presented as compendium of two publications already published and two additional chapters which constitute drafts of publications to be submitted in the near future.

In particular, Chapter 2 corresponds to the publication "Understanding charge transfer dynamics in blended positive electrodes for Li-ion batteries" (Energy Storage Materials, 69 (2024) 103414.https://doi.org/10.1016/j.ensm.2024.103414) and describes the validation of the developed experimental approaches in six different blend compositions consisting of 50:50 mixtures of different commercial electrode materials. The study highlights how voltage profiles influence current distribution during charge and discharge, and evidences the "buffer effect" among blend components, which depends on factors like operation temperature and state of charge.

Chapter 3 corresponds to the article "Towards understanding the functional mechanism and synergistic effects of $LiMn_2O_4$ - $LiNi_{0.5}Mn_{0.3}Co_{0.2}O_2$ blended positive electrodes for Lithium-ion batteries" (Journal of Power Sources, 591 (2024) 233804.https://doi.org/10.1016/j.jpowsour.2023.233804) and reports studies of LMO:NMC blends in different amounts, observing that the combination enhances energy density and rate capability due to synergistic interactions. The change in effective rate is assessed for each component depending on their ratio, which is also

validated by operando synchrotron XRD and XAS. Chapter 4 corresponds to the study of LRO blended with delithiated active materials, in a strategy aiming at compensating its first cycle irreversible capacity, an approach which has been also found to improve the electrode thermal stability and has recently been object of a patent. Two different materials were assessed (delithiated LFP and LMO) and design guidelines are defined based on the results obtained.

Chapter 5 represents the extension of previous work to apply the "decoupled blend" protocol to silicon/graphite blends and following the behaviour at different temperatures.

Finally, Chapter 6 covers a global discussion of the results obtained in the framework of this PhD together with the main conclusions and perspectives of further work in the topic.

References

[1] T. Nagaura and K. Tozawa, Progress in batteries and solar cells. 1990.

[2] "LITHIUM-ION BATTERIES - Scientific Background on the Nobel Prize in Chemistry 2019." Accessed: Oct. 29, 2024. [Online]. Available: https://www.nobelprize.org/prizes/chemistry/2019/advanced-information/

[3] C. Pillot (Avicenne Energy), "The rechargeable battery market and main trends 2020-2030," in Batteries Event 2022 Lyon, Oct 18 to 21st, Lyon, Oct. 2022.

[4] M. Merano, "150MW/300 MWh Tesla Megapack system in Australia goes live," https://www.teslarati.com/edify-tesla-megapack-150mw-300mwh-system/, Oct. 10, 2023.

[5] Y. Nishi, "The development of lithium ion secondary batteries," Chemical Records, vol. 1, no. 5, pp. 406–413, 2001, doi: 10.1002/tcr.1024.

[6] R. Fong, U. von Sacken, and J. R. Dahn, "Studies of Lithium Intercalation into Carbons Using Nonaqueous Electrochemical Cells," J Electrochem Soc, vol. 137, no. 7, p. 2009, Jul. 1990, doi: 10.1149/1.2086855.

[7] G. E. Blomgren, "The Development and Future of Lithium Ion Batteries," J Electrochem Soc, vol. 164, no. 1, pp. A5019–A5025, 2017, doi: 10.1149/2.0251701jes.

[8] J.-M. Tarascon and M. Armand, "Issues and challenges facing rechargeable lithium batteries," 2001. [Online]. Available: www.nature.com

[9] L. Croguennec and M. R. Palacin, "Recent achievements on inorganic electrode materials for lithium-ion batteries," 2015, American Chemical Society. doi: 10.1021/ja507828x.

[10] D. Larcher, S. Beattie, M. Morcrette, K. Edström, J. C. Jumas, and J. M. Tarascon, "Recent findings and prospects in the field of pure metals as negative electrodes for Li-ion batteries," J Mater Chem, vol. 17, no. 36, pp. 3759–3772, 2007, doi: 10.1039/b705421c.

[11] D. Mazouzi et al., "Critical roles of binders and formulation at multiscales of silicon-based composite electrodes," Apr. 15, 2015, Elsevier. doi: 10.1016/j.jpowsour.2015.01.140.

[12] J. S. Bridel, T. Azaïs, M. Morcrette, J. M. Tarascon, and D. Larcher, "Key parameters governing the reversibility of Si/carbon/CMC electrodes for Li-ion batteries," Chemistry of Materials, vol. 22, no. 3, pp. 1229–1241, Feb. 2010, doi: 10.1021/cm902688w.

[13] W. Porcher and S. Lyonnard, "Extra lithium gives a boost," Nat Energy, vol. 8, no. 7, pp. 649–650, 2023, doi: 10.1038/s41560-023-01287-8.

[14] M. B. Armand, "Intercalation Electrodes," in Materials for Advanced Batteries, J. and S. B. C. H. Murphy D. W. and Broadhead, Ed., Boston, MA: Springer US, 1980, pp. 145–161. doi: 10.1007/978-1-4684-3851-2_7.

[15] C. Pillot and F. Renard, "The Rechargeable Battery Market: Value Chain and Main Trends," in Advanced Automotive Battery Conference Europe, Strasbourg , 2024.

[16] M. M. Thackeray, "MANGANESE OXIDES FOR LITHIUM BATTERIES," 1997.

[17] G. Amatucci and J.-M. Tarascon, "Optimization of Insertion Compounds Such as LiMn2O4 for Li-Ion Batteries," J Electrochem Soc, vol. 149, no. 12, p. K31, 2002, doi: 10.1149/1.1516778.

[18] C. Zhan, T. Wu, J. Lu, and K. Amine, "Dissolution, migration, and deposition of transition metal ions in Li-ion batteries exemplified by Mn-based cathodes-A critical review," Feb. 01, 2018, Royal Society of Chemistry. doi: 10.1039/c7ee03122j.

[19] A. Banerjee et al., "On the oxidation state of manganese ions in li-ion battery electrolyte solutions," J Am Chem Soc, vol. 139, no. 5, pp. 1738–1741, Feb. 2017, doi: 10.1021/jacs.6b10781.

[20] C. Masquelier and L. Croguennec, "Polyanionic (phosphates, silicates, sulfates) frameworks as electrode materials for rechargeable Li (or Na) batteries," Aug. 14, 2013. doi: 10.1021/cr3001862.

[21] A. Yamada, Y. Kudo, and K.-Y. Liu, "Phase Diagram of Li[sub x](Mn[sub y]Fe[sub 1−y])PO[sub 4] (0≤x, y≤1)," J Electrochem Soc, vol. 148, no. 10, p. A1153, 2001, doi: 10.1149/1.1401083.

[22] T. Numata, C. Amemiya, T. Kumeuchi, M. Shirakata, and M. Yonezawa, "Advantages of blending LiNi 0.8 Co 0.2 O 2 into Li 1+x Mn 2-x O 4 cathodes."

[23] A. J. Smith, S. R. Smith, T. Byrne, J. C. Burns, and J. R. Dahn, " Synergies in Blended LiMn 2 O 4 and Li[Ni 1/3 Mn 1/3 Co 1/3]O 2 Positive Electrodes ," J Electrochem Soc, vol. 159, no. 10, pp. A1696–A1701, 2012, doi: 10.1149/2.056210jes.

[24] C. Taubert, H. Y. Tran, M. Fleischhammer, P. Axmann, and M. Wohlfahrt-Mehrens, "LiMn2O4 spinel/LiNi0.8Co 0.15Al0.05O2 blends as cathode materials for lithium-ion batteries," in AABC 2010 - Advanced Automotive Battery Conference, 2010. doi: 10.1149/1.3560582.

[25] S. B. Chikkannanavar, D. M. Bernardi, and L. Liu, "A review of blended cathode materials for use in Li-ion batteries," 2014, Elsevier B.V. doi: 10.1016/j.jpowsour.2013.09.052.

[26] *M. Lang et al., "Post mortem analysis of fatigue mechanisms in LiNi0.8Co0.15Al0.05O2 – LiNi0.5Co0.2Mn0.3O2 – LiMn2O4/graphite lithium ion batteries," J Power Sources, vol. 326, pp. 397–409, Sep. 2016, doi: 10.1016/j.jpowsour.2016.07.010.*

[27] *M. S. D. Darma et al., "The influence of cycling temperature and cycling rate on the phase specific degradation of a positive electrode in lithium ion batteries: A post mortem analysis," J Power Sources, vol. 327, pp. 714–725, Sep. 2016, doi: 10.1016/j.jpowsour.2016.07.115.*

[28] *P. H. Lee, S. huang Wu, W. K. Pang, and V. K. Peterson, "The storage degradation of an 18650 commercial cell studied using neutron powder diffraction," J Power Sources, vol. 374, pp. 31–39, Jan. 2018, doi: 10.1016/j.jpowsour.2017.11.021.*

[29] *R. Schmuch, R. Wagner, G. Hörpel, T. Placke, and M. Winter, "Performance and cost of materials for lithium-based rechargeable automotive batteries," Apr. 01, 2018, Nature Publishing Group. doi: 10.1038/s41560-018-0107-2.*

[30] *C. Heubner, T. Liebmann, M. Schneider, and A. Michaelis, "Recent insights into the electrochemical behavior of blended lithium insertion cathodes: A review," Apr. 10, 2018, Elsevier Ltd. doi: 10.1016/j.electacta.2018.02.165.*

[31] *C. Heubner, T. Liebmann, C. Lämmel, M. Schneider, and A. Michaelis, "Internal dynamics of blended Li-insertion electrodes," J Energy Storage, vol. 20, pp. 101–108, Dec. 2018, doi: 10.1016/j.est.2018.09.003.*

[32] *A. Klein, P. Axmann, and M. Wohlfahrt-Mehrens, " Origin of the Synergetic Effects of LiFe 0.3 Mn 0.7 PO 4 – Spinel Blends via Dynamic In Situ X-ray Diffraction Measurements ," J Electrochem Soc, vol. 163, no. 9, pp. A1936–A1940, 2016, doi: 10.1149/2.0741609jes.*

[33] *C. Heubner, T. Liebmann, C. Lämmel, M. Schneider, and A. Michaelis, "Deconvolution of Cyclic Voltammograms for Blended Lithium Insertion Compounds by using a Model-Like Blend Electrode," ChemElectroChem, vol. 5, no. 3, pp. 425–428, Feb. 2018, doi: 10.1002/celc.201700997.*

[34] *C. Heubner, C. Lämmel, M. Schneider, and A. Michaelis, "Temperature induced compositional redistribution in blended insertion electrodes," J Power Sources, vol. 344, pp. 170–175, 2017, doi: 10.1016/j.jpowsour.2017.01.106.*

[35] *D. Saurel et al., "Experimental Considerations for Operando Metal-Ion Battery Monitoring using X-ray Techniques," Chemistry-Methods, vol. 1, no. 6, pp. 249–260, Jun. 2021, doi: 10.1002/cmtd.202100009.*

[36] *A. P. Black et al., "Synchrotron radiation based operando characterization of battery materials," Dec. 12, 2022, Royal Society of Chemistry. doi: 10.1039/d2sc04397a.*

[37] T. Jousseaume, J. F. Colin, M. Chandesris, S. Lyonnard, and S. Tardif, "How Beam Damage Can Skew Synchrotron Operando Studies of Batteries," ACS Energy Lett, vol. 8, no. 8, pp. 3323–3329, Aug. 2023, doi: 10.1021/acsenergylett.3c00815.

[38] C. K. Christensen et al., "Beam damage in operando X-ray diffraction studies of Li-ion batteries," J Synchrotron Radiat, vol. 30, no. Pt 3, pp. 561–570, Mar. 2023, doi: 10.1107/S160057752300142X.

[39] A. P. Black et al., "Beam Effects in Synchrotron Radiation Operando Characterization of Battery Materials: X-Ray Diffraction and Absorption Study of LiNi0.33Mn0.33Co0.33O2 and LiFePO4 Electrodes," Chemistry of Materials, vol. 36, no. 11, pp. 5596–5610, Jun. 2024, doi: 10.1021/acs.chemmater.4c00597.

[40] D. Atkins et al., "Accelerating Battery Characterization Using Neutron and Synchrotron Techniques: Toward a Multi-Modal and Multi-Scale Standardized Experimental Workflow," Adv Energy Mater, vol. 12, no. 17, May 2022, doi: 10.1002/aenm.202102694.

[41] O. Arcelus et al., "FullProfAPP: a graphical user interface for the streamlined automation of powder diffraction data analysis," J Appl Crystallogr, vol. 57, pp. 1676–1690, Oct. 2024, doi: 10.1107/S1600576724006885.

2. Understanding charge transfer dynamics in blended positive electrodes for Li-ion batteries

Dimitrios Chatzogiannakis, Violetta Arszelewska, Pierre-Etienne Cabelguen, François Fauth, Montse Casas-Cabanas, M. Rosa Palacin

Energy Storage Materials, Volume 69, May 2024, 103414

https://doi.org/10.1016/j.ensm.2024.103414

Abstract

This paper investigates the electrochemical behavior of binary blend electrodes comprising equivalent amounts of lithium-ion battery active materials, namely $LiNi_{0.5}Mn_{0.3}Co_{0.2}O_2$ (NMC), $LiMn_2O_4$ (LMO), $LiFe_{0.35}Mn_{0.65}PO_4$ (LFMP) and $LiFePO_4$ (LFP)), with a focus on decoupled electrochemical testing and operando X-ray diffraction (XRD). All possible 50:50 blend combinations were studied and the distribution of current between blend components was followed during continuous and pulsed charge and discharge processes. The results demonstrate the significant impact of the voltage profiles of individual materials on the current distribution, with the effective C-rate of each component varying throughout the State of Charge (SoC). Pulsed decoupled electrochemical testing reveals the exchange of charge between blend components during relaxation, showcasing the "buffer effect", which has also been captured through time-resolved operando XRD experiments in real blends carefully considering beam-induced effects. The directionality and magnitude of the charge transfer were found to depend on the nature of the components and the cell SoC, being also influenced by temperature. These dependencies can be rationalized considering both thermodynamics (voltage profile) and reaction kinetics of the blend constituents. These findings contribute to advancing the understanding of internal dynamics in blended electrodes, offering valuable insights for the rational design of blends to meet the diverse operational demands of lithium-ion batteries.

2.1 Introduction

Transport electrification has resulted in an expansion of the Li-ion battery market from its original scope embracing mostly portable electronics. This has brought up challenges in terms of scale (from Wh to kWh storage) which involve not only building larger cells but also their assembly in modules and packs. These are controlled by a Battery Management System (BMS) to ensure safe and reliable operation while also mitigating performance loss as much as possible. Aside improvements in cell size and cycle life, additional battery requirements brought up by the advent of electric vehicles are related to performance indicators (e.g. in terms of power), enhancement of sustainability and decrease of cost.

Blending different active materials in the same cell electrode, an empirical approach commonly used for primary cells has been readily applied to commercial EV Li-ion batteries, mostly on the positive side [1], despite unfortunately receiving rather low attention at the fundamental research level. The global aim is to promote positive synergetic effects between the different electrode components (typically $LiMn_2O_4$ and layered $LiMO_2$ with M consisting of Ni, Co and Mn or Al). Several different strategies have been identified to achieve this goal.

On the chemical side, and as pointed out by Numata et al. (NEC corporation) more than 20 years ago [2], the capacity fade in $LiMn_2O_4$ caused by manganese dissolution related to acid leaching could be alleviated by blending with $LiMO_2$. The underlying rationale behind is that the basicity of $LiMO_2$ would help in mitigating the presence of hydrofluoric acid (HF) in the electrolyte, which can result from hydrolysis of PF_6

anions present in the electrolyte caused by H_2O impurities. In addition to that, the presence of $LiMn_2O_4$ would contribute to decrease the total amount of cobalt in $LiMO_2$ electrodes, hence improving both battery cost and environmental footprint. Such compound specific features, which also involve the electrolyte and were also confirmed

by later studies [3–6], exert an influence on thermal behaviour, consequently also impacting safety [6–8].

More generic aspects to be considered are particle sizes and reaction kinetics of the electrode active materials. Improvement in terms of loading density of the casted electrodes can result from tuning the electrode microstructure [9]. One notable example is mixing materials with different particle sizes (not necessarily involving different compositions), a practice that may be common at the industrial level despite it has not been extensively addressed in the scientific literature.

A few studies related to thermodynamics have been carried out [10–14] providing insights into the influence of temperature on the behaviour of the blended electrodes. Reversible heat generation rates are consistent with predictions based on the composition and properties of constituents. Yet, and as a result of the different entropy coefficients of the blend components, temperature changes will induce an internal charge transfer process (i.e. lithium exchange) which will take place even when batteries are at rest, for instance, while vehicles are parked.

Kinetic aspects are considered most relevant for practical application, and their rationalization would help in the design of blended electrodes optimized for operation under specific conditions. Materials with fast reaction kinetics can sustain significantly higher effective rates than the nominal rate applied to the electrode, which is beneficial for applications involving high pulse-like loads such as electric vehicles. Once the pulse is finished, relaxation will induce a redistribution of lithium within the components to reach equilibrium. This rationale has motivated the widespread commercial use of $LiMO_2$: $LiMn_2O_4$ blends. $LiMO_2$, despite having slow kinetics, exhibits high capacity (especially for large amounts of M=Ni). The addition of $LiMn_2O_4$ lowers overall costs while enhancing power performance. Olivine $LiMPO_4$ (M=Fe, Mn) based blends have a lower presence in commercial cells to date but they have also deserved attention at the laboratory scale as they can as well exhibit fast kinetics and are based on low cost

abundant transition metals (See [15] as an example together with general review papers [16, 17]).

The study of interactions rooted in different kinetics (improvement of electrode rate capability sometimes referred to as "buffer effect") has significantly progressed in recent years thanks to the approach developed by Heubner et al., adapted from corrosion studies, which enables to separate the current responses from the individual blend components using three electrode cells. [13,18,19]. By using an analogous setup for the study of $LiMn_2O_4$ *:* $LiNi_{0.5}Mn_{0.3}Co_{0.2}O_2$ *blends [17], the effective current load on each blend component was found to be very different depending on SoC and ratio of blended components. This finding was in full agreement with results from operando synchrotron X-ray absorption and diffraction experiments carried out on real blend electrodes where the components are in physical contact [20].*

The present paper aims to broaden the scope by including a wider set of blends, with every binary 50:50 combination of $LiMn_2O_4$ *(LMO),* $LiNi_{0.5}Mn_{0.3}Co_{0.2}O_2$ *(NMC),* $LiFePO_4$ *(LFP) and* $LiFe_{0.35}Mn_{0.65}PO_4$ *(LFMP), well known materials applied in commercial cells and exhibiting not only different kinetics but also different voltage profiles. The above mentioned three electrode cell setup was also used, for both continuous and pulsed galvanostatic experiments, and coupled to timeresolved synchrotron operando X-ray diffraction experiments, to capture and rationalize charge transfer events between blend components as a function of thermodynamical (voltage profile) and reaction kinetics of individual blend components.*

2.2 Experimental details

2.2.1 Decoupled blend study

In order to investigate the effective current loads experienced by each blend component (as opposed to the nominal applied rate) and the amount of charge exchanged during the relaxation steps, the decoupled blend setup developed by

Heubner et al. was used [13]. This setup, which allows mimicking the electrochemical response of a blended electrode while monitoring individual current contributions, is comprised of a three electrode Swagelok cell (perfluoroalkoxyalcane (PFA) body) with two positive working electrodes (each containing one of the blend components) and a third common negative lithium metal counter electrode.

The electrode formulation used consists of 84:8:8 (Active material (Pure or blended): Super P (Thermo Scientific): PVDF (Kureha). $LiMn_2O_4$ (LMO) was purchased from Sigma Aldrich, $LiNi_{0.5}Mn_{0.3}Co_{0.2}O_2$ (NMC) from MTI corp., and $LiFePO_4$ (LFP) and $LiFe_{0.35}Mn_{0.65}PO_4$ (LFMP) from Aleees. N-Methyl-2-Pyrrolidone (NMP)-based slurries were tape casted (250 µm) onto aluminum foil (SAMA), dried at 120°C, and punched into 14 mm discs, calendared at 4 Tons and later further punched to reduce the diameter to 10mm before a final drying at 120°C under vacuum overnight. The electrodes were then transferred to a glovebox (Argon-filled, H_2O < 0.5 ppm, O_2 < 2 ppm) for assembly, ensuring minimal exposure to ambient humidity or oxygen throughout the entire process.

For each cell, two electrodes of the same diameter (10 mm) and areal loading (4–5 mg/cm^2) were selected trying to achieve an active mass ratio as close to 50:50 as possible. The achieved ratios, capacities and 1C specific currents are listed in Table 1 S.I. The cells were first cycled 3 times at a rate of C/10 in the 4.3-3.2 V range, including 1 h long constant voltage steps at the upper and lower cutoff voltages, while recording the current flowing to/from each of the two working electrodes. After a final charge (and 1 h constant voltage step) at C/10 up to 4.3 V, the cells were discharged through 20 pulses at a rate of 3C, each lasting 1 min. After each pulse, the cell underwent a 10 min relaxation period in OCV (Open Circuit Voltage), with the current flowing between the electrodes containing the individual blend components being measured both during the pulse and the relaxation. To have a consistent protocol for all the blends, no lower cutoff voltage was used. Before this measurement, no cell had been discharged at voltages lower than 3.2 V.

For the measurements done at 40°C, a recirculating bath (Thermo Scientific) filled with silicon oil was used. After it reached the target temperature, individual zip bags containing the 3 electrode cells, were immersed in the oil where they were left for at least 24 h to thermalize. Afterwards, the same protocols used at room temperature were applied.

2.2.2 Synchrotron X-Ray diffraction

High resolution XRD measurements were carried out at BL-04 (MSPD) beamline of ALBA synchrotron in transmission geometry using a MYTHEN2 high-throughput position sensitive detector. The cells used were specially adapted Hohsen CR2032 coin cells [21] (Institute for Applied Materials - Energy Storage Systems Karlsruhe Institute of Technology), bearing a thin glass window on both sides and a hole on the stainless-steel spacer, but otherwise identical to the standard CR2032 ones. Glass windows (130 μm thick) were selected because of their rigidity and a Kapton disc was placed on the hole of the current collector/spacer [22]. Both contribute to achieving a more homogeneous cell pressure, critical in such experiments at fast rates. The cells were mounted on an 8 coin cell carousel-like holder enabling sequential data acquisition [21] and cycled using a VSP potentiostat-galvanostat (Bio-Logic). The electrodes used in the experiments, each one containing a 50:50 blend, were prepared using the same techniques and materials described in Section 2.1 and treated in the same way differing only in their diameter which was in this case was kept at 14 mm. Their capacities and 1C specific currents are given in Table 2 S.I.

Since beam effects during operando experiments have been previously reported [23–26] precautions were taken to optimize the data acquisition protocol and experiments were done at two different photon energies 15 keV (λ = 0.8265 Å) and 30 keV (λ = 0.4135 Å). Before being mounted on the beamline cell holder, all cells were pre-charged slowly (C/10 for pulsed and C/5 for continuous testing) up to 4.3 V and then kept at constant voltage (CV) for at least 1 h. During continuous discharges, cells were

cycled in parallel while sequentially exposed to the beam to acquirediffraction patterns. This protocol resulted in approximately 6 min intervals between two successive paterns on each cell, thus avoiding continuous irradiation. For the pulsed experiments, a protocol comparable to the one used in the decoupled blend study was used, with 20, 1 min long, 3C discharge pulses. After each 1 min discharge pulse and 10 min relaxation (11 min of total beam exposure), the cell was left without irradiation for approx. 1 h to allow for the recovery of any possible reversible beam-induced effects. The area where the relaxations were recorded remained unirradiated during the pulse and was only exposed to the beam (3 × 1 mm) after the current cutoff. During the 10 min acquisition the cell was oscillated ±1 mm to create an effective exposed area of approximately 3 × 3 mm, thereby reducing the accumulated radiation dose per unit area of the electrode.

2.3 Results and discussion

2.3.1 Decoupled blend continuous electrochemical testing

The 4 materials under study, $LiNi_{0.5}Mn_{0.3}Co_{0.2}O_2$ (NMC), $LiMn_2O_4$ (LMO), $LiFe_{0.35}Mn_{0.65}PO_4$ (LFMP) and $LiFePO_4$ (LFP), were initially measured in the decoupled setup, simulating the 6 possible two component blend combinations: NMC-LFP, NMC-LMO, NMC-LFMP, LFP-LFMP, LMO-LFMP and LMO-LFP. The individual components differ significantly in their voltage vs capacity profiles (see Fig. 1S.I.) which are sloping for NMC, single plateau for LFP, two plateaus at very close potentials for LMO and two plateaus at significantly different potentials for LFMP. Fig. 1 depicts the voltage (in blue) as a function of time for the last C/ 10 cycle of all the cells. The solid black line indicates the current flowing exclusively to one of the materials (determined by the cell's connection), while the dashed black line indicates the total (dis)charging current of the cell distributed between the two materials. The shaded areas indicate the amount of charge stored or provided by each one of them. Colour coding has been implemented throughout this article with NMC marked in Green, LFMP in Black, LFP in Red and LMO in Blue. Voltage vs capacity curves for all the cells can be found in Fig. 2S.I.

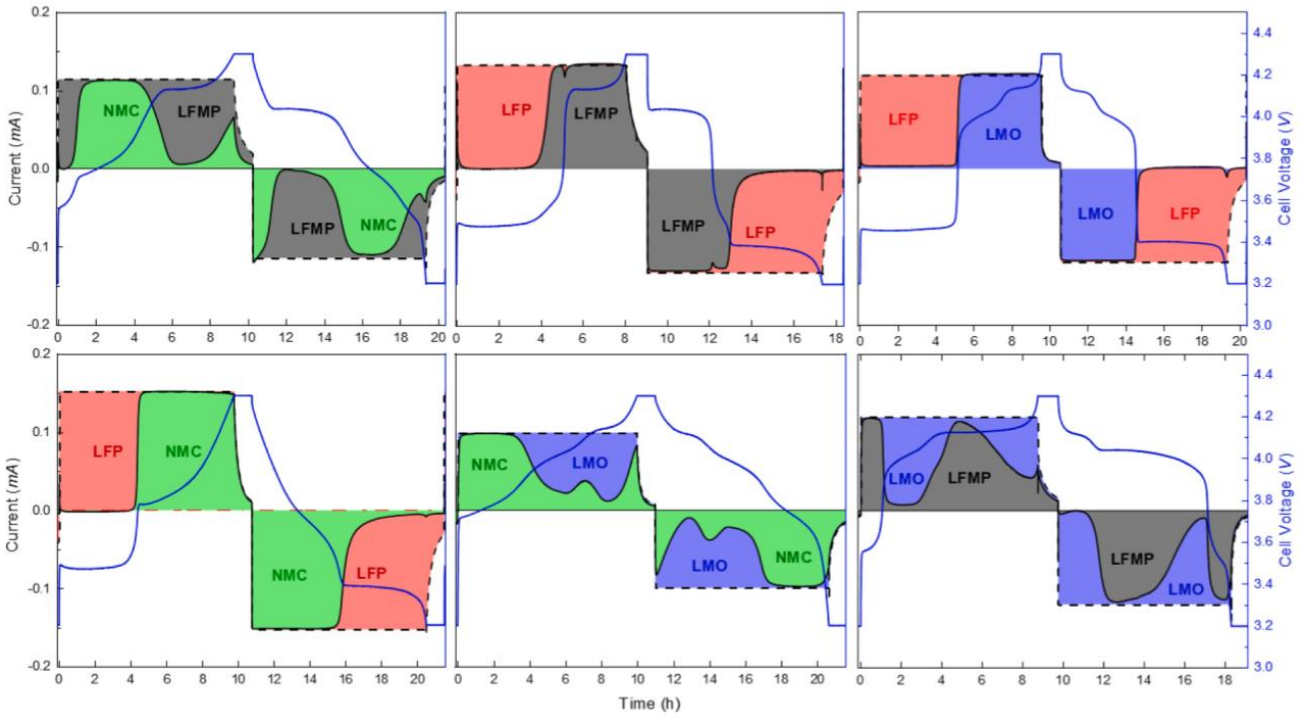

Figure 1: Voltage profiles (Blue Lines) and charge distribution (shaded areas) in each of the 6 combinations of the selected materials when tested using the decoupled blend setup. The dashed black line shows the total (dis)charging current of the cell, set to achieve a cell nominal rate of C/10.

The distribution of the current between the two blend components depends on the individual voltage profile of the materials, and therefore varies significantly with the SoC. Except for the case of NMC-LMO, each component´s contribution ranges from ca. 0 % to ca. 100 % throughout both charge and discharge, which is related to the little overlap between the voltage profiles of the two materials.

Since each material accounts for 50 % of the active mass of the blend, and the cell´s nominal C-rate is calculated taking into account the total expected capacity, the effective C-rate for a component in the areas where it has 100 % contribution will be substantially higher (exactly double if both materials had the same capacity). This situation contrasts with the case of an electrode containing a single active material, which would withstand a constant C-rate throughout the full voltage range. Blended electrodes exhibit thus an extra level of complexity because the effective rate can significantly vary depending on the cell SoC. Since lithium intercalation kinetics in active materials may also depend on

their level of lithiation, blends could be designed to reduce the load of a specific component during a "low kinetics" region and increase it for the "fast kinetics" phase, tailoring them to the real application operation conditions (e.g. voltage window and power). Furthermore, the magnitude of this load increase/decrease could also be modified by changing the mass ratio between the blend components, though this remains out of the scope of this study.

The results depicted in Fig. 1 clearly indicate that the distribution of current for the charge and discharge processes is rather symmetrical, which indicates reversibility of the processes taking place regardless the direction of the current. The minor differences observed in some cases are attributed to overpotential and depend on the cell rate and the kinetics of the materials. The latter may vary with the SoC resulting in different overpotentials during lithiation or delithiation.

Interestingly, blends containing LFP exhibit a stepwise change in current contribution when the voltage of the blend is close to 3.4 V, the value at which the potential vs capacity profile of LFP exhibits a very flat plateau (Fig. 1S.I.). During charge, the activity of LFP is initially 100 % but falls to near 0 % when the blend voltage exceeds the LFP plateau voltage. A similar situation occurs with LFMP. However, since the characteristic curve of this material exhibits two plateaus at around 3.5 V and 4.05 V (Fig. 1S.I.), the activity of LFMP distinctly rises twice during both charge and discharge for both LFMP-LMO and LFMP-NMC, which is when the voltage of the blend coincides with the voltage corresponding to the plateaus. Since NMC exhibits a sloping voltage vs capacity profile, its contribution in a blend with a material exhibiting plateaus tends to increase when the voltage of the cell is above, below or in between the plateaus of the other material. Conversely, the contribution of NMC decreases dramatically when the cell voltage coincides with the plateau voltage of the other material.

This phenomenon can also be explained in terms of the rate of change of charge with respect to voltage, expressed as dQ/dV. The sloping behaviour of NMC results in a significant dQ/dV value throughout its working voltage range, while the other materials

display a spike in dQ/ dV at their voltage plateau and reach values close to 0 at the other voltages. The material with the higher contribution at each blend cell operation voltage is the one with higher dQ/dV. This is showcased in Fig. 2 for the case of NMC-LMO where dQ/dV measured for a C/10 discharge of two coin cells containing electrodes with only NMC (Green) or only LMO (Red) as active materials are plotted together with the current going to NMC in the NMC-LMO decoupled blend experiment (Black dashed line), also carried out at C/10. These results demonstrate a close agreement between the results of both types of experiments, as the current directed to NMC closely aligns with the total cell current (solid black line) when LMO´s dQ/dV is close to 0. This is evident at voltages higher than 4.2 V or lower than 3.9 V. In contrast, at 4.12 V and 4.00 V, where plateaus of LMO are observed, NMC current drops to very low values (indicating that LMO´s current is very high). In the region around 4.1 V, where the two materials have similar dQ/dV values, the current is shared between them, in agreement with the expectations. As the discharge C-rate increases, the dQ/dV peaks are expected to shift towards lower voltages according to the rate each material is experiencing and its reaction kinetics. For a continuous discharge and electrodes containing a single active materials this rate will be constant yet in blended electrodes this peak shift will be more complex due to the non-constant rate, and different for each of the blended active materials. With sufficient knowledge of the reaction kinetics and the material specific rates, dQ/dV plots could potentially be used as a prognostic tool for blended electrodes.

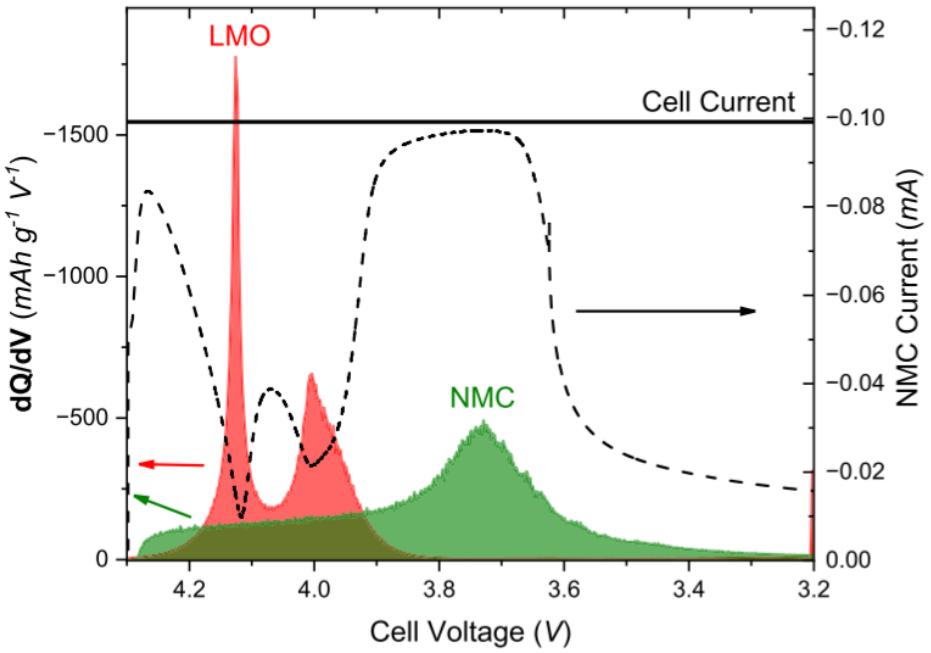

Figure 2: dQ/dV of NMC (Green) and LMO (Red) as measured from coin cells of the pure materials and NMC´s current (Black dashed line) during the decoupled NMC-LMO blend experiment. Solid black line shows the total discharge current of the decoupled blend cell.

2.3.2 Decoupled blend pulsed electrochemical testing

Galvanostatic discharge pulses were also applied to the decoupled blends in order to monitor the exchange of charge between blend components during relaxation on the same cells used previously for the continuous charge/discharge protocol. as described in Section 2.1.

Fig. 3a illustrates the pulsed discharge data obtained for the NMCLMO blend while those corresponding to the rest of combinations can be found in Fig. 4S.I. The top figure shows the evolution of cell voltage vs time during the pulsed discharge, while the bottom plot represents the NMC current vs time. The latter reveals that current of significant magnitude flows between blend components during relaxation as indicated by the shaded areas. This current is represented in different colours depending on its

direction, where green shows the current from LMO to NMC and red from NMC to LMO, as schematically shown in Fig. 3b for three representative pulses.

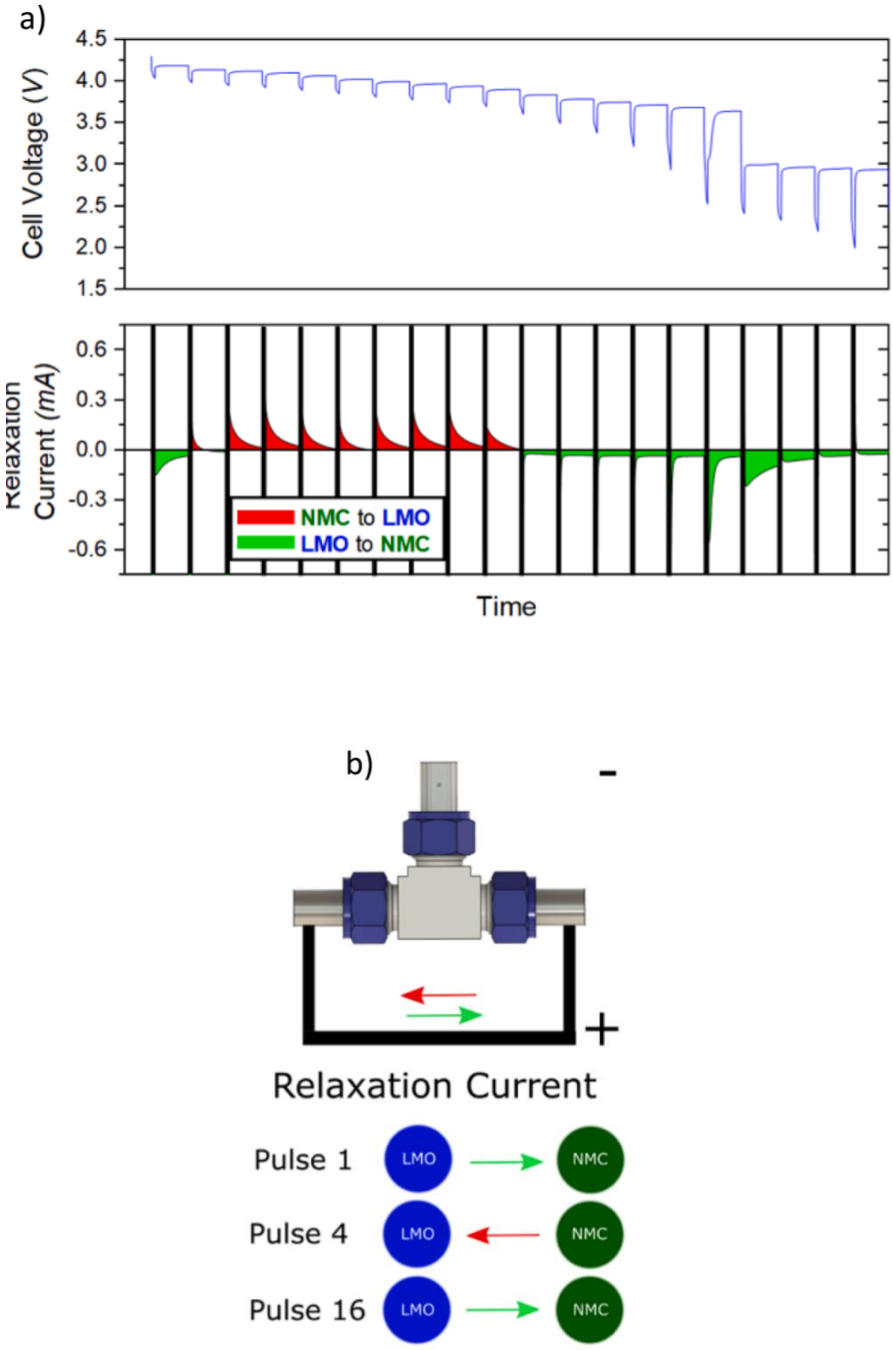

Figure 3: (a) Pulsed discharge protocol showing the voltage vs time (top) as well as the relaxation current (bottom), color coded depending on the lithium flow direction (green for LMO to NMC and red for NMC to LMO). (b) Graphical representation of the cell and the relaxation current (top), direction of the relaxation current for selected pulses (bottom) of the present measurement.

During a high current pulse and due to the high flux of lithium towards one of the components causing a growing overpotential, it may become favorable for the lithium to be incorporated into the other material (depending on its voltage profile). Since this is an out of equilibrium condition, when the flux of lithium (cell current) is cut and the overpotential diminishes, lithium ions will be transferred between components to reach equilibrium. This phenomenon has been studied before, and is commonly referred to as the "buffer effect". However the studies presented herein allow to infer that the directionality of this current can vary with voltage (and therefore, with cell SoC), which is rooted both in thermodynamic aspects (voltage profile) and individual reaction kinetics, which in turn may vary with SoC for each component. In this case LMO accommodates excess lithium during the first galvanostatic discharge pulse and beyond pulse number 10. Hence during the relaxation period, lithium will be transferred from LMO to NMC. The situation is however reversed during pulses 2–10, where NMC is able to accommodate excess lithium during the pulse, and LMO accepts the extra lithium during relaxation.

Fig. 4 shows the magnitude and directionality of the relaxation current observed for each of the four materials when blended with any of the other three. This is presented as a function of the specific capacity of the blend specifying which material acts as a lithium donor (positive y values) or lithium acceptor (negative y values) during the pulse relaxation. Building upon the example of LMO – NMC outlined earlier, the top-left graph reveals that, except for the first pulse, NMC serves as a Li + donor until pulse 12 and transitions to an acceptor role from pulse 12 onward. This behaviour is analogous to what happens when blended with LFMP. In contrast, when blended with LFP, NMC predominantly operates as a Li + acceptor.

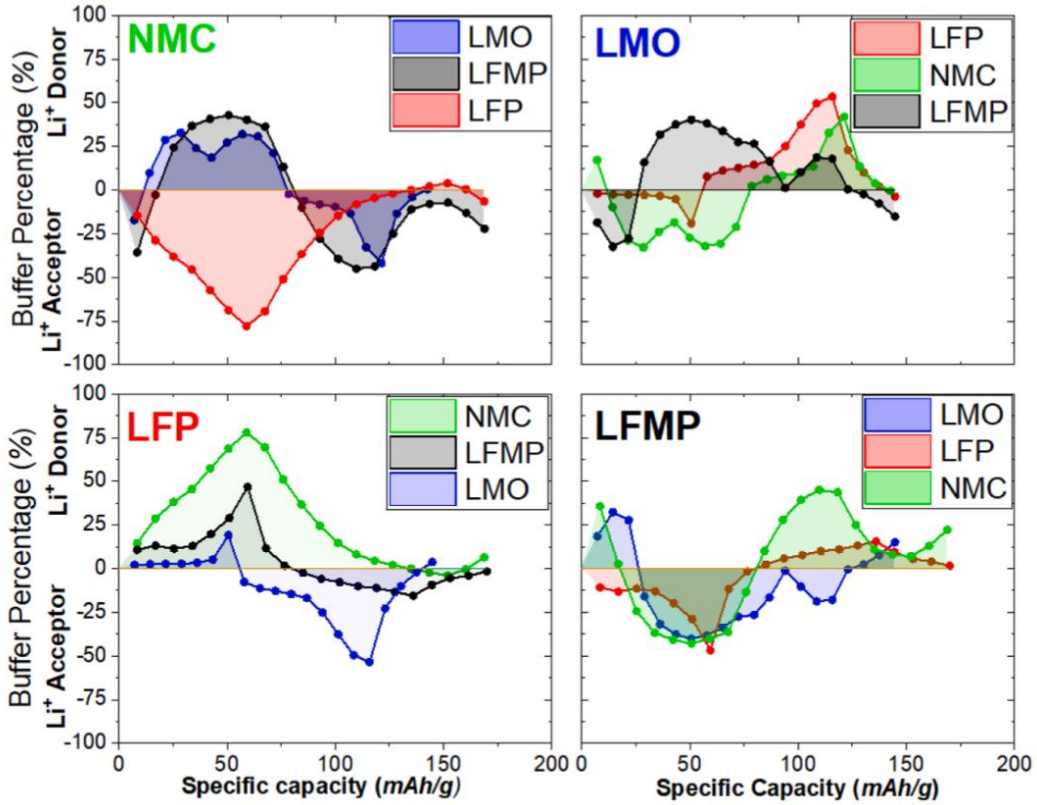

Figure 4: Combined view of the charge transferred during relaxation (expressed as percentage of the total pulse charge) as a function of specific capacity for all the possible combinations of the 4 materials studied. The blends represented in each plot share one common component (written in the upper left corner of each plot) and the y-values indicate if this component acts as lithium donor (positive) or acceptor (negative) during post-pulse relaxation.

2.3.3 Effect of temperature in the relaxation current

The above results allow to assess the variation of the magnitude and the directionality of the current exchange between blend components, which is dictated by the voltage profiles of the active materials. Yet, other factors are expected to play an additional role, such as the relative particle sizes, electrode formulation and properties as well as temperature, that directly affects kinetics, the extent of the effect being also different depending on SoC.

To explore the effect of temperature, a new set of identical cells was made, and the same electrochemical protocol described in 3.1 was applied to them after they were thermalized at 40°C. Fig. 5a shows the comparison of the measurements done for blends of NMC at 25°C and 40°C. First, with increasing temperature, the relaxation specific current peaks at higher values, which could be explained by the enhanced conductivity of the electrolyte as well as the faster kinetics of lithium within the materials and at the material-electrolyte interfaces. However, at higher temperature, the total amount of charge exchanged between the materials during relaxation seems to have decreased. In Fig. 5b the value of the voltage after the 10 min relaxation, as well as the lowest voltage value recorded during the pulse, are depicted. It can be seen that, even though the relaxation voltages almost coincide for the two temperatures under study, there are significant discrepancies in the minimum voltage values recorded, which are systematically lower at 25°C. The decrease of the overpotential for higher temperatures is something well established, yet what is deduced here is that the overpotential on each material is what drives the post-pulse inter-material relaxation. Increasing the overpotential is thus expected to also increase the amount of lithium transferred between blend components during relaxation, as shown in Fig. 5c.

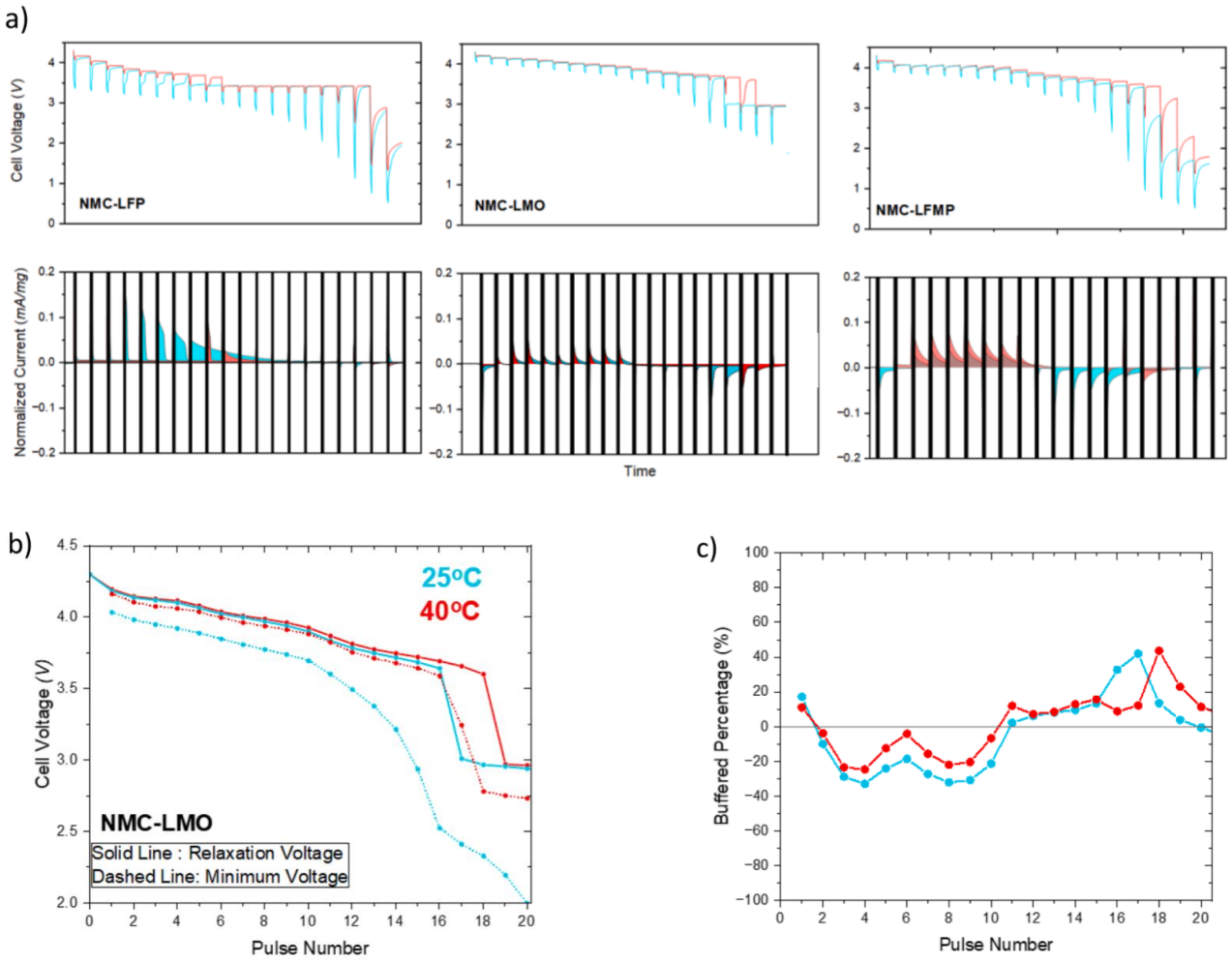

Figure 5: (a) Comparison between pulsed discharges and relaxation currents at 25°C and 40°C (b) After relaxation and minimum voltages recorded for NMC-LMO blend at 25°C and 40°C (c) The relaxation charged expressed as the percentage of the total pulse charge.

An interesting case is that of pulses 3–9 for NMC-LFMP where the amount of lithium transferred during relaxation is higher at 40°C. This is attributed to the fact that relaxation is not finished between two consecutive pulses (i.e. the current is still significant). It is expected that, given enough time to fully relax (with current approaching zero) the amount of charge transferred at high temperatures will be lower, as observed for the experiments involving blends containing LFP, LMO and NMC. This effect is however of interest, as pulsing an already out of equilibrium blended electrode could be a plausible

scenario for batteries in real world situations as fast consecutive accelerations in electric vehicles.

2.3.4 Study of the internal dynamics in a blended positive electrode through operando X-Ray diffraction (XRD)

Operando X-ray diffraction was conducted as described in Section 2.2 to capture structural changes associated to charge transfer events between blend components through time-resolved experiments. In this case the blend components are not separated as in the decoupled blend study but physically mixed and part of a single electrode, providing complementary information. Initially, a low rate (C/5) continuous discharge was recorded for all the blends in the 4.3–3.2 V range to follow the evolution of the diffraction peaks. Fig. 6 below shows selected regions of the recorded patterns which enable to follow the evolution of specific peaks characteristic of each material as a function of SoC. The measured capacity vs voltage curves are shown in Fig. 3S.I. and show remarkable similarity with the curves measured for the decoupled blends regardless of the very different measurement setup and higher rate (C/5 for XRD and C/10 for the decoupled blends).

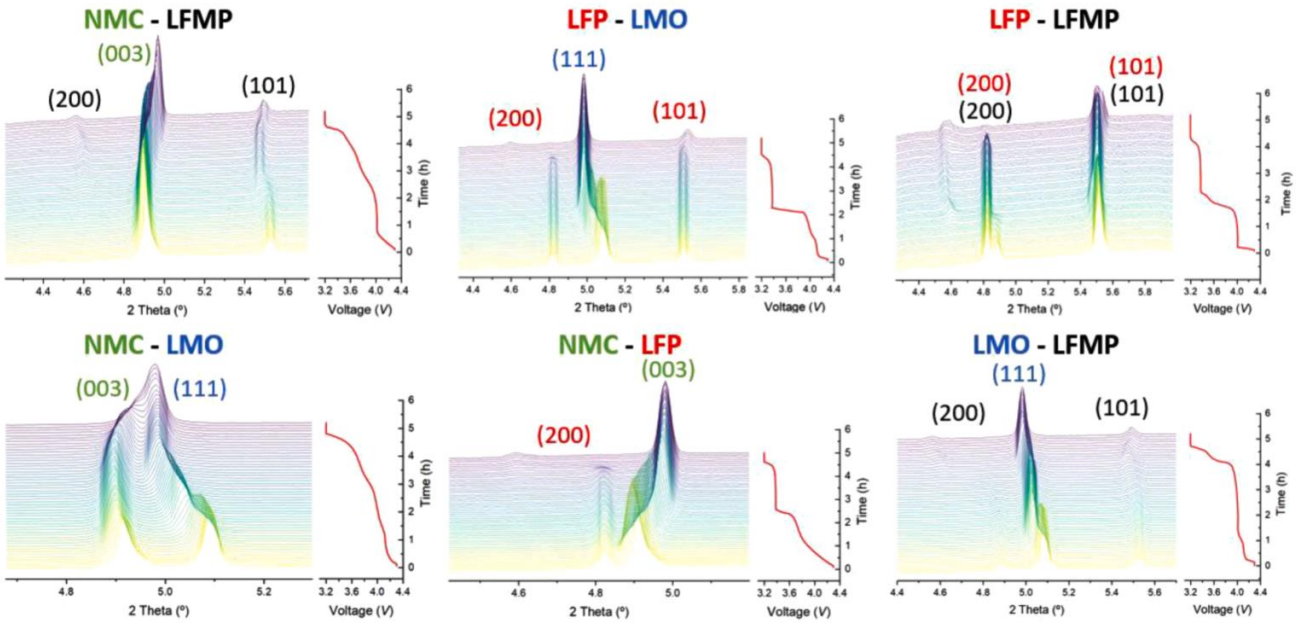

Figure 6: Diffraction patterns recorded during continuous C/5 discharge of the blended electrodes at 30 keV (λ = 0.4135 Å) together with the corresponding voltage profile. Angular ranges depicted contain the more relevant and intense peaks of the blend components. Their Miller indices, colour coded according to material, are also shown.

For NMC (R-3 m space group), there is a non-monotonic shift of the $(003)_{NMC}$ peak (initially at 4.9°) towards lower angles first, and in the opposite direction afterwards, in agreement with the expected behavior and well-known evolution of material´s interlayer distance. For LMO spinel (Fd-3 m space group), the $(111)_{LMO}$ peak appears initially at 5.1° and shifts to lower angles upon lithium intercalation, again in good agreement with the expected behavior. Note that $(003)_{NMC}$ and $(111)_{LMO}$ reflections converge at the end of discharge. The $(200)_{FP}$ peak of the olivine $FePO_4$ (Pnma space group) appears at approx. 4.81° and decreases gradually in intensity (in agreement with the redox mechanism of LFP involving a first order phase transition) at the expense of the $(200)_{LFP}$ peak appearing at around 4.6°. The $(101)_{FP}$ peak is also seen at around 5.5° which slightly shifts to higher angles when lithiated. Finally, for the also olivine LFMP (Pnma space group) two peaks are observed, at 4.88° (200) and 5.52° (101). The low angle peak disappears while a peak rises at around 4.6° while the one at 5.52° shifts to lower

angles until 5.48° and then again slightly towards higher angles. The behaviour of the observed peaks are in line with what is expected from their reaction mechanism.

Consistent with the results of the decoupled blend study (Fig. 1) the SoC of a specific active material, monitored through the evolution of its diffraction peaks, will evolve differently with the depth of discharge for each blend in which it is present. A good example is that of LMO when blended with LFP or LFMP. Due to the lower voltage of LFP compared to the significantly higher voltage of LMO, the two materials discharge sequentially with LMO undergoing full lithiation before lithium is inserted into LFP. This is demonstrated by the $(111)_{LMO}$ peak in the LFP-LMO blend in Fig. 6, which has reached its lithiated position after approximately 2.5 h and remains unchanged while LFP is active. Conversely, the behavior of LMO-LFMP blend is different, since LFMP is also active at high voltages, resulting in a more simultaneous discharge of the two materials. Once again, this can be showcased by the $(111)_{LMO}$ peak which in this case reaches its final position at the end of the discharge, and it is witnessed to evolve throughout the whole discharging process. A similar analysis can be applied to the NMC-LMO and the NMC-LFP blend. Focusing on the $(003)_{NMC}$ peak, when blended with LMO, much of the peak shift happens towards the end of discharge, after 3 h, which is in line with the decoupled blend study shown in Fig. 1 where NMC is predominantly active towards the end of the discharge. This phenomenon is reversed when NMC is combined with LFP, as both XRD and decoupled blends show NMC activity towards the beginning of the discharge. In this case, and similarly to the LMO-LFP blend, the materials discharge in a sequential fashion and as such the (003) NMC peak makes its full range of shift in the first half of the discharge.

Pulsed discharges including relaxation steps between consecutive pulses were also followed by operando XRD. While voltage profiles and the directionality of lithium during relaxation are expected to be similar to those observed in the experiment using the decoupled blend setup described in Section 3.2, we anticipate slight differences in kinetics due to the faster lithium exchange in a true blended cathode where the components are in direct contact.

As described in Section 2.2, the operando experiments to follow both pulses and relaxation between successive pulses were carried out at both 15 keV and 30 keV aiming to identify potential beam effects. Fig. 7 shows the patterns taken during the pulse for NMC containing blends measured for both energies. The expected peak evolution is observed in both cases, yet a more distinct pattern evolution is seen at 30 keV. Notably, there is a smaller peak intensity variation between the patterns as well as less broadening which could be attributed to a more homogeneous lithiation in the area under irradiation. For both NMC-LMO and NMC-LFMP blends, the $(003)_{NMC}$ peak in Fig. 7 does not reach the expected position at full lithiation at 15 keV. This discrepancy is resolved at 30 keV, where the $(003)_{NMC}$ peak overlaps with the (111) LMO peak. For NMC-LFMP the peak in the final pattern at 15 keV is broader and exhibits lower intensity, in agreement with a less homogeneous lithiation degree in the irradiated area. Once again this is not the case for 30 keV. For NMC-LFP, the $(003)_{NMC}$ peak appears to reach to its final state also at 15 keV, yet this is attributed most likely to LFP being a lower voltage material expected to start lithiating after NMC is fully lithiated. This results in NMC spending a large fraction of the discharge time in the fully lithiated state and as such having more time to reach its final state, which might be perceived as reduced reaction kinetics. Comparing the patterns at different energies, it can be concluded that significant differences occur based on beam photon energy, with higher energy photons proving effective in minimizing beam related effects and this dependence is in line with recently published works [24]. Some of the studied active materials, namely NMC and LFP, were found to be more sensitive to such phenomena. Electrochemistry showed no signs of alteration from the beam, which could be explained with the fact that the illuminated area accounted only for approximately 6 % (~10 mm^2) of the total electrode area (~154 mm^2).

Measuring at higher energy (lower wavelength) comes however with the drawback of the patterns appearing "compressed". This is evident from the x axes scales of Fig. 7, where the same peaks are being pictured for both energies. This effect, paired with the fact that kinetics at 15 keV seem slower despite all precautions taken, increase the

possibility that the buffer effect is better captured at 15 keV, potentially enabling us to leverage beam effects to our advantage.

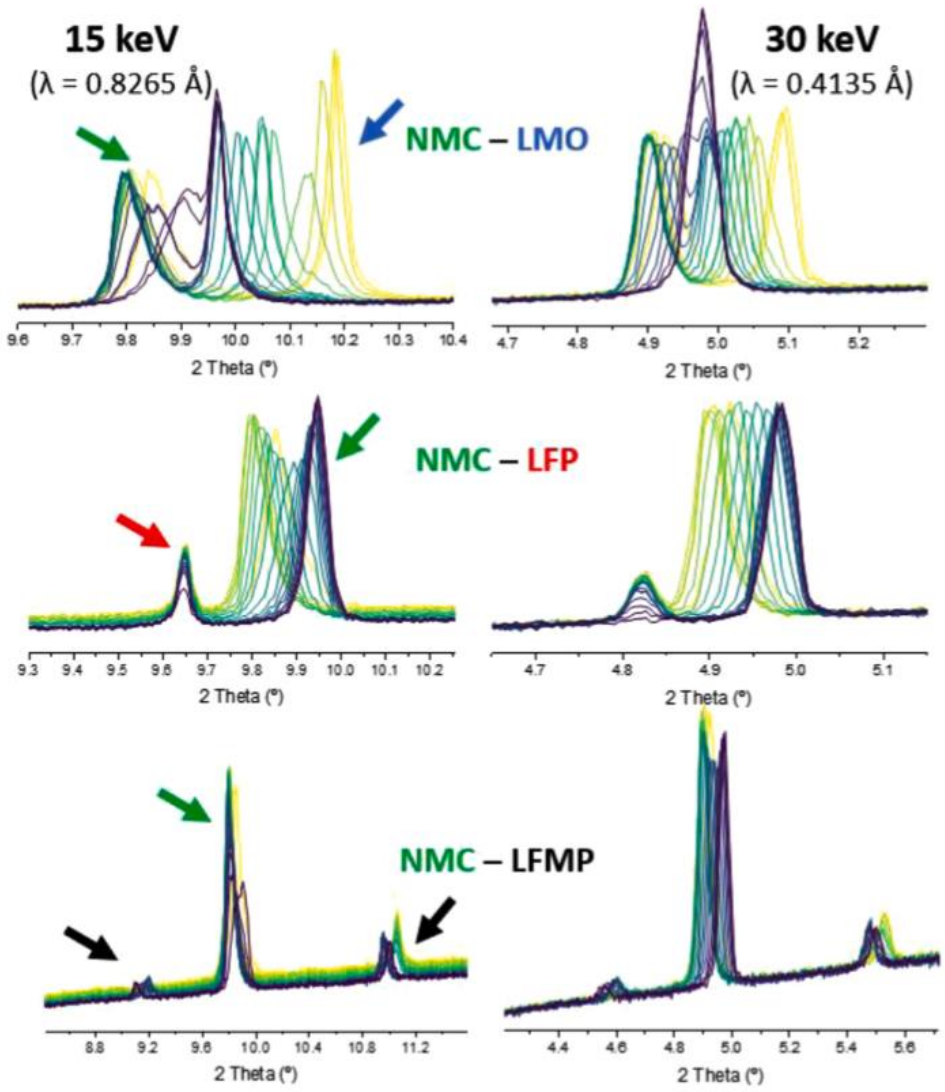

Figure 7: First pattern recorded for each of the pulses at 15 keV (= 0.8265 Å) and 30 keV (λ = 0.4135 Å). Arrows are colour coded according to the material to which each peak corresponds.

Fig. 8 shows selected pulses where all the patterns obtained for each relaxation (approx. 160 patterns) are depicted evolving from black (immediately after current interruption) to yellow (after 10 min of no current) at 15 keV (same plots for 30 keV are shown in Fig. 5S.I.). For the understanding of the results, one can make predictions using the decoupled blends study. For the case of NMC-LMO, as seen in Fig. 3, during relaxation

of pulse 1, lithium is transferred from LMO to NMC which is also witnessed in the diffraction in Fig. 8a where the $(003)_{NMC}$ peak shifts towards lower angles indicating lithiation while $(111)_{LMO}$ peak shifts slightly towards higher angles showing evidence of delithiation. For the relaxation of pulse 4 (Fig. 8b), decoupled blends predict lithiation of LMO and delithiation of NMC yet in diffraction only the lithiation of LMO is witnessed, evidenced by the shift of the $(111)_{LMO}$ peak towards lower angles. Finally, for pulse 16, lithium exchange is expected to happen from LMO to NMC, and once again only the lithiating component was witnessed. Delithiation is also captured for the NMC-LFP through an increase in the intensity of $(002)_{LFP}$ peak. In general, even though delithiation was proven challenging to evidence in XRD, the material that was witnessed relaxing was in the vast majority of cases in line with the decoupled blends experiment and this serves as a direct proof of the buffer effect in the electrodes under study, as predicted by the decoupled blends.

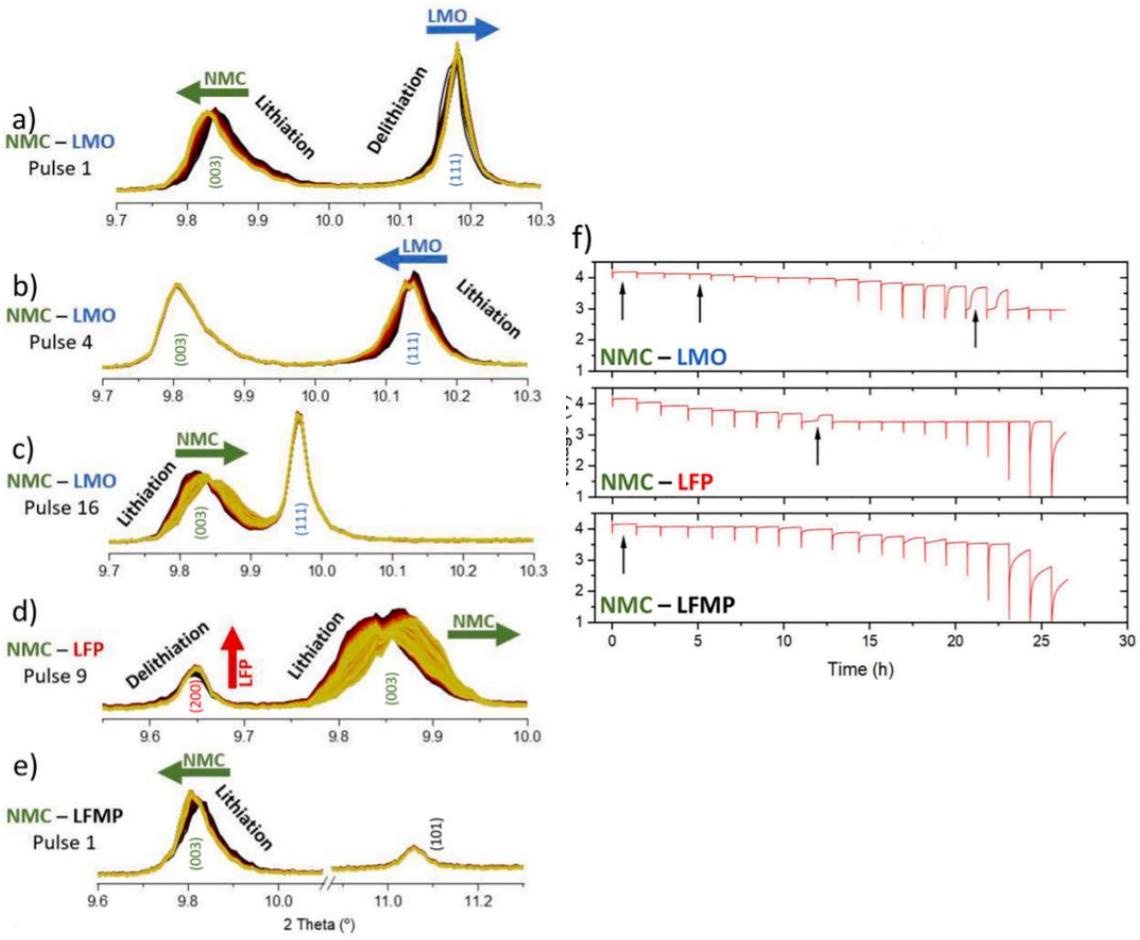

Figure 8: (a–e) Selected relaxations of measured blends showing peak evolution, black is the first pattern obtained after the pulse and yellow is the last. Arrows are colour coded according to material and act as a guide to the eye for the peak shift observed during relaxation. On top of each peak, the shift observed is linked to the materials (de)lithiation. f) Voltage as a function of time for the blends pictured. The black arrows indicate the relaxations shown in plots a-e.

The difficulty in witnessing the delithiation can be rationalized in terms of electrode kinetics. Due to the technical nature of the cell, the area where the windows are experiences a lower stack pressure in addition to being irradiated. Both can contribute in the slower kinetics of the materials, with 15 keV experiments seemingly experiencing a stronger effect. After the pulse, lithiation naturally homogenizes throughout the electrode, and a general influx of lithium is expected from faster kinetically active areas towards the slower ones—specifically, the area under test. This phenomenon is expected

to be superimposed to the buffer effect and as such favour the witnessing of the lithiation while potentially masking the delithiation. Nevertheless, delithiation is still expected to occur whenever the buffering effect is stronger and, as discussed above, this has been the case in certain pulses.

2.4 Discussion

Despite blended electrodes being widely used in commercial cells, transition from empiricism to full understanding of the internal dynamics with the aim of being able to predict properties is hampered by the complexity of the system, which is also tricky to capture through modelling [27]. Thus, getting experimental data on a range of blend model systems under controlled operation conditions is crucial to shed light on their operation mechanism and advance towards ad hoc rational design of the blends to match specific application demands.

The results achieved within this study illustrate how the performance of blended electrodes, besides depending on the kinetics of each individual component (influenced by both electronic and ionic conductivities, which can also vary with the SoC), is influenced by thermodynamics (voltage profiles). Indeed, these play a role on the extent and directionality of the current/lithium exchanged between components, which exhibit relevant variations throughout the full range of operation. Even if the study does not cover changes in the ratio between the components, it is clear that the blending fraction will have an additional effect on these aspects. Considering a material that takes the whole cell current at a certain voltage, its effective operation rate will be dictated by its fraction. In a hypothetical blend of materials A and B of equal theoretical capacities where A is 20 % of the active mass, if all the cell current is provided by A at a certain voltage, its effective rate would be 5 times higher than the cell´s nominal rate. Yet, if it's material B that provides all cell current, its effective rate will be only 1.25 times higher. Thus, it can be expected that using a small fraction of a material with a plateau

in a blend would cause it to experience exceedingly high rates when the cell voltage coincides with the one of the plateau.

Since for many materials kinetics are a function of SoC, blending could be used as a strategy to relief or stress operation at certain voltage. During pulsed operation the magnitude of the "buffer effect" in the electrode will be dictated by effective overpotentials on blend component. Since overpotential is not only related to intrinsic properties of materials but also affected by other aspects, such as particle size or electrode related parameters (e.g. porosity and tortuosity), these can provide an additional tool to tune the ability and extent of buffering. Because overpotential will itself be dependent on the SoC, a significant influence of the blending ratio on the buffering can also be expected.

Thermodynamics will dictate the direction of the buffering current which can be deduced from the individual voltage profiles. At a given SoC this direction is expected to be the same upon charge and discharge. Shall buffering occur, a material A with only a high voltage plateau is expected to act as a lithium acceptor during post-pulse relaxation upon discharge when blended with a material B with a lower voltage plateau. Kinetics will only affect the magnitude of the phenomenon, as the overpotential of A grows, it becomes easier to enter the operation voltage range of B and induce the buffer effect. Yet, buffering will no longer be possible once the high voltage material becomes fully lithiated. Reversing the current on the same system is expected to reverse the buffering "roles", now, the low voltage component B, due to overpotential, can enter the active regime of the higher voltage material A, enabling material B to be buffered.

Operando XRD measurements have allowed to capture charge transfer events in real blends, providing a deeper understanding of their behavior. However, the challenges associated with time-resolved XRD, particularly potential beam effects, need careful consideration to ensure the reliability and accuracy of the obtained data. Despite these challenges, the results obtained from operando XRD are in good agreement with those of decoupled electrochemical experiments.

In conclusion, the results presented herein showcase the importance of a holistic approach in studying complex electrode systems. Further work should be addressed to extend this studyto a wider set of temperatures, compositions and blend component ratios (eventually considering ternary [28] or even quaternary compositions), the ultimate goal being to achieve predictive understanding and rationalization of blend design to match specific application operation needs.

2.5 Conclusions

The study of a wide set of binary blend electrodes with a range of different components but keeping a 50:50 ratio between them serves as a valuable complement to previous work carried out on specific blends (e. g. NMC-LMO) with varying compositions. The results presented herein facilitate the assessment of the influence of the voltage profile of the components in the extent and directionality of the charge transfer between them, which is further shown to be dependent on the cell SoC and the operation temperature. The trends deduced from electrochemical experiments carried out using the decoupled blend setup were found to be in very good agreement with those derived from operando XRD on real blended electrodes in which the components are in physical contact, which evidences the representativity of this experimental approach. Assessing the influence of thermodynamic factors constitutes an additional step to progress in the mechanistic understanding of blended electrodes, which is obviously greatly influenced by the reaction kinetics of the individual materials (that also depend on SoC). The findings presented in this study offer a foundational framework for the design of blended electrodes customized to specific application requirements and pave the way for a more informed and strategic approach to developing blended electrodes.

2.6 Supporting Information

Table 1: Achieved mass ratios, 1C specific currents and expected cell capacities in decoupled blends studies.

Decoupled Blend	25°C			40°C		
	Mass Ratio	1C Specific Current (mA/g)	Cell Capacity (mAh)	Mass Ratio	1C Specific Current (mA/g)	Cell Capacity (mAh)
NMC-LFP	49:51	169	1.52	51:49	169	1.34
LMO-LFP	52:48	145	1.16	50:50	146	1.18
NMC-LFMP	46:54	169	1.14	51:49	169	1.39
LFP-LFMP	51:49	170	1.32	50:50	170	1.34
LMO-LFMP	51:49	145	1.19	52:48	145	1.21
NMC-LMO	47:53	143	0.99	50:50	144	1.19

Table 2: 1C specific currents and expected cell capacities in Operando XRD experiments

Operando Cell	Continuous C/10 Cycling		Pulsed Discharges	
	1C Specific Current (mA/g)	Cell Capacity (mAh)	1C Specific Current (mA/g)	Cell Capacity (mAh)
NMC-LFP	169	1.35	169	1.39
LMO-LFP	145	1.10	145	1.09
NMC-LFMP	169	1.35	169	1.38
LFP-LFMP	170	1.31	170	1.39
LMO-LFMP	145	1.17	145	1.14
NMC-LMO	145	1.15	145	1.14

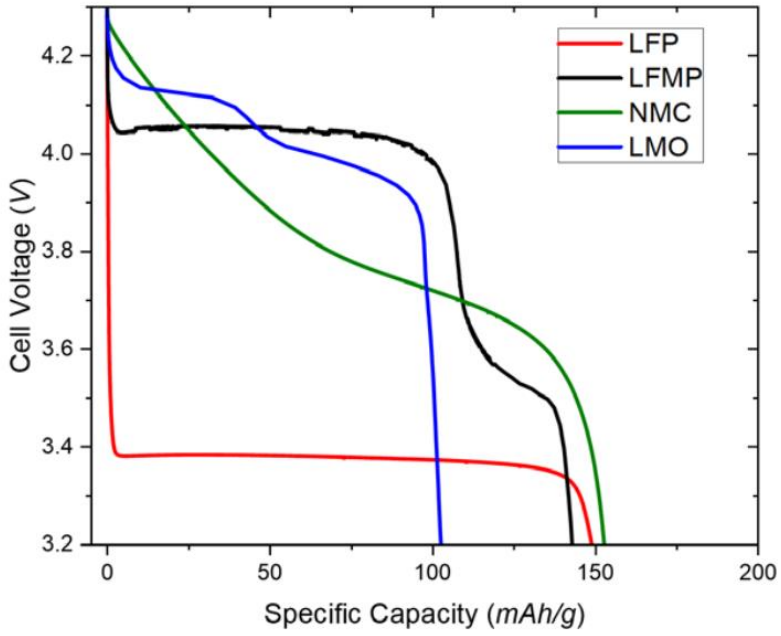

Figure S.I. 1: Voltage (vs Li+/Li) vs Capacity profiles of the materials during discharge at C/10.

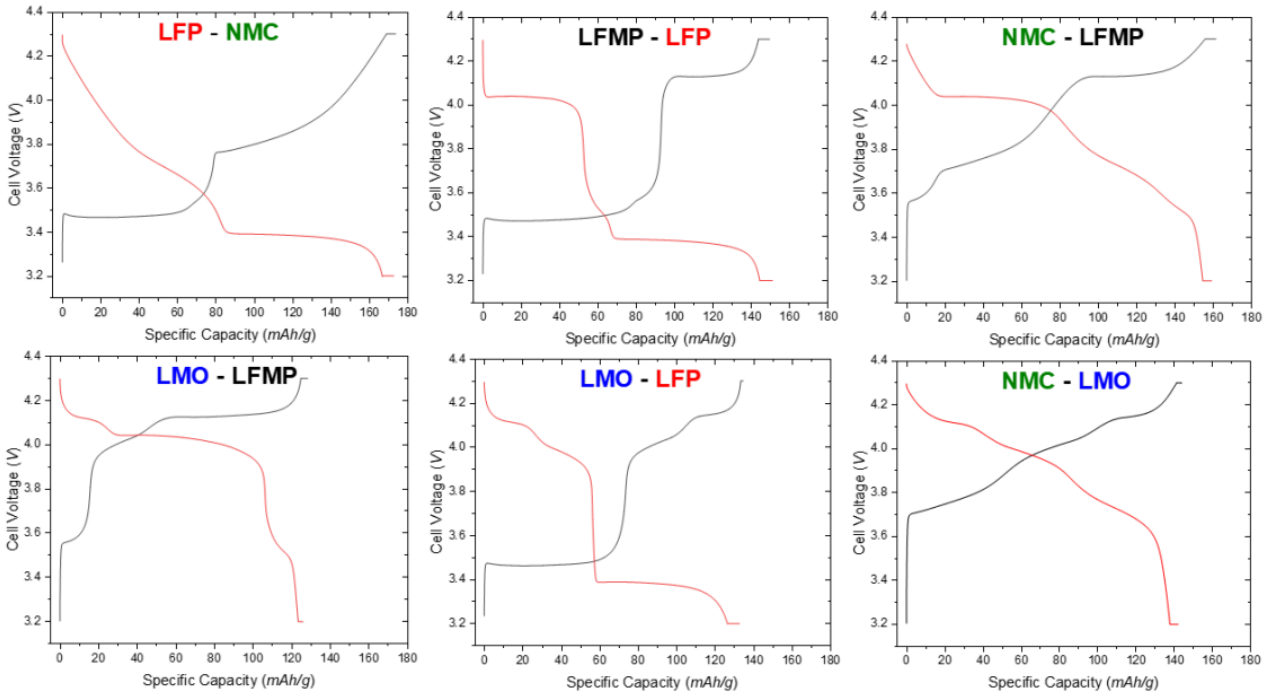

Figure S.I. 2: Voltage vs Capacity plots of the decoupled blend cells cycled at C/10 depicted in Fig.1 of the main text.

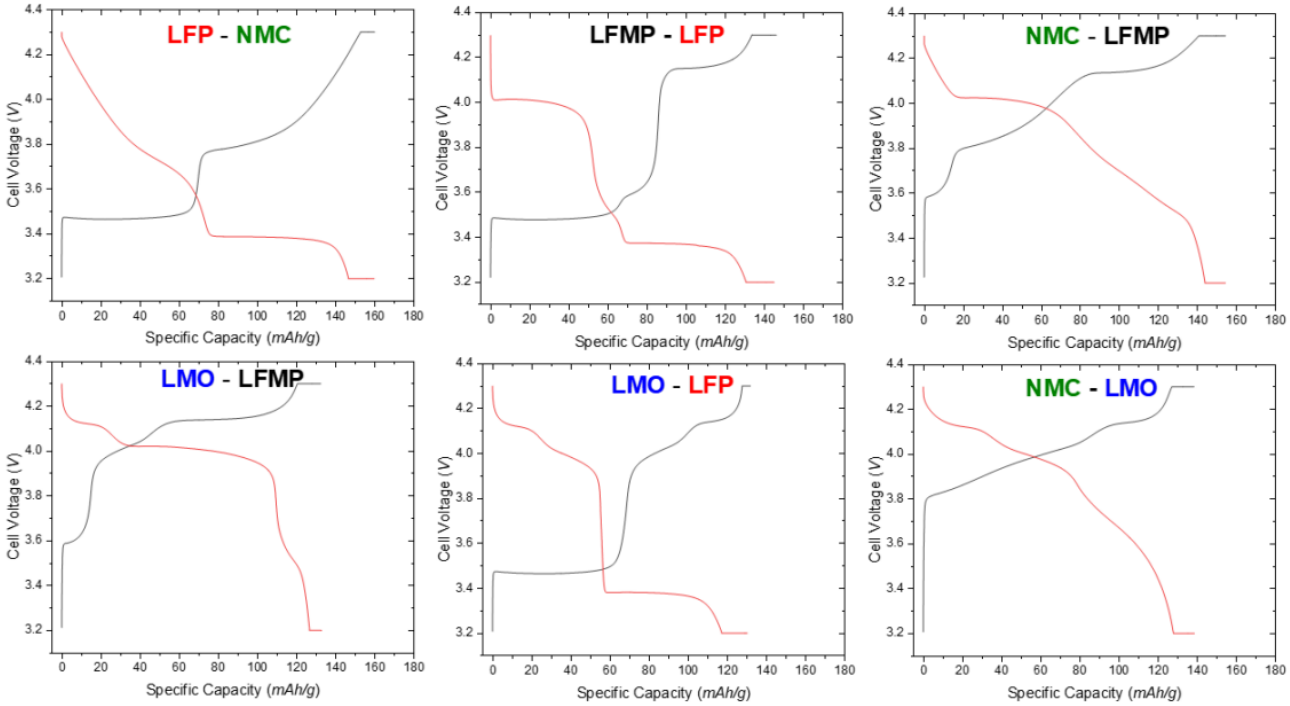

Figure S.I. 3: Voltage vs Capacity plots of the cells used for operando XRD cycled at C/5 and are depicted in depicted in Fig.6

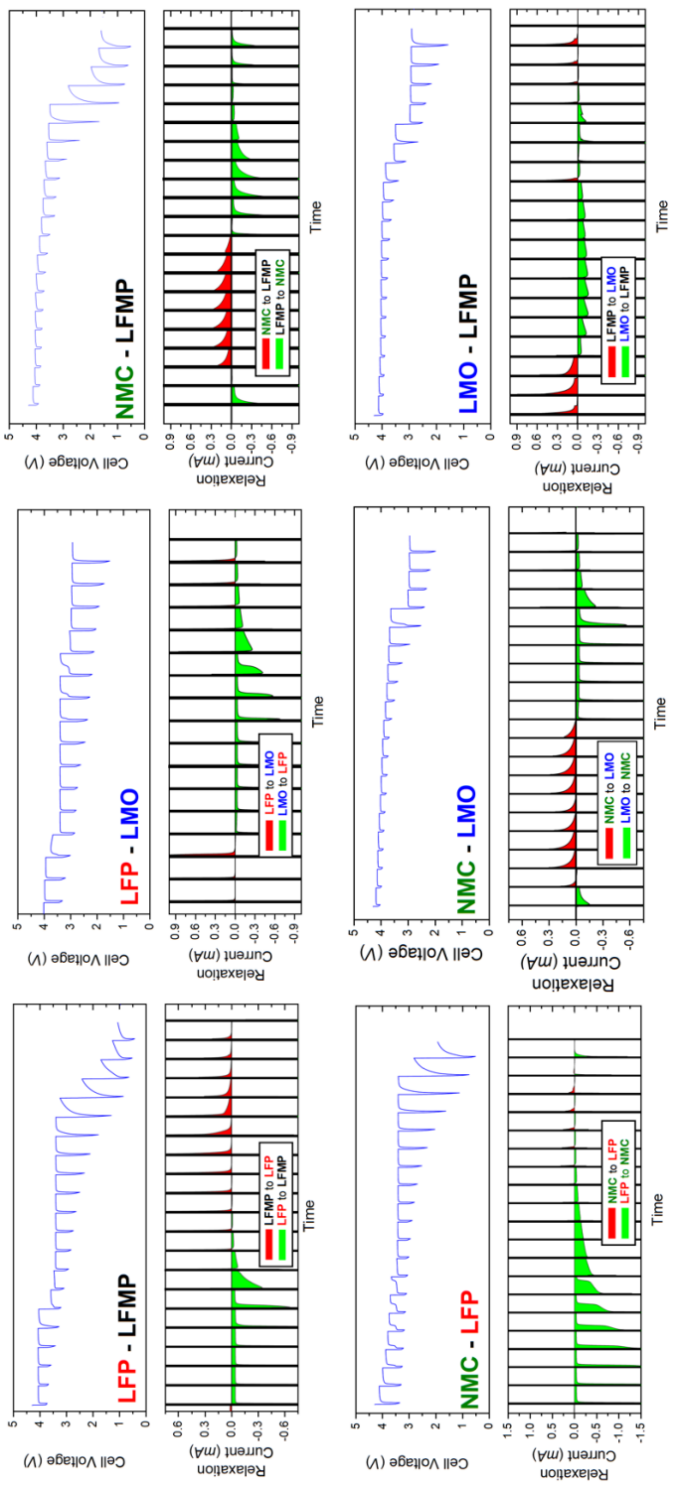

Figure S.I. 4: Data analogous to Fig.3 of the main text, showing the decoupled blend measurements for all the samples. For each blend the voltage profile is shown on top and the post-pulse relaxation current on the bottom.

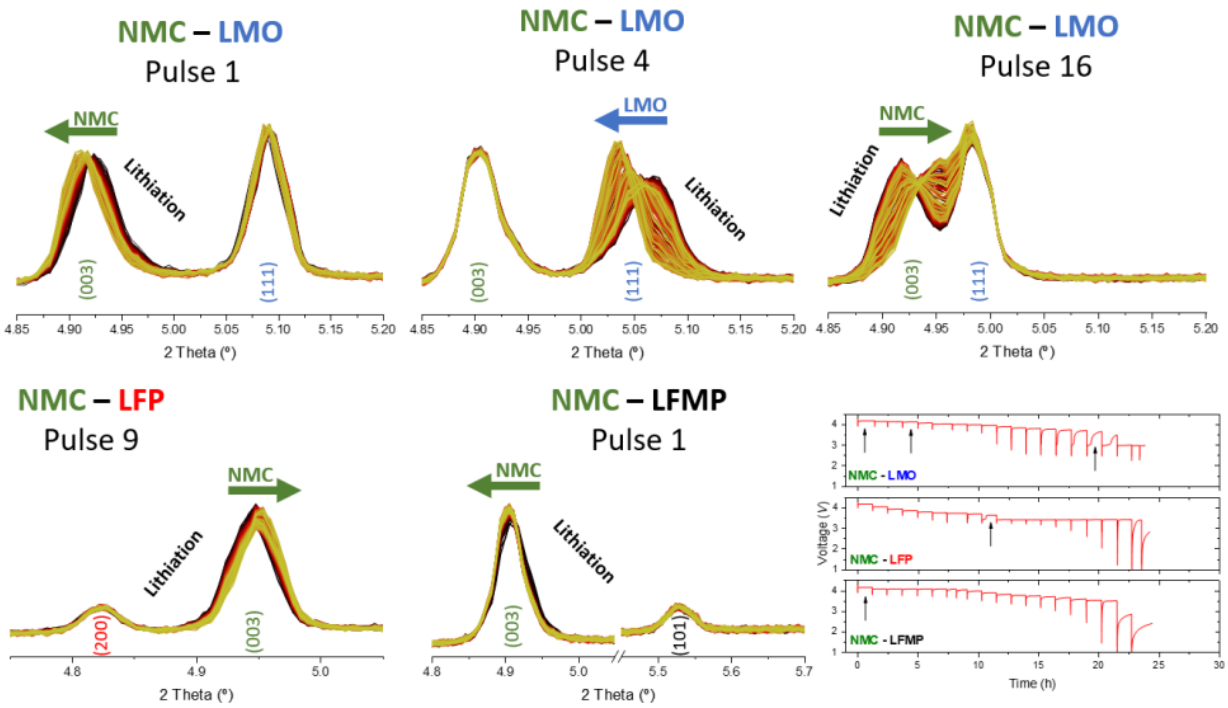

Figure S.I. 5: XRD patterns collected during relaxations collected at 30keV, the relaxations depicted are comparable to the ones depicted in Fig. 8 of the main text for 15keV

References

1. *R. Schmuch, R. Wagner, G. Horpel,¨T. Placke, M. Winter, Performance and cost of materials for lithium-based rechargeable automotive batteries, Nat. Energy 3 (2018) 267–278.*
2. *T. Numata, C. Amemiya, T. Kumeuchi, M. Shirakata, M. Yonezawa, Advantages of blending LiNi0.8Co0.2O2 into Li1+xMn2− xO4 cathodes, J. Power Sources 97–98 (2001) 358–360.*
3. *S.B. Chikkannanavar, D.M. Bernardi, L. Liu, A review of blended cathode materials for use in Li-ion batteries, J. Power Sources 248 (2014) 91–100.*
4. *H.Y. Tran, C. T¨aubert, M. Wohlfahrt-Mehrens, Influence of the technical process parameters on structural, mechanical and electrochemical properties of LiNi0.8Co0.15Al0.05O2 based electrodes – a review, Prog. Solid State Chem. 42 (2014) 118–127.*
5. *A.J. Smith, S.R. Smith, T. Byrne, J.C. Burns, J.R. Dahn, Synergies in blended LiMn2O4 and Li [Ni1/3Mn1/3Co1/3]O2 positive electrodes, J. Electrochem. Soc. 159 (2012) A1696.*
6. *H.Y. Tran, et al., LiMn2O4 Spinel/LiNi0.8Co0.15Al0.05O2 blends as cathode materials for lithium-ion batteries, J. Electrochem. Soc. 158 (2011) A556.*
7. *N.M. Jobst, A. Hoffmann, A. Klein, S. Zink, M. Wohlfahrt-Mehrens, Ternary cathode blend electrodes for environmentally friendly lithium-ion batteries, ChemSusChem 13 (2020) 3928–3936.*
8. *G. Sun, et al., Synergistic effect between LiNi0.5Co0.2Mn0.3O2 and LiFe0.15Mn0.85PO4/C on Rate and Thermal Performance for Lithium Ion Batteries, ACS Appl. Mater. Interfaces 10 (2018) 16458–16466.*
9. *D. Westhoff, et al., Analysis of microstructural effects in multi-layer lithium-ion battery cathodes, Mater. Charact. 151 (2019) 166–174.*

10. *T. Liebmann, C. Heubner, M. Schneider, A. Michaelis, Understanding kinetic and thermodynamic properties of blended cathode materials for lithium-ion batteries, Mater. Today Energy 22 (2021) 100845.*
11. *T. Liebmann, C. Heubner, M. Schneider, A. Michaelis, Investigations on the reversible heat generation rates of blended Li-insertion electrodes, J. Solid State Electrochem. 23 (2019) 245–250.*
12. *C. Heubner, M. Schneider, A. Michaelis, Reversible heat generation rates of blended insertion electrodes, J. Solid State Electrochem. 21 (2017) 2109–2115.*
13. *C. Heubner, T. Liebmann, C. L¨ammel, M. Schneider, A. Michaelis, Internal dynamics of blended Li-insertion electrodes, J. Energy Storage 20 (2018) 101–108.*
14. *J. Huang, et al., Entropy coefficient of a blended electrode in a lithium-ion cell, J.Electrochem. Soc. 162 (2015) A2367.*
15. *M. Yue, et al., Improved elevated temperature performance of LiFePO4/Graphite cell by blending NMC640 in cathode, J. Electrochem. Soc. 170 (2023) 110532.*
16. *C. Heubner, T. Liebmann, M. Schneider, A. Michaelis, Recent insights into the electrochemical behavior of blended lithium insertion cathodes: a review, Electrochim. Acta 269 (2018) 745–760.*
17. *M. Casas-Cabanas, A. Ponrouch, M.R. Palacín, Blended positive electrodes for Li ion batteries: from empiricism to rational design, Isr. J. Chem. 61 (2021) 26–37.*
18. *T. Liebmann, C. Heubner, C. L¨ammel, M. Schneider, A. Michaelis, Investigations on the effective electric loads in blended insertion electrodes for lithium-ion batteries, ChemElectroChem. 6 (2019) 5728–5734.*
19. *C. Heubner, T. Liebmann, C. Lammel, M. Schneider, A. Michaelis, Deconvolution of cyclic voltammograms for blended lithium insertion compounds by using a modellike blend electrode, ChemElectroChem 5 (2018) 425–428.*
20. *D. Chatzogiannakis, et al., Towards understanding the functional mechanism and synergistic effects of LiMn2O4 - LiNi0.5Mn0.3Co0.2O2 blended positive electrodes for Lithium-ion batteries, J. Power Sources 591 (2024) 233804.*

21. *M. Herklotz, et al., A novel high-throughput setup for in situ powder diffraction on coin cell batteries, J. Appl. Crystallogr. 49 (2016) 340–345.*
22. *D. Saurel, et al., Experimental considerations for operando metal-ion battery monitoring using X-ray techniques, Chem. Methods 1 (2021) 249–260.*
23. *T. Jousseaume, J.F. Colin, M. Chandesris, S. Lyonnard, S. Tardif, How beam damage can skew synchrotron operando studies of batteries, ACS Energy Lett. 8 (2023) 3323–3329.*
24. *C.K. Christensen, et al., Beam damage in operando X-ray diffraction studies of Liion batteries, J. Synchrotron. Radiat. 30 (2023) 561–570.*
25. *L. Blondeau, et al., Are operando measurements of rechargeable batteries always reliable? An example of beam effect with a Mg battery, Anal. Chem. 94 (2022) 9683–9689.*
26. *P. Black, et al., Beam Effects in Synchrotron Radiation Based Operando Characterization of Battery Materials: XRD and XAS Study of LiNi0.33Mn0.33Co0.33O2 and LiFePO4 Electrodes, Submitted for publication, 2024.*
27. *C. Heubner, T. Liebmann, C. Lammel, M. Schneider, A. Michaelis, Synergy effects in blended electrodes for Li-ion batteries: a conceptual clarification, Batter. Supercaps. 5 (2022) e202100171.*
28. *M.S.D. Darma, et al., The influence of cycling temperature and cycling rate on the phase specific degradation of a positive electrode in lithium ion batteries: a post mortem analysis, J. Power Sources 327 (2016) 714–725.*

3. Towards Understanding the functional mechanism and synergistic effects of $LiMn_2O_4$ – $LiNi_{0.5}Mn_{0.3}Co_{0.2}O_2$ blended positive electrodes for Lithium-ion batteries

Dimitrios Chatzogiannakis, Marcus Fehse, Maria Angeles Cabañero, Natalia Romano, Ashley Black, Damien Saurel, M. Rosa Palacin, Montse Casas-Cabanas

Journal of Power Sources, Volume 591, 30 January 2024, 233804

https://doi.org/10.1016/j.jpowsour.2023.233804

Abstract

Blended positive electrodes consisting of mixtures of $LiMn_2O_4$ spinel (LMO) and layered $LiNi_{0.5}Mn_{0.3}Co_{0.2}O_2$ (NMC) have been studied by coupling electrochemical testing to operando synchrotron based X-ray absorption and powder diffraction experiments to shed light on their redox mechanism. Blending NMC with LMO results in enhanced energy density at high rates, with the composition with 25% LMO exhibiting the best electrochemical performance. Tests with a special electrochemical setup detecting the contribution of each blend component indicate that the effective current load on each blend component can be significantly different from the nominal rate and also varies as function of SoC. Operando studies enabled to monitor the evolution of oxidation state and changes in the crystal structure, which are in agreement with the expected behaviour of the individual components considering the material specific electrochemical current loads. These findings should contribute to a deeper mechanistic understanding of blended electrodes to foster a rational driven approach for their design.

3.1 Introduction

"Blended" positive electrodes with multiple active materials pose an interesting and industrially relevant approach to overcome intrinsic disadvantages of certain single compounds. Mixing materials in the right proportion can potentially give rise to improvements in a variety of properties. Several works have reported enhanced thermal stability [1,2], increased rate capability [3] and extended cycle life via blending, in particular for $LiMn_2O_4$, which exhibits fast kinetics but limited capacity [2,4,5]. Numerous studies on $LiNi_xMn_yCo_zO_2$ (where x+y+z = 1, often referred to as NMC-XYZ e.g. NMC-111, NMC-532, NMC-811, etc.) have shown that electrochemical performance is significantly dependent on the relative transition metal ratios. A general understanding of the phase diagram of NMCs is that increasing the amount of cobalt favours the lithium (de)intercalation reaction kinetics, high nickel content improves capacity and raising the amount of manganese favours thermal stability (and hence safety) and lowers cost [6]. The current trend in commercial batteries is oriented towards increasing the nickel share to enhance capacity and reduce cobalt content due to environmental, cost, supply and ethical concerns. Blends of either NMCs or NCA ($LiNi_xCo_yAl_zO_2$ where x+y+z = 1) with olivine-type materials ($LiFePO_4$, $LiFe_xMn_yPO_4$, x+y = 1) or $LiMn_2O_4$ have been studied to combine the high capacity of the former with the lower cost and higher power capability of the latter [7]. For that case, improved shelf and cycle life compared to pure LMO was also achieved thanks to the mitigation of Mn dissolution [8–10]. Blends of LMO and NMC are already being widely used in commercial batteries for EV's in addition to other, less specialized applications [1,5,8,11,12].

Still today, commercial blends are primarily chosen based on empirical evidence, and the mechanistic understanding of the individual contribution of each component and their interplay remains unclear, even after several noteworthy works in the field [13,14]. According to a theoretical multi-particle model, it was proposed that the flow of current across each component in the blend is different, with the material possessing faster kinetics having a higher capacity to accommodate lithium during galvanostatic

discharge pulses. This surplus lithium is then redistributed during the subsequent relaxation period, which is commonly referred to as the ''buffer effect'' [15]. This effect was experimentally evinced by Klein et al. [16] by means of X-ray diffraction for the $LiFe_{0.3}Mn_{0.7}PO_4$ *-* $LiMn_{1.9}Al_{0.1}O_4$ *system. Heubner et al. were able to quantify it by using an electrochemical cell set-up with two working electrodes (each one with one component material of the blend) that allows to determine the current contribution of each material separately [17]. The same group applied this technique to different blend combinations LMO-NMC, LCO-LMO [18], LFP-LCO [7] and LMO-LFP [19], observing that each material is subjected to a different electrochemical load (current) with its effective C-rate often being several times higher (or lower) than the C-rate of the cell. Recently Liebmann et al. demonstrated that the basic electrochemical properties of the blend's components match those of a physical mixture model hence objecting to a systematic change of the thermodynamic and kinetic properties of the mixture [20].*

One of the few mechanistic studies on the LMO-NMC system was carried out by Kobayashi et al. using X-ray diffraction to follow the changes in the lattice parameters of the blends at low and high rates for fresh and degraded cathodes. The conclusion was that the reduction of capacity at higher rates (C/2 vs. C/20) was due to limited insertion of Li ions in NMC during discharge [21]. In agreement with previous studies they also observed Li exchange between active materials during relaxation periods between charge and discharge after extensive cycling.

Herein we present a study on the LMO - NMC-532 aiming at elucidating the synergistic effects, examine their correlation with the blend composition and investigate the redox mechanism by combining electrochemical and operando synchrotron based spectroscopic and diffraction techniques. Through the comparison and contrasting of those insights we strive to contribute to a better understanding of the working principle of such blends and advance towards a more rational approach in their design.

3.2 Experimental details

3.2.1 Electrode formulation and cell assembly

The materials used were all of commercial grade. $LiMn_2O_4$ (LMO) and $LiNi_{0.5}Mn_{0.3}Co_{0.2}O_2$ (NMC-532) were purchased from Sigma Aldrich and MTI corp., respectively. The microstructure of the two materials was quite different with $LiNi_{0.5}Mn_{0.3}Co_{0.2}O_2$ secondary particles in micrometer size (D_{50} = 10.0 − 14.0 μm) composed of primary particles exhibiting diameters smaller than 500 nm (data provided by aggregated particles with diameters around 300−500 nm and $LiMn_2O_4$ particles exhibiting diameters smaller than 500 nm (data provided by supplier and verified by SEM and TEM, see Fig. 1(a) and (b) in S.I., respectively). Slurries of the pure materials and three different LMO:NMC-532 blends were prepared, namely L25:N75, L50:N50 and L75:N25 based on their weight percentage, by dispersing the mixture of active materials in N-Methyl-2-pyrrolidone, NMP, along with Polyvinylidene fluoride, PVDF binder (Solef 5130/1001, Solvay, Belgium), and carbon additive (C65, Imerys, Switzerland) in a ratio of 84:8:8. Subsequently, and after homogenizing through vigorous stirring (ULTRA-TURRAX T25, IKA Germany) the slurries were tape casted on 18 μm Al foil as current collector. The capacity loading was generally adjusted to 1 ± 0.25 mAh cm^{-2} , except for the case of the power performance tests (Fig. 1) where it was kept to 1 ± 0.05 mAh cm^{-2} for the sake of a rigorous comparison. For the calculation of the areal capacity loadings, the expected cell capacities and the C-rate calculation, the capacity of the materials measured as C/20 in the same electrochemical window was used (167 mAh/g for NMC-532 and 121 mAh/g for the LMO).

A cross sectional micrograph of a 50:50 blend electrode is depicted in Fig. 1(c) in the S.I. In the micrograph, easily distinguishable are the micrometer sized NMC-532 particles which are homogeneously surrounded by the LMO sub-micron sized ones as evinced by elemental mapping see Fig. 1(d). Blend electrodes are compact and crack-free, which validates the quality of the tape casting process.

Electrodes consisted of discs of 14 mm diameter cut from the above mentioned tapes, which were pressed at 4 tons using a hydraulic press and subsequently dried at 120 ◦ C under vacuum for at least one hour. Afterwards and without any exposure to air they were used as working electrodes for cell assembly in an argon-filled glove-box (≤ 0.1 ppm H_2O and O_2) using a quartz fibre separator (QM-A; Whatman, 475 µm) and a 16 mm diameter lithium disc as counter-electrode. From the mass of the Lithium (≈50 mg) the capacity of the electrode was found to be 192 mAh vastly larger than the typical working electrode capacity of less than 2 mAh. The thickness of the working electrodes was found to be 60–70 µm before calendering, reducing to ≈ 50 µm after, yielding a density of ≈ 1.5 gcm^{-3} . Approximately 300 µL of a commercial 1:1 EC/DMC mixture with 1M $LiPF_6$ and 2% VC was used as electrolyte (Solvionic, France). Electrochemical performance was tested using CR2032 coin cells and cycled using a VMP-3 potentiostat-galvanostat (Bio-Logic, France) within the voltage window of 3.2 to 4.3 V vs. Li^+ / Li and at room temperature. All the post-formation reported cycles had coulombic efficiencies higher than 95 %.

The electrochemical cycling during operando measurements were carried out using a VSP potentiostat-galvanostat (Bio-Logic, France) at C/4 rate in CC mode within voltage window of 3.2 to 4.3 V vs. Li^+ / Li.

For the operando experiments, identical electrodes as for the electrochemical experiments were used with active material loading of around 7 mg cm^{-2} in a specially designed in situ cell for operando spectroscopic measurements, recently described elsewhere [22]. For the diffraction experiment CR2032 coin cells equipped with glass window were used.

3.2.2 Decoupled blended electrode setup

In order to further investigate the electrochemical stress (current load) experienced by each material in the blends, a cell setup with decoupled blend component electrodes was used with electrodes and separators identical to the previously mentioned. The assembly was done as previously described by Heubner et al., in a three electrode PFA

swagelok type cell with two electrodes containing one of the blend components each, with an appropriate active mass ratio to mimic the mixed blend (tuned by electrode diameter). The two electrodes, along with two separator discs, were placed facing each other while having a piece of perforated, properly shaped, lithium in between, as counter electrode. The same, previously discussed electrolyte was used but approximately double the amount of a coin cell (≈ 600 μL). For the measurement, two channels of a potentiostat/galvanostat (BioLogic VMP-3) were used. One of them supplied the cycling current to one of the positive electrodes, while the other held the two positive electrodes at the same potential (ΔV = 0 V) recording the current of the second electrode.

3.2.3 Operando X-ray diffraction

XRD measurements were carried out on MSPD beamline at the ALBA synchrotron using 15 keV photon energy (λ = 0.82572 Å) in transmission geometry using a MYTHEN high-throughput position sensitive detector for the 2θ range 1.5 to 61°. The cells used were specially adapted CR2032 coin cells (Institute for Applied Materials - Energy Storage Systems Karlsruhe Institute of Technology), bearing a thin glass window on both sides and a hole on the stainless steel spacer but otherwise identical to the standard ones. A VSP potentiostat-galvanostat (Bio-Logic, France) was utilized in CC/CV (1h CV + 1h OCV) mode and cells were cycled at C/4. The cells were mounted on an 8 coin cell carousel-like holder enabling sequential data acquisition [23] with an interval of 5.5 min between patterns for each cell. Structural analysis was performed by means of Rietveld refinements using the FullProf software [24]. The peaks from the Aluminium current collector were included in Le Bail mode.

3.2.4 Operando dual edge X-ray absorption spectroscopy

XAS measurements at the Ni and Mn K-edge were carried out in transmission mode at the CLAESS beamline at ALBA synchrotron. A specially designed in situ cell, recently described elsewhere [22], was placed between the first and second ionization

chambers. A focusing double-crystal Silicon (311) monochromator was used and beam size was adjusted to 3 × 1 mm (V×H). XAS spectra were continuously acquired during one complete electrochemical cycle, alternating every 10 min between the two transmission metal edges (Ni and Mn). For energy calibration, transition metal (TM) reference foils placed between the second and third ionization chambers were used. Cycling protocol and equipment was identical to the one used in the XRD measurement, excluding the OCV step.

3.2.5 Chemometric data analysis

The complete operando XAS datasets were analysed by combining Principal Component Analysis (PCA) and Multivariate Curve Resolution Alternating Least Squares (MCR-ALS) analysis, see details elsewhere [25]. The MCR-ALS analysis for XAS data set was carried out with the following constraints: non-negativity of the concentration of the components and closure (sum of the components concentrations equal to 100%) as well as single component at beginning of discharge. For Mn a less or equal to 1 closure constrain had to be used to achieve a converging fit.

3.3 Results

3.3.1 Electrochemical performance of blends

The electrochemical performance of the three different LMO:NMC blended positive electrode materials (25:75, 50:50 and 75:25 wt%) was tested against lithium metal at coin cell level and compared with that of electrodes made with only one of the components. Fig. 1 shows the measured and calculated voltage vs. capacity profiles upon discharge at different C-rates of the individual components (LMO, NMC-532) and the 50:50 wt% blend. The calculated profile capacity was achieved from the weighted average of the capacity of the two individual materials using their mass fraction as the weighting factor, as was previously reported by Jung et al. [26] (equation in S.I.). No significant differences between the expected and the experimentally obtained curves are observed at low cycling rate (C/20). However, as cycling rate is increased to 1C, 2C and 3C, a growing mismatch between them can be appreciated, which is highlighted by the yellow area in Fig. 1 . A higher average discharge voltage is observed experimentally, the magnitude of which grows with cycling rate (1, 3 and 5 mV respectively). This results in an enhanced specific capacity (vs the calculated) for 1 C, 2C and 3C of 3.5, 3.8 and 5.8 m Ah g −1 , respectively. A similar trend was observed for the L25:N75 blend depicted in Fig. 3, in the S.I.. These observations are the manifestation of the previously suggested synergistic effect achieved in the blends when compared to sum of the individual components [1,11,12] .

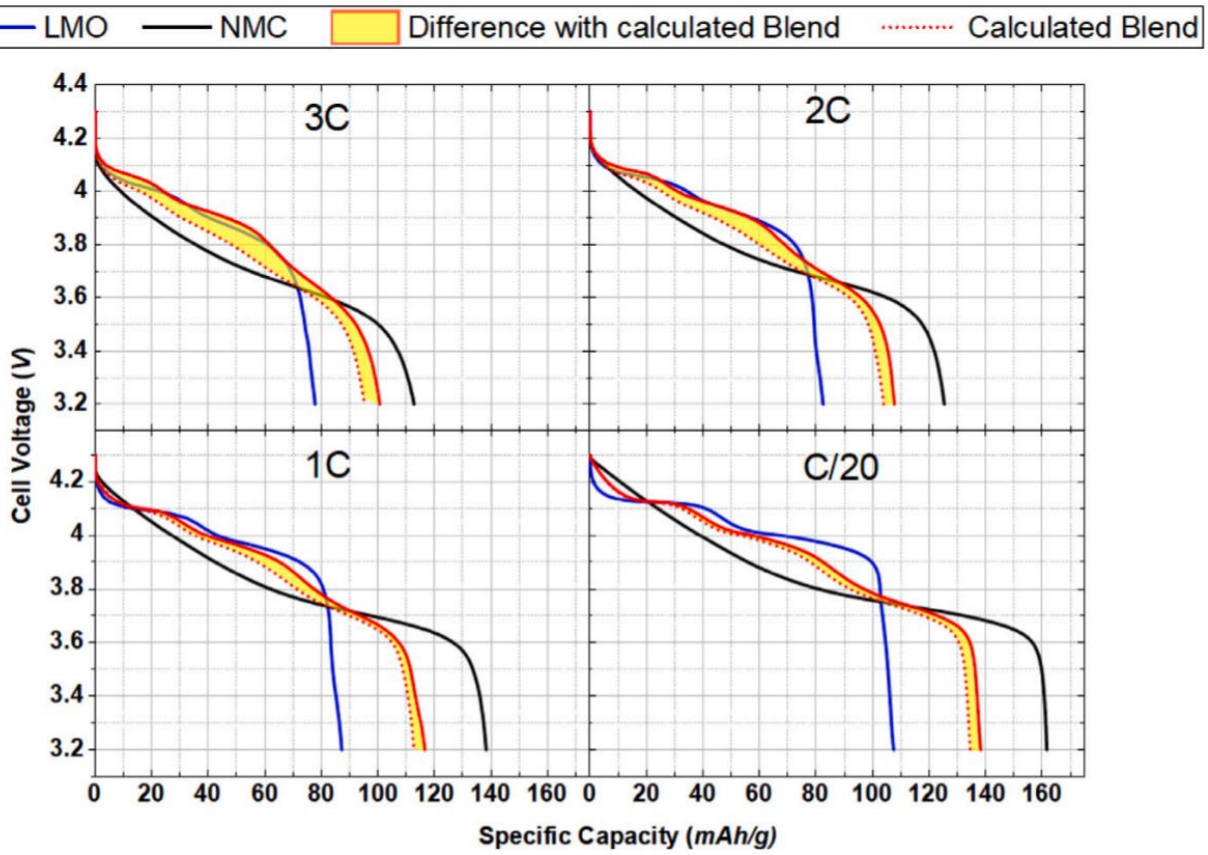

Figure 9 : Cell voltage vs specific capacity curves during discharge at different cycling rates for a L50:N50 blend (solid red line), pure LMO (blue), pure NMC-532 (black) as well as calculated blend (dotted red line). The difference between the calculated and experimentally observed electrochemical cycling curve reflecting the synergistic effect is highlighted in yellow. (For interpretation of the references to colour in this figure legend, the reader is referred to the web version of this article.)

In order to investigate the impact of blending ratio, a study on the C-rate performance and capacity retention was performed where the different blends where first subjected to multiple cycling rates (from C/20 up to 3C) followed by 100 cycles at 1C. At least four cells were used for each measurement with their loading adjusted at 1 ± 0.25 mAh cm −2 for reproducibility. Thanks to the higher discharge voltage of LMO compared to NMC-532, we witness a gradual increase of the blend's average voltage with increasing LMO content (see Fig. 2(a)). The spread of the curves gives information about the overpotential growth with faster rates and even though pure LMO is less affected by rate

than pure NMC, the results are inconclusive for the blends. In spite of the voltage benefit stemming from LMO addition, the increase in its content also results in a decrease in energy density due to its significantly lower specific capacity, see Fig. 2(b). Interestingly, the L25:N75 blend provides comparable energy density to the pure NMC532, particularly at higher rates. This blend ratio is hence of particular interest and was selected for mechanistic investigation, vide infra. It should be noted that this 25% LMO addition results not only in cost reduction but also in a more sloping electrochemical signature which could facilitate SoC estimation compared to pure NMC. Furthermore, our blend comparison results also show that by adding just 25% of NMC-532 to LMO, the cyclability of LMO, which is prone to fading, can be greatly improved up to the level of pure NMC-532, see Fig. 2 (S.I.). Such a stabilization of LMO by blending has been previously reported [5,8].

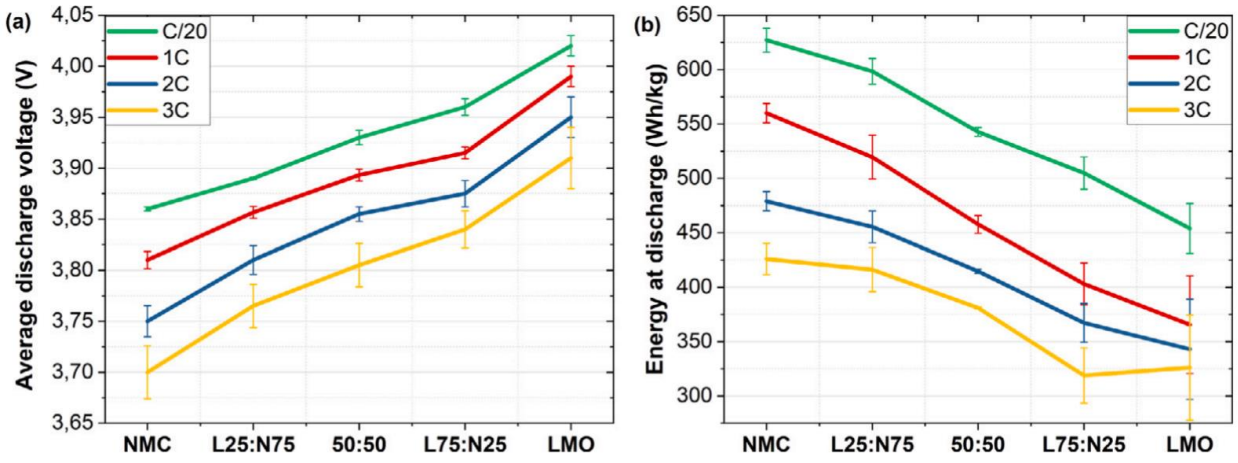

Figure 10: Comparison between single-component electrodes and L25:N75, L50:N50 and L75:N25 blends for (a) discharge voltage and (b) discharge energy at C/20, 1C, 2C and 3C. All results are averaged based on four cells, with bars depicting standard deviations.

3.3.2 Decoupled blends

For the decoupled blended electrode study, the L25:N75 and L75:N25 blends were selected and each cell was subjected to subsequent charge and discharge cycles. Fig. 3 summarizes the data corresponding to a C/5 (0.2 C) discharge, a rate comparable to the one used for the operando studies. The current recorded for each material in the

blend was divided by its theoretical capacity to obtain the effective C-rate, indicative of the real current load each electrode material is bearing.

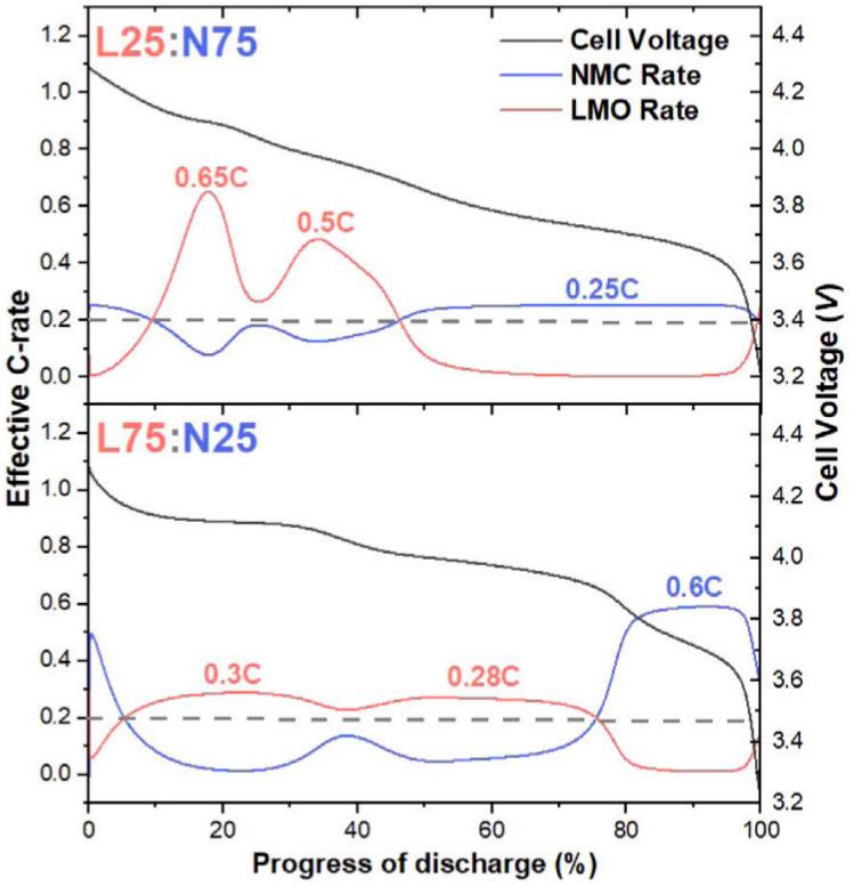

Figure 11: Decoupled blended electrode tests for L25:N75 (Top) and L75:N25 (Bottom) at C/5 (0.2C). The red (LMO) and blue (NMC-532) lines depict the effective C-rate of each electrode component, with explicit values corresponding to maximum observed C-rate. C-rates are calculated from the current flowing through each electrode component, which is divided by its capacity. The grey dashed line is the overall nominal cell current divided by the sum of the capacities of both positive electrodes (set at C/5). (For interpretation of the references to colour in this figure legend, the reader is referred to the web version of this article.)

As expected, due to their very different characteristic electrochemical curves and power capabilities, the effective C-rate of the two materials varies constantly depending on the state of charge (SoC) of the blend. The influence of the LMO voltage plateaus is

highlighted by the fact that its discharge C-rate increases drastically when the voltage of the cell coincides with them, resulting in two characteristic peaks in the effective C-rate plot. However, their maximum effective C-rate value depends strongly on the fraction of LMO in the blend. For the L25:N75, the effective rate on LMO reaches up to 0.65 C, more than three times the applied C rate and twice as high as the maximum current load for L75:N25, which peaks at 0.3 C. Also, since LMO in L25:N75 practically contributes during 40% of the overall discharge time (10%–50% of overall progress of discharge) it discharges 2.5 times faster than expected by the cell's C-rate (in 120 min instead of 300 for C/5 rate). On the other hand, NMC-532 takes most of the current load at lower SoC due to its lower average potential, the value being again highly dependent on its weight fraction in the blend. For the blend with minority share of NMC (L75:N25), it reaches three times the total applied rate of the cell. This highlights that the effective C-rate of the blend constituents can differ significantly from the nominal cell C-rate and is an important factor that should be taken into account for rational design of blended electrodes. To further understand the behaviour of each component, the decoupled blends study for the L25:N75 blend was extended to higher rates (up to 3C) and the results are shown comparatively in Fig. 4.

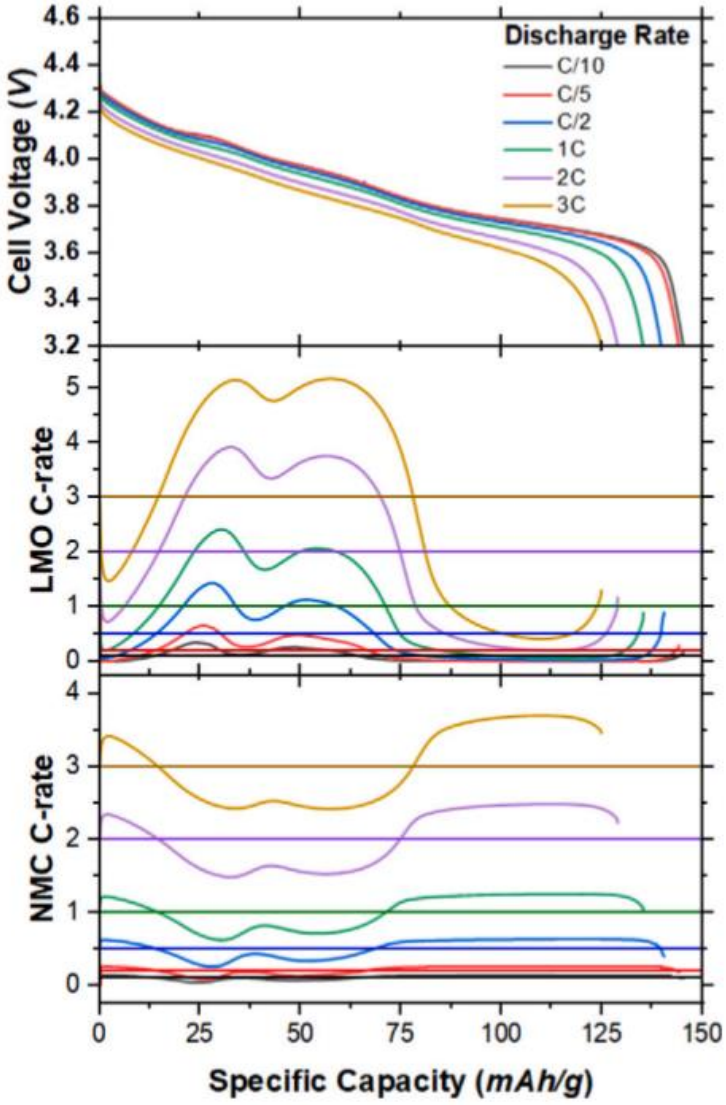

Figure 12: Decoupled Blend L25:N75 tested at multiple rates. The characteristic curves of the blend are depicted for each rate (top) and below are shown the effective Crates that were determined for each component, LMO (Middle) and NMC-532 (Bottom). Horizontal lines indicate the cell's nominal C-rate.

Immediately apparent is that the deviation of each component's effective C-rate from the cell nominal C-rate differs significantly, easily noticeable at higher rates, especially for the minority component (in this case LMO). At 3C the effective C-rate of LMO ranges from 0.4C to 5.2C while that of NMC is comprised between 2.4C to 3.7C. These data highlight that the ratio of the active components becomes even more relevant at high

C-rates. Noteworthy is also the fact that LMO maintains its characteristic double peak behaviour for all the tested rates, although experiences C-rate dependent alterations. Going to higher discharge rates causes the shift of the peaks to higher specific capacities and broadens them. Insights on the synergetic phenomena arise when one calculates the ratio between effective and nominal Crate. At 0.1C (C/10) nominal cell rate, the maximum effective C-rate experienced by LMO was found to be 0.3C, three times that of the nominal. This differs significantly from the discharge at a 3C nominal cell rate where LMO experiences a maximum slightly above 5C, only 1.7 times higher. Thus, at high rates within the range of 10–90 mAh/g where LMO is active, the two components function more cooperatively altering the load share, which leads to the performance increase observed in Fig. 1. Based on the aforementioned analysis one can conclude that on Fig. 1, the rule of mixture calculation fails to describe the properties of the blend because it assumes equal current load on both electrode components. This is not the case as LMO takes the majority of the current at high voltages (high SoC). The overpotential of the blend should be dictated mainly from the voltage of the primarily active component at the effective C-rate. Interestingly, even though blended LMO discharges at an effective C-rate significantly larger than the cell's nominal, its overpotential is comparable to the one observed for pure LMO at 3C. The resulting increase in the average discharge voltage of the blended cathode allows the retrieval of higher specific capacity values before the cell reaches its lower cut-off voltage, as seen in Fig. 1.

3.3.3 Operando XRD and XAS

Based on its better electrochemical cycling performance (vide supra), the L25:N75 blend was selected for an in-depth operando study acquiring either X-ray diffraction patterns or X-ray absorption near edge spectra (XANES) while being subjected to lithiation (discharge) or delithiation (charge) current at C/4. While XRD provides information on long-range structural changes such as phase transitions and variations

in lattice cell parameters, the XANES spectra presents insights into oxidation state and local coordination geometry changes of the probed transition metal.

The diffraction patterns in selected angular ranges for a full cycle (discharge + charge) along with the corresponding electrochemical curve are shown in Fig . 5. Gradual changes in terms of peak position and intensity are observed during charge and discharge from which the evolution of lattice parameters (and hence cell volume) and phase changes can be deduced by means of multi-phase Rietveld refinement. A single phase with $R\bar{3}m$ space group was selected to represent NMC-532 throughout the full cycle while three phases with the same, $Fd\text{-}3m$ space group were considered for LMO because it undergoes through two phase transitions.

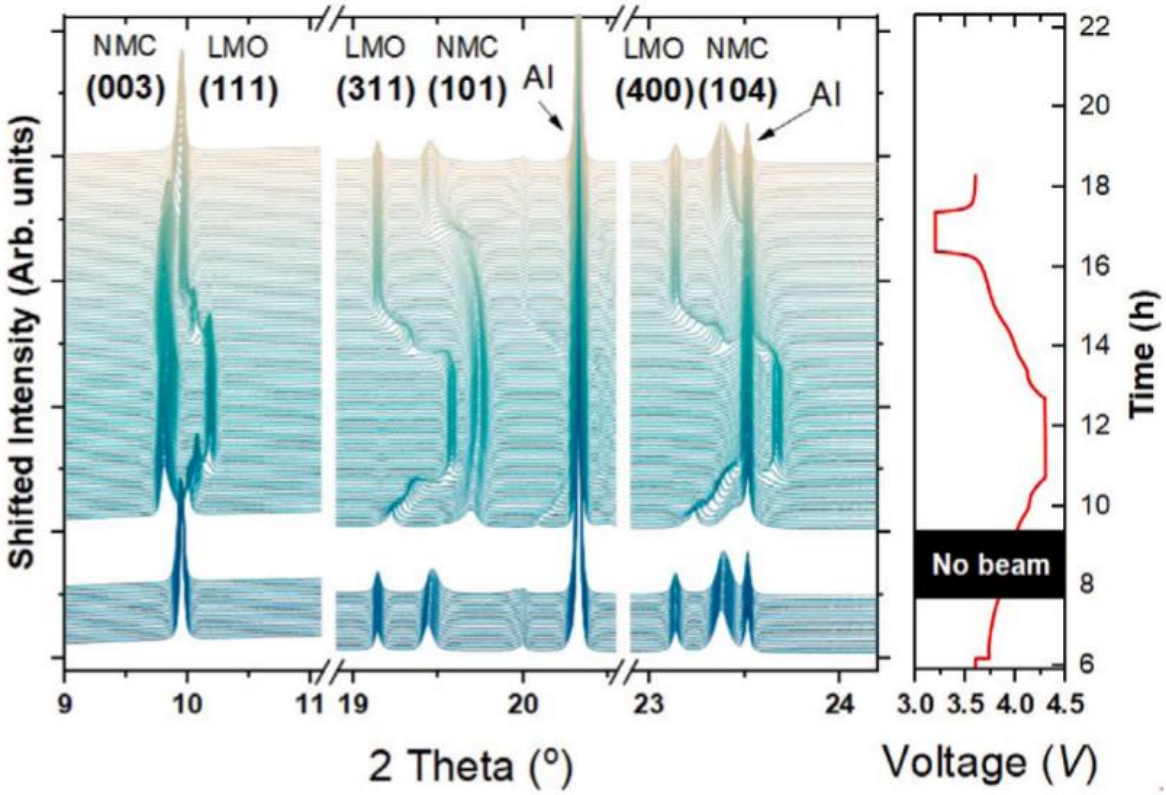

Figure 13: Evolution of diffraction patterns of a L25:N75 blend electrode operando upon discharge and charge at C/4. hkl Miller indices are given for selected peaks corresponding to NMC and LMO phase. Peaks corresponding to Al current collector are also indicated. Blank area marks a period of beam loss.

The refinement of the diffraction patterns reveals that the cell volume of both materials decreases during charge (delithiation), expressed by a general shift of diffraction peaks to higher angles. An exception to this is the (003) peak of the NMC-532 phase, as an increase in interlayer distance is observed, in agreement with the literature [27]. This specificity of NMC-532 (and all layered oxides in general) is commonly explained by the increasing electrostatic repulsion between the positively charged MO 6 slabs. It has been reported that the interlayer distance reduces abruptly at high delithiation degree caused by the decrease of the repulsion between O −2 layers as the metal-oxygen bonds become more covalent [28,29]. In our operando diffraction data we only see the onset of this effect at the upper cut-off voltage at 4.3 V. Regardless of this c cell parameter increase, while a and b decrease, as evidenced by the (101) and (104) peaks shift towards higher angles, an overall monotonically cell volume contraction upon charge occurs.

While a continuous shift in the peak positions is observed for NMC532, in agreement with a single phase reaction mechanism involving the formation of a solid-solution, a different evolution is observed for the LMO (111) peak, in agreement with its well known redox mechanism involving two successive phase transitions during charge (i.e. different LMO phases, differing in Li content, co-exist for the same SoC). To monitor changes as a function of SoC, the global LMO cell volume was calculated as the weighted average of the cell volumes of the co-existing LMO phases and is depicted as solid red lines without markers in Fig. 7 together with that of NMC-532 (bottom and top respectively). The evolution of phase weight fractions is depicted in Fig. 4 in S.I. The trends observed upon charge are fully reversed during the discharge (lithiation) in agreement with the high reversibility of the structural changes of NMC-532 and LMO.

To obtain complementary information on the local structure and electrochemical activity of the redox active transition metal (TM) the L25:N75 blend was also investigated by

dual edge operando XAS under similar experimental conditions, however starting with pre-charged cells.

The evolution of both Mn and Ni XANES K-edges upon delithiation and lithiation are depicted in Fig. 6 along with the corresponding electrochemical curve. It should be noted that XAS spectra represent the sum of all absorbers within the beam path, hence, for a LMO:NMC blend, the Mn K-edge will comprise both the LMO and NMC-532 contribution, while for Ni K-edge NMC-532 is the only contributing species. A gradual shift to lower energies is observed upon discharge (lithiation) for both TM edges which reflects the lowering of the mean oxidation state of the TM. Interestingly the main spectral changes of the two TM do not coincide. While for the Mn edge (Fig. 6, left) the main changes are observed during the first few spectra (≤#6), the changes on the Ni edge are strongest towards the end of the discharge (#8 to 14). This underlines the usefulness of element specific XANES analysis as in the electrochemical curve no distinct plateaus can be identified and the slope changes are barely visible. Upon charge (delithiation, >#16) the observed changes are largely reversed, which suggests a good reversibility of the TM redox reaction.

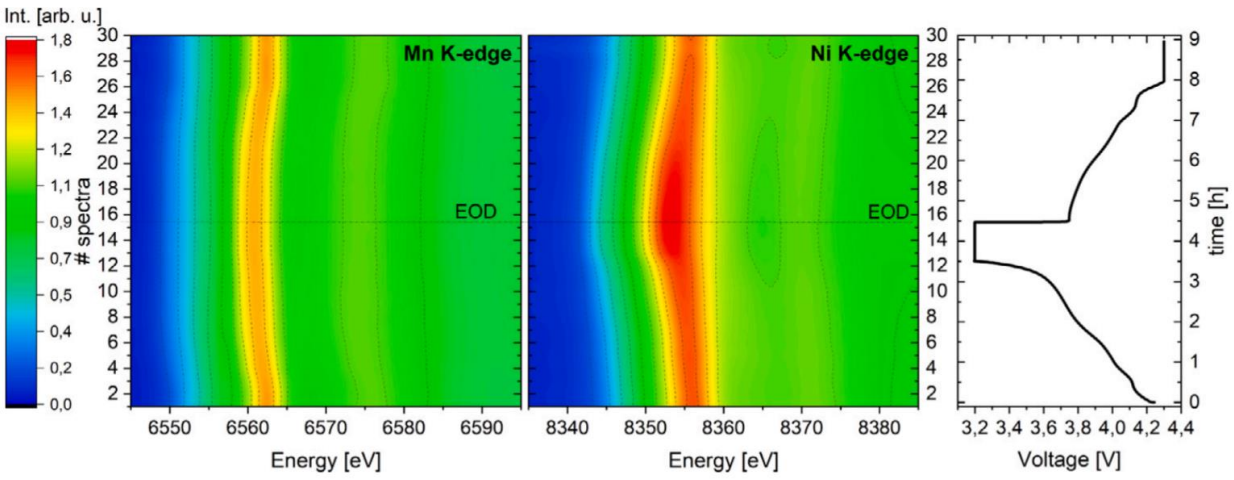

Figure 14: Evolution of Mn (left) and Ni (right) K-edge XANES spectra upon discharge and charge under operando conditions.

These spectral data sets were further analysed using a statistical tool based on PCA followed by MCR-ALS, see Fig. 6 in S.I. The results obtained suggest that the full spectral data set of Ni K-edge can be reproduced with a linear combination of three components. This is well in line with the expected reduction of Ni^{+4} to Ni^{+2} via the intermediate Ni^{+3} phase upon NMC-532 discharge, see Fig. 7(top). For Mn K-edge the spectral changes can be reproduced analogously using two components which is in agreement with the expected reduction of Mn^{+4} to $Mn^{+3.5}$ during LMO lithiation. It should be noted that the statistical approach used for the concentration profile plotting only takes into consideration the spectral changes in the data set. Absorbing atoms that do not change their coordination geometry and /or chemical state leading to spectral alterations are hence not considered. Interestingly, the closure condition (sum of components equal to one) could not be achieved for the Mn spectral data set unlike for Ni. This indicates that there are additional spectral changes which are not considered by the evolution of the two components. It is likely that these additional unaccounted for spectral changes originate from the Mn in the NMC-532, which represents ≈ 46% of the total Mn present in the blend electrode. Although the Mn in NMC-532 is not expected to undergo any change in the oxidation state, it experiences alterations in its ligand field caused by the reduction and oxidation of the redox active Ni in its vicinity which result in alterations of the Mn K-edge XANES spectra [30,31], as we have recently evidenced for another high voltage positive electrode material [32]. This hypothesis is also supported by the fact that the largest mismatch between closure condition equal to one and the sum of the two Mn components is found between spectra #10 to 20, which is the region where the strongest Ni spectral changes occur, see dotted line with hollow markers in Fig. 7 (bottom). The pure Ni and Mn XANES spectral components associated to the concentration profiles depicted in Fig. 7 are shown in Fig. 7 of the S.I. along with metal oxide reference spectra to fingerprint their approximate oxidation state. The results depicted in this figure strengthen the assumption that the three Ni components can be roughly ascribed to the Ni^{+2} , Ni^{+3} and Ni^{+4} in NMC-532. In fact a good agreement between Ni comp2 and Ni^{+2} reference is found, underlining that at EOD (End of Discharge) the most reduced state of Ni is prevalent which is closest to the

Ni^{+2} state. The deviation from the Ni^{+2} is a consequence of the presence of Ni^{+3}. As Mn and Co have oxidation states equal to +4 and +3 respectively and the average oxidation state of the TMs in NMC is +3, the Ni^{+2} /Ni^{+3} ratio changes depending on the Ni and Mn contents. Thus, Ni^{+3} will be present in pristine NMC's with a content of Ni higher than that of Mn [6,30]. Furthermore, a good agreement is found for Ni comp3 and the Ni^{+3} reference, which accentuates that the formation of a transient phase with an approximate oxidation state of Ni^{+3} occurs. The fingerprint comparison also reveals that, at EOC, at which Ni comp1 is prevalent, the Ni^{+4} state is not reached which suggests an incomplete delithiation. Such incomplete delithiation is to be expected in regard of conservative cycling conditions used here to avoid detrimental structural rearrangement of the NMC phase at high SoC, and has been reported in previous operando XAS experiments [30].

Absorption edge position of both pure spectral components of Mn are between the Mn-oxide references of $Mn^{+3.5}$ and Mn^{+4} . Component 2 is prevalent at EOD and has the oxidation state closest to $Mn^{+3.5}$

reference. This is in agreement with the fact that the mean oxidation state of Mn includes roughly a mix of 55 to 45% of $Mn^{+3.5}$ in LMO and Mn^{+4} of the NMC. Upon delithiation component 1 is formed at higher energies compared to component 2, indicating a higher oxidation state, in agreement with the oxidation of the LMO. Interestingly, the edge position of component 1 is slightly lower than the Mn^{+4} reference, which could originate from an incomplete delithiation of the LMO upon charge reaction at the applied cut-off voltage of 4.3 V.

The findings of operando XRD and XANES analyses are summarized in Fig. 7 which depict the correlation between oxidation state and unit cell volume for Ni phase (top) and Mn phase (bottom), respectively. It is remarkable that even though these data come from two independent experiments the gradual growth of the NMC-532 unit cell volume upon lithiation (discharge) is fully congruent with the rise of intermediate nickel component 3, which reflects the reduction of Ni^{+4} to Ni^{+3} , see Fig. 7(top). Upon further

lithiation beyond 50 mAh/g an accelerated increase in the NMC-532 lattice volume is observed which coincides with the steep rise of nickel component 2, reflecting the formation of completely reduced Ni^{+2}. Upon subsequent charge (delithiation) up to 100 mAh/g capacity an equally good overlap between the sharp decrease in NMC unit cell volume and the decline of component 2 is observed. Lithiation beyond this capacity results in a less steep shrinkage of lattice volume, which analogous to the discharge reaction, coincides with the formation of the intermediate Ni^{+3} (component 3). Towards the end of charge a steep decline of both cell volume and concentration of intermediate component 2 are observed. Interestingly, an asymmetry between discharge and charge is observed both for the Rietveld refinement derived volume change and the XAS derived concentration profiles, which could be due to overpotential build-up. Such a good agreement between two separate operando experiments is remarkable and underlines the reproducibility of the experimental findings.

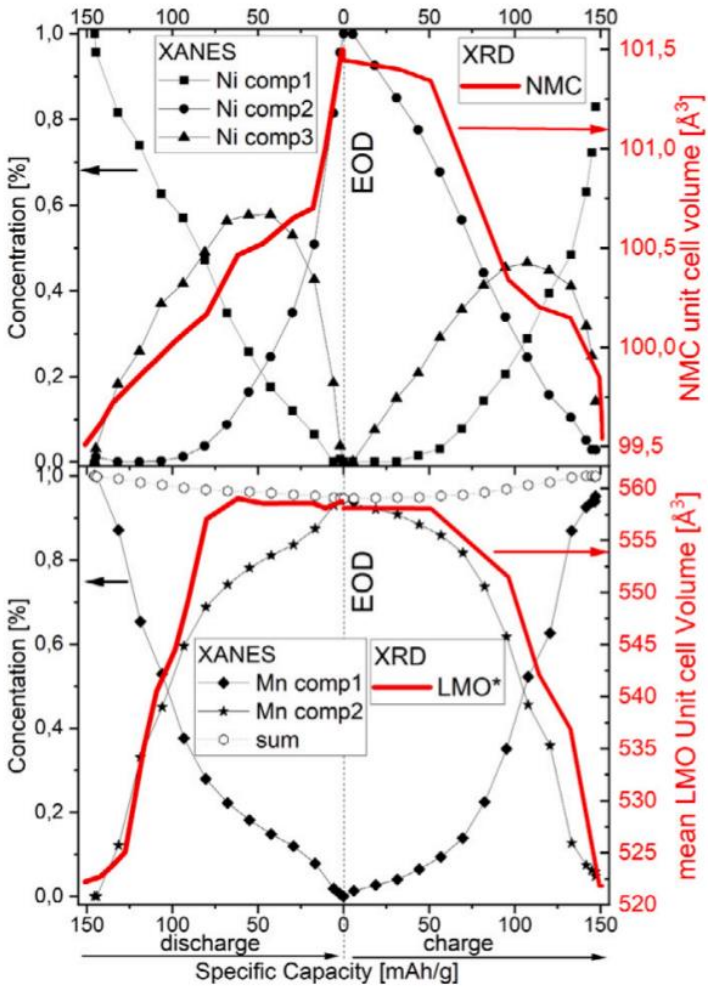

Figure 15: Concentration profiles based on XANES analysis (black line with markers) for Ni (top) and Mn (bottom) and unit cell volume evolution (solid red lines without markers) based on operando XRD for NMC-532 (top) and LMO (bottom) as function of specific capacity. The dashed line with hollow markers in bottom figure represents the sum of the two XANES-derived Mn components. The mean LMO unit cell volume was calculated by multiplying the lattice volume of individual LMO phases with their corresponding phase fraction. The vertical dashed line indicates the end of discharge (EOD). (For interpretation of the references to colour in this figure legend, the reader is referred to the web version of this article.)

The Mn XAS and XRD LMO data illustrate that the main unit cell volume change and oxidation state changes occur in the capacity range of 150 to 100 mAh/g during discharge, and 100 to 150 mAh/g during charge. Within this range, the rapid decay of Mn component 1 and the rise of component 2 occurs, reflecting the reduction from Mn^{+4}

to $Mn^{+3.5}$ and a rapid increase in mean unit cell volume of the LMO phases. In the capacity range from 100 mAh/g discharge to 100 mAh/g charge a single LMO crystal phase is prevalent (see Fig. 4 S.I. for individual phase volumes and fractions), for which only minor volume changes are observed. This is well in line with the broad maximum of the spectroscopic species Mn component 2, reflecting the redox inactivity of the Mn TM in this region.

In summary, our combined XAS and XRD analysis shows that during charge (delithiation) of a L25:N75 blend the subsequent oxidation of firstly Ni and secondly Mn occurs which is accompanied by a contraction of the cell volume for both components (NMC-532, LMO). This sequence is reversed upon discharge.

To visualize the correlation between the redox mechanism progression and the fluctuating effective current load in the L25:N75 blend electrode, the rate of change of oxidation state of Mn (based on XANES) and of the LMO unit cell volume (based on XRD) are superimposed with those of effective C-rate on LMO in Fig. 8(a). A general agreement between the effective C-rate on the LMO and the oxidation state changes of the Mn K-edge is found depicting a twin peak, despite a much lower resolution of the latter and slightly higher applied C-rate (C/4 instead of C/5). In fact the maxima at ≈15 and 35% of SOD of the effective current rate on LMO phase are well aligned with the maxima and shoulder peak position of the Mn K-edge change rates. This confirms that when LMO phase bears highest current rate it undergoes the fastest redox reaction. To further support this claim, the normalized unit cell volume of a pure LMO electrode (see Fig. 5 in S.I.) as determined from operando XRD refinements at C/4 are plotted as a function of discharge time alongside those of the L25:N75 blend Fig. 8(b). There is an apparent difference in the behaviour of the normalized unit cell volume of LMO in pure compared to blended electrode. Even though the start and end points are similar, blended LMO is active only during the first 2 h (or approx. 50% SOD) as also observed in the decoupled blend study. In an effort to quantify the difference in the reaction rate, the most active regions of each curve were linearly fit in order to calculate an average rate of change (expressed as Å/h) of LMO normalized unit cell volume. An ≈ 2,8-fold

increase in reaction rate was observed when the material is in the L25:N75 blend (25 Å/h compared to 9 Å/h), very close to the 2.5-fold increase observed in the decoupled blend study (vide supra).

It should be noted that the sharp twin peak behaviour of the effective rate across the LMO phase depicted in Fig. 8(a) is specific to the L25:N75 blend ratio. Increasing the LMO content in the blend is expected to lower the peak maxima and increase the width of the peaks, as observed for the L75:N25 blend (vide supra). In the extreme case of a pure LMO electrode a constant rate is to be expected, equal to the cell's rate. Interestingly, a similar trend of twin peaks is also observed for the change rate of the Rietveld-refined LMO unit cell volume. However, in this case, the peaks are slightly shifted to higher SOD which suggests that the phase transformation reaction is somewhat delayed with respect to the effective current load and oxidation state changes. This delay between XAS and XRD has been previously attributed to domain growth [33]. Nevertheless the general agreement between the three independent experiments (decoupled electrode, operando XAS and operando XRD) underlines the reliability of our findings.

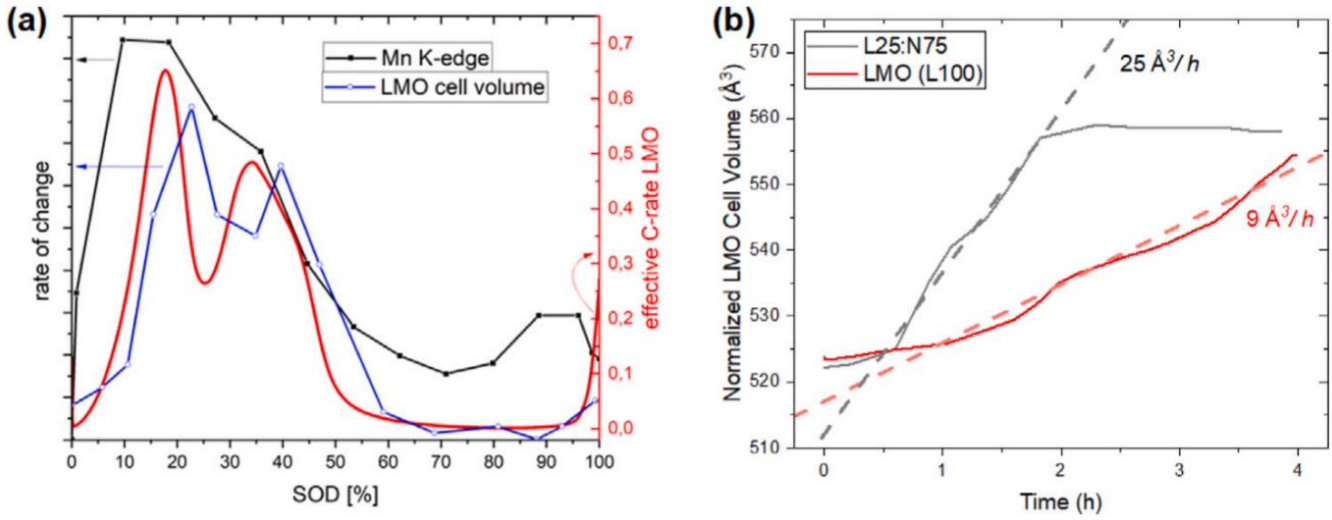

Figure 16: (a) Rate of change of Mn oxidation state (black line with square markers) and LMO normalized unit cell volume (blue line with hollow spherical markers) along with effective current load rate on LMO (solid red line) as function of state of discharge (SOD) for a L25:N75 blend electrode. (b) LMO normalized

unit cell volume as a function of discharge time (at C/4) for the cell with the blended L25:N75 electrode (grey line) and one with pure LMO electrode (red line). The most active regions were linearly fit (dashed lines) and their slope is reported. (For interpretation of the references to colour in this figure legend, the reader is referred to the web version of this article.)

3.4 Conclusions

Our results confirm that blending NMC with LMO is a viable approach to unlock synergistic effects in terms of energy density, rate capability and cycling stability. We find that the effective current load on each blend component greatly differs both as function of SoC as well as of its share in the mixture. In this regard, we have demonstrated that the minority component is subjected to a much higher effective current load resulting in higher electrochemical stress. It is hence crucial for rational blend design to select a minority component with fast reaction kinetics in order to yield to a net performance gain. We highlight that these effective current load peaks spur the redox and phase change reaction. Furthermore the operando diffraction and spectroscopic analysis confirms that the reaction mechanism occurs via phase transition involving the Mn +3⁄4 redox couple in the LMO and via solid solution mechanism involving Ni +2⁄4 redox couple with a transient Ni^{+3} in the NMC. Moreover, we underline the correlation between lattice contraction and expansion upon oxidation and reduction of the redox active TM. The dual edge XAS unveils that the Mn +3⁄4 reaction in LMO overlaps with the Ni +3⁄4 reaction in NMC, while the Ni +2⁄3 redox reaction occurs at a lower voltage range. Overall these findings enhance the understanding of the mechanisms involved and encourage a more methodical approach to designing blend electrodes and emphasize the need for additional research across a broader range of compositions to strengthen insights and inform the design process effectively.

3.5 Supporting Information

The mathematical formula used to determine the calculated characteristic curve of a blend consisting of two components a and b is:

$$C_{blend}(V) = f_a C_a(V) + f_b C_b(V)$$

where: $C_{blend}(V)$ is the expected specific capacity of the blend at each voltage V, C_a and C_b the specific capacities of the components a and b respectively at the same voltage V, as determined by electrodes with pure materials, and f_a, f_b the relative fractions of a and b in the active mass of the blend.

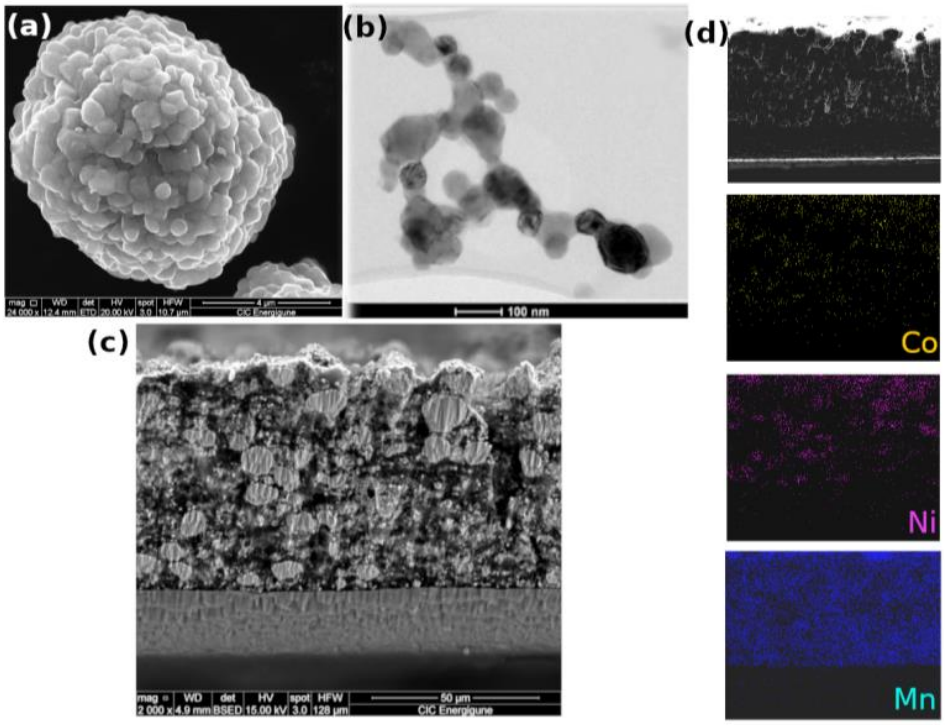

Figure S.I. 6: (a) SEM of micrometer NMC-532 (b) TEM of nanometer LMO (c) cross sectional SEM image of a 50:50 LMO-NMC blend. Large micrometer sized particles correspond to NMC while smaller submicrometer particles consist of LMO (d) SEM of 50:50 LMO-NMC blend and corresponding elemental maps of Co, Ni and Mn from top to bottom.

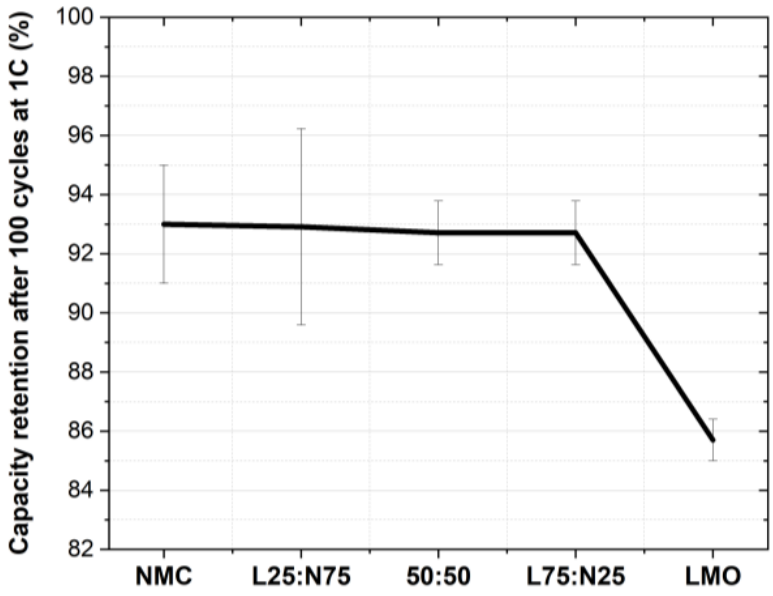

Figure S.I. 7: Capacity retention after 100 cycles at 1C for the pure materials as well as the blends studied.

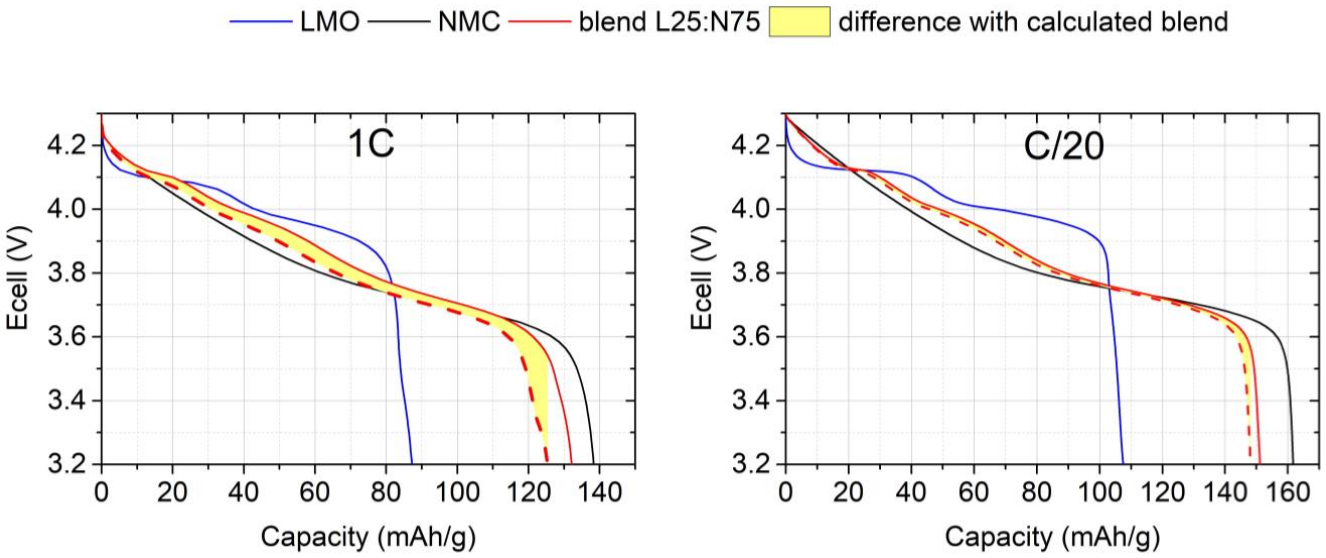

Figure S.I. 8: Cell Voltage vs specific capacity during discharge for L25:N75 blend at C/20 (right) and 1C (left) showing the difference between the calculated (dashed red line) and measured curves (solid red line).

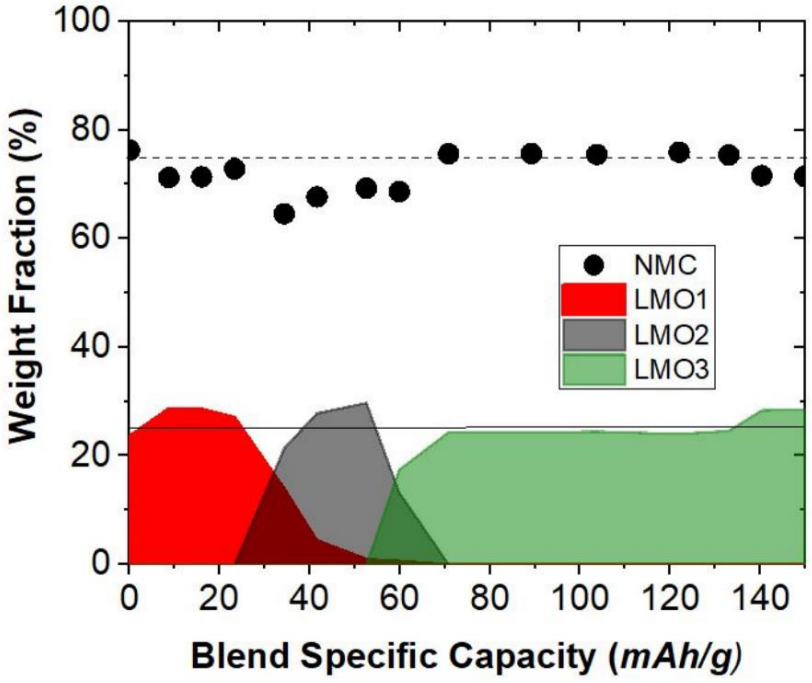

Figure S.I. 9: Phase fractions of LMO and NMC cathode blends upon discharge. Upon charge no phase coexistence of LMO was observed.

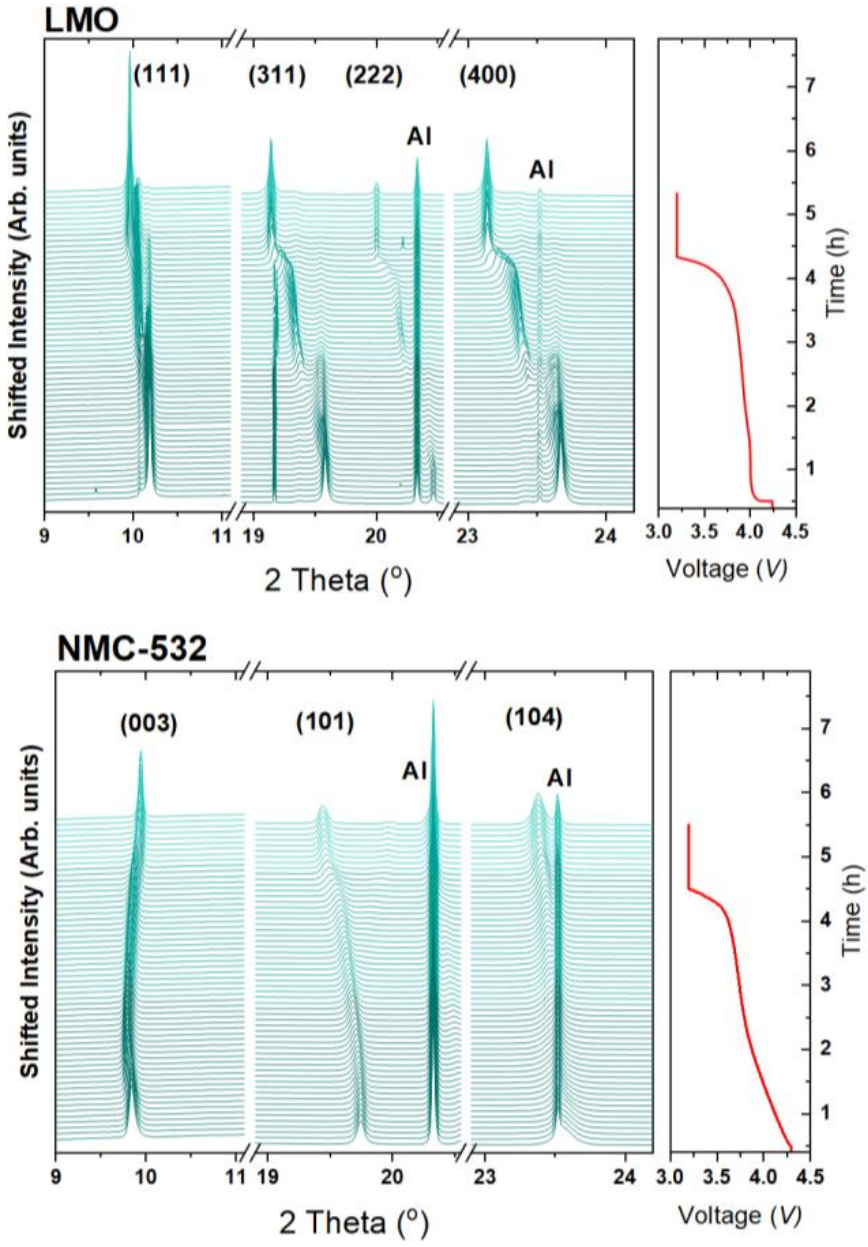

Figure S.I. 10 : Evolution of diffraction patterns of a pure LMO electrode (top) and a pure NMC-532 one (bottom) operando upon discharge at C/4. hkl Miller indices are given for the peaks of LMO and NMC-532. Peaks corresponding to Al current collector are also indicated.

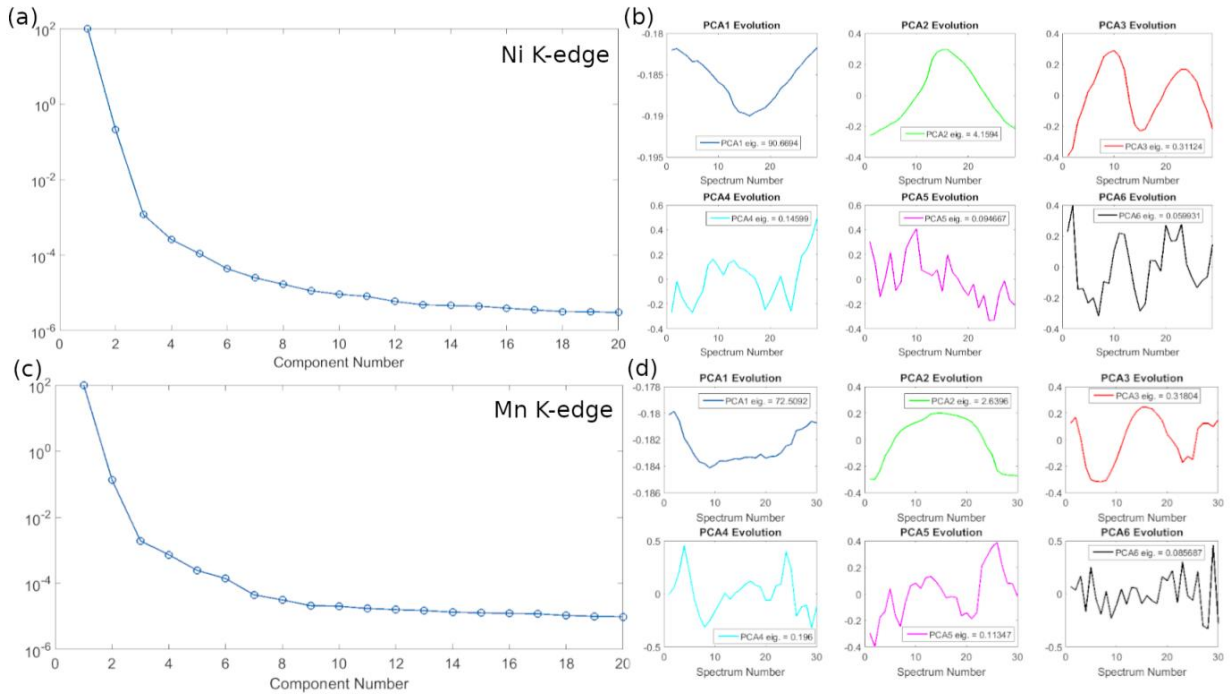

Figure S.I. 11 : PCA derived (a & c) evolution of eigenvalue components in order of decreasing variance and (b & d) evolution of first 6 components throughout the operando experiment for Ni and Mn, respectively.

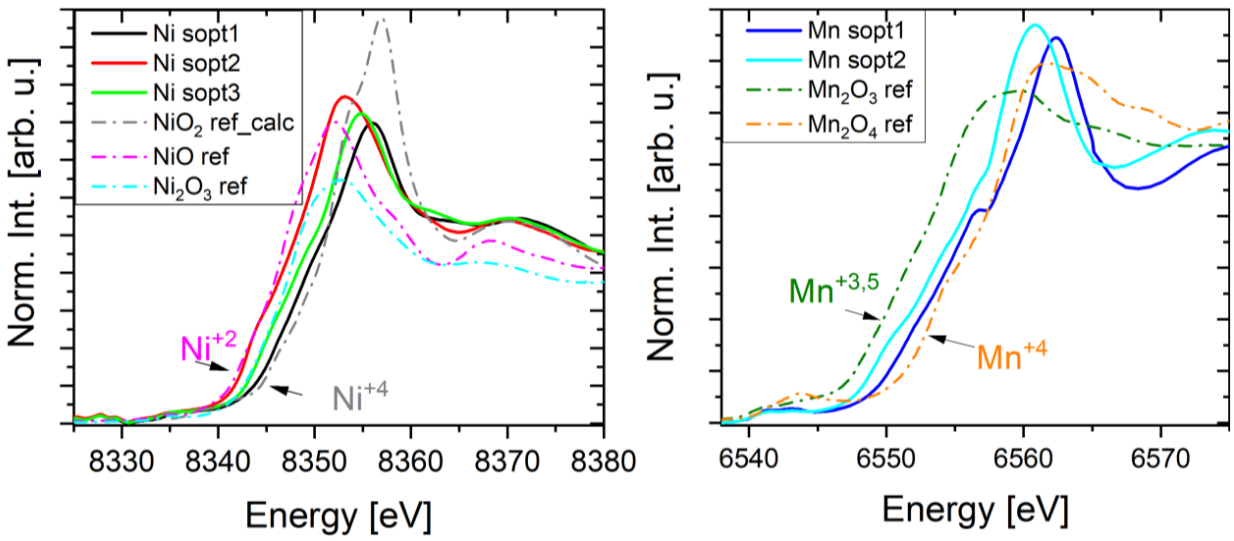

Figure S.I. 12: XANES pure spectral components (sopt) for Ni (left) and Mn (right) along with experimental obtained TM-oxide reference spectra. For Ni^{+4} a calculated reference spectra was used as this oxidation state is highly unstable and exist only in very few compounds.

Acknowledgements

Operando experiments were performed at MSPD & CLAESS beamlines (proposal 2021035098 and 2021095303) at ALBA Synchrotron with the collaboration of ALBA staff. Authors are grateful to ALISTORE ERI and to H. Ehrenberg and his team at KIT for providing access to the 8 coin cell carousel holder. ICMAB-CSIC members thank the Spanish Agencia Estatal de Investigación Severo Ochoa Programme for Centres of Excellence in R&D, Spain (CEX2019-000917-S) and funding through grant PID2020-113805GB-I00. This work has been done in the framework of the doctorate in Materials Science of the Universitat Autònoma de Barcelona and D.C. wants to acknowledge DESTINY MSCA PhD Programme. Authors acknowledge support of the publication fee by the CSIC Open Access Publication Support Initiative through its Unit of Information Resources for Research (URICI). This project has received funding from the European Union's Horizon 2020 research and innovation programme under Grant Agreement No 945357.

References

1. *J. Wang, Y. Yu, B. Li, P. Zhang, J. Huang, F. Wang, S. Zhao, C. Gan, J. Zhao, ACS Appl. Mater. Interfaces 8 (31) (2016) 20147–20156, http://dx.doi.org/10.1021/acsami.6b06976.*
2. *H.Y. Tran, C. Täubert, M. Fleischhammer, P. Axmann, L. Küppers, M. WohlfahrtMehrens, J. Electrochem. Soc. 158 (5) (2011) A556, http://dx.doi.org/10.1149/ 1.3560582.*
3. *H. Kookjin, I. Jehong, L. Jeong-Seon, J. Jeonggeon, K. Seokhun, K. Jaekook, L. Jinsub, J. Electrochem. Sci. Technol. 11 (3) (2020) 282–290, http://dx.doi.org/10.33961/jecst.2019.00661, URL: http://www.jecst.org/journal/view.php?number=334, arXiv:http://www.jecst.org/journal/view.php?number=334.*
4. *A. Klein, P. Axmann, M. Wohlfahrt-Mehrens, J. Power Sources 309 (2016) 169–177, http://dx.doi.org/10.1016/j.jpowsour.2016.01.093.*
5. *A.J. Smith, S.R. Smith, T. Byrne, J.C. Burns, J.R. Dahn, J. Electrochem. Soc. 159 (10) (2012) A1696–A1701, http://dx.doi.org/10.1149/2.056210jes.*
6. *M. Dixit, B. Markovsky, F. Schipper, D. Aurbach, D.T. Major, J. Phys. Chem. C (2017-10-06) http://dx.doi.org/10.1021/acs.jpcc.7b06122, URL:https://pubs.acs.org/doi/pdf/10.1021/acs.jpcc.7b06122, Archive Location: world Publisher: American Chemical Society.*
7. *C. Heubner, T. Liebmann, C. Lämmel, M. Schneider, A. Michaelis, ChemElectroChem 5 (3) (2018) 425–428, http://dx.doi.org/10.1002/celc.201700997.*
8. *H. Kitao, T. Fujihara, K. Takeda, N. Nakanishi, T. Nohma, Electrochem. Solid-State Lett. 8 (2) (2004) A87, http://dx.doi.org/10.1149/1.1843792.*
9. *H.Y. Tran, C. Täubert, M. Wohlfahrt-Mehrens, Prog. Solid State Chem. 42 (4) (2014) 118–127, http://dx.doi.org/10.1016/j.progsolidstchem.2014.04.006, URL: https://www.sciencedirect.com/science/article/pii/S0079678614000156, Functional materials and analytics for high performance lithium ion batteries.*

10. T. Numata, C. Amemiya, T. Kumeuchi, M. Shirakata, M. Yonezawa, J. Power Sources 97–98 (2001) 358–360, http://dx.doi.org/10.1016/S03787753(01)00753-4, URL: https://www.sciencedirect.com/science/article/pii/ S0378775301007534, Proceedings of the 10th International Meeting on Lithium Batteries.
11. S.K. Jeong, J.S. Shin, K.S. Nahm, T. Prem Kumar, A.M. Stephan, Mater. Chem. Phys. 111 (2) (2008) 213–217, http://dx.doi.org/10.1016/j.matchemphys. 2008.03.032, URL: https://www.sciencedirect.com/science/article/pii/ S0254058408001417.
12. D. Wu, H. Ren, Y. Guo, X. Zhang, Z. Zhang, J. Li, Ionics 25 (4) (2019) 1595–1605, http://dx.doi.org/10.1007/s11581-018-2650-z.
13. S.B. Chikkannanavar, D.M. Bernardi, L. Liu, J. Power Sources 248 (2014) 91–100, http://dx.doi.org/10.1016/j.jpowsour.2013.09.052, URL: https://www.sciencedirect.com/science/article/pii/S0378775313015486.
14. M. Casas-Cabanas, A. Ponrouch, M.R. Palacín, Isr. J. Chem. 61 (1–2) (2021) 26–37, http://dx.doi.org/10.1002/ijch.202000099.
15. Z. Mao, M. Farkhondeh, M. Pritzker, M. Fowler, Z. Chen, Electrochim. Acta 222 (2016) 1741–1750, http://dx.doi.org/10.1016/j.electacta.2016.11.169.
16. A. Klein, P. Axmann, M. Wohlfahrt-Mehrens, J. Electrochem. Soc. 163 (9) (2016) A1936–A1940, http://dx.doi.org/10.1149/2.0741609jes.
17. C. Heubner, T. Liebmann, C. Lämmel, M. Schneider, A. Michaelis, J. Power Sources 363 (2017) 311–316, http://dx.doi.org/10.1016/j.jpowsour.2017.07. 108.
18. C. Heubner, T. Liebmann, C. Lämmel, M. Schneider, A. Michaelis, J. Energy Storage 20 (2018) 101–108, http://dx.doi.org/10.1016/j.est.2018.09.003.
19. T. Liebmann, C. Heubner, C. Lämmel, M. Schneider, A. Michaelis, ChemElectroChem 6 (22) (2019) 5728–5734, http://dx.doi.org/10.1002/celc.201901554.
20. T. Liebmann, C. Heubner, M. Schneider, A. Michaelis, Mater. Today Energy 22 (2021) 100845, http://dx.doi.org/10.1016/j.mtener.2021.100845.
21. T. Kobayashi, Y. Kobayashi, H. Miyashiro, J. Mater. Chem. A 5 (18) (2017) 8653–8661, http://dx.doi.org/10.1039/C7TA02056B.

22. *D. Saurel, A. Pendashteh, M. Jáuregui, M. Reynaud, M. Fehse, M. Galceran, M. Casas-Cabanas, Chem. Methods 1 (6) (2021) 249–260, http://dx.doi.org/10.1002/cmtd.202100009, URL: https://chemistry-europe.onlinelibrary.wiley.com/doi/abs/10.1002/cmtd.202100009.*
23. *M. Herklotz, J. Weiß, E. Ahrens, M. Yavuz, L. Mereacre, N. KiziltasYavuz, C. Dräger, H. Ehrenberg, J. Eckert, F. Fauth, L. Giebeler, M. Knapp, J. Appl. Crystallogr. 49 (1) (2016) 340–345, http://dx.doi.org/10.1107/ S1600576715022165.*
24. *J. Rodríguez-Carvajal, Physica B 192 (1) (1993) 55–69, http://dx.doi.org/10.1016/0921-4526(93)90108-I, URL: https://www.sciencedirect.com/science/ article/pii/092145269390108I.*
25. *M. Fehse, A. Iadecola, M.T. Sougrati, P. Conti, M. Giorgetti, L. Stievano,Energy Storage Mater. 18 (2019) 328–337, http://dx.doi.org/10.1016/j.ensm.2019.02.002, URL: https://www.sciencedirect.com/science/article/pii/S2405829719300431.*
26. *S. Jung, J. Power Sources 264 (2014) 184–194, http://dx.doi.org/10.1016/j.jpowsour.2014.04.072.*
27. *R. Weber, C.R. Fell, J.R. Dahn, S. Hy, J. Electrochem. Soc. 164 (13) (2017) A2992, http://dx.doi.org/10.1149/2.0441713jes.*
28. *T. Liu, L. Yu, J. Lu, T. Zhou, X. Huang, Z. Cai, A. Dai, J. Gim, Y. Ren, X. Xiao, M.V. Holt, Y.S. Chu, I. Arslan, J. Wen, K. Amine, Nature Commun. 12 (1) (2021) 6024, http://dx.doi.org/10.1038/s41467-021-26290-z, URL: https://www.nature.com/articles/s41467-021-26290-z , Number: 1 Publisher: Nature Publishing Group.*
29. *T. Li, X.-Z. Yuan, L. Zhang, D. Song, K. Shi, C. Bock, Electrochem. Energy Rev. 3 (1) (2020-03-01) 43–80, http://dx.doi.org/10.1007/s41918-019-00053-3.*
30. *K.R. Tallman, G.P. Wheeler, C.J. Kern, E. Stavitski, X. Tong, K.J. Takeuchi, A.C. Marschilok, D.C. Bock, E.S. Takeuchi, J. Phys. Chem. C 125 (1) (2021) 5873, http://dx.doi.org/10.1021/acs.jpcc.0c08095, Publisher: American Chemical Society.*

31. *Y.-N. Zhou, X. Yu, J. Liu, J. Bai, E. Dooryhee, Z.-W. Fu, E. Hu, H. Li, L.G. and* Kyung-Wan Nam, S.-M. Bak, X.-Q. Yang, Adv. Energy Mater. 6 (2016) 1600597, URL: https://onlinelibrary.wiley.com/doi/abs/10.1002/aenm.201600597.*
32. *M. Fehse, N. Etxebarria, L. Otaegui, M. Cabello, S. Martín-Fuentes, M.A. Cabañero, I. Monterrubio, C.F. Elkjaer, O. Fabelo, N.A. Enkubari, J.M. López del Amo, M. Casas-Cabanas, M. Reynaud, Chem. Mater. 34 (14) (2022) 6529–6540, http://dx.doi.org/10.1021/acs.chemmater.2c01360.*
33. *H. Arai, K. Sato, Y. Orikasa, H. Murayama, I. Takahashi, Y. Koyama, Y. Uchimoto, Z. Ogumi, J. Mater. Chem. A 1 (2013) 10442–10449, http://dx.doi.org/10.1039/C3TA11637A.*

4. Addressing first cycle irreversible capacity in lithium-rich layered oxides by blending them with delithiated active materials

4.1 Introduction

As efforts towards sustainable transportation intensify, Electric Vehicles (EVs) become more and more popular as they provide the means of moving away from fossil fuels. Even though great progress has been made in automotive engineering, leading to commercially available vehicles with satisfactory performance, some challenges remain largely unsolved. Many of the shortcomings stem from the fact that in order to accelerate the production of the vehicles, the batteries used were primarily adapted from already existing technologies developed for very different applications, such as mobile devices, with different performance requirements.

One of the key components of the battery is the positive electrode, and more precisely its active material, i.e. the compound that initially stores and can reversibly exchange lithium ions with the negative electrode during battery operation. Some of the compounds that have been used in the Li-ion technology are layered oxides, with general formula $LiMO_2$ (where M = Co, Mn, Ni, Al or combinations of them). The most representative families of layered oxides are $LiNi_xMn_yCo_zO_2$ where x+y+z=1, widely known as NMCs and $LiNi_xCo_yAl_zO_2$ where x+y+z=1, known as NCAs. Other active materials present in commercial batteries are $LiFePO_4$ (LFP), with olivine structure, and the spinel $LiMn_2O_4$ (LMO). All these compounds contain transition metals which are redox active and provide the lithium reservoir in Li-ion batteries, which are assembled in the discharged state. They play thus a crucial role in the battery's capacity, cost and the environmental footprint stemming from the mining and processing of the various metals involved. Each material possesses its own strengths and weaknesses which could be generalized as layered oxides having the highest reversible capacities, $LiFePO_4$ having the longest cycle life and safety and the lowest cost, and LMO possessing very fast reaction kinetics while maintaining low cost.[1], [2] In an effort to tailor materials to the application needs, a blend of multiple active materials is often utilized in EV batteries. Although often used in commercial batteries, blending remains a largely empirical practice, and only a limited number of studies have focused on rationalizing the interactions between different active materials.[3]

The most popular active material blend is that of layered oxides and LMO. When LMO is mixed with NMC it has been observed that, even though the total specific capacity of the electrode decreases, the overall lithium exchange kinetics of the electrode improve. Moreover, such blended electrode can exhibit additional improvements as a result of the "synergy" between components: higher energy density than expected from the rule of mixture, especially at high rates, and also lower capacity fading, the latter being related to a decrease in manganese dissolution.[4], [5] During cycling, the effective rate experienced by a material within a blend can differ significantly from the nominal cell rate [6] and blend components can bear more or less current depending on the cell state of charge and the individual reaction kinetics of the materials.[6]

On the other hand, safety concerns related to EVs mainly revolve around their battery related hazards. Catastrophic failure usually happens when the battery is overheated above a critical threshold, causing a phenomenon known as thermal runaway. During such an event, large amounts of heat are released, triggering a series of exothermic reactions that can result in battery failure, fire, or explosion. These reactions can involve the electrode materials, the electrolyte, or internal short circuits, causing a rapid increase of temperature which further accelerates such reactions, creating a positive feedback loop. The cathode plays a crucial role in this phenomenon and its thermal stability and interaction with other components can significantly influence the risk of thermal runaway.[7], [8] Additionally, many of the active materials release oxygen when heated, which can fuel combustion in the presence of the flammable organic compounds used as electrolyte solvents in Li-ion batteries.[9] Studies on active materials have been carried out to increase this critical runaway temperature and/or reduce the heat released during the event through chemical substitutions, coatings or modifying the electrolyte.[10], [11] Blending multiple active materials together has also been utilized to improve safety in Li-ion batteries [12].

A very promising family of next-generation positive active materials meant for EVs is the so called lithium-rich layered oxides.[9], [13] Their chemical formula and crystal structure derives from that of layered oxides, yet have a Li/M ratio higher than 1 and can therefore

be described as $Li_{1+x}M_{1-x}O_2$ where typically $0 < x \leq 0.33$.[14] Figure 4.1 shows simple layered oxides featuring alternate layers of MO_2 and lithium and lithium rich oxides (LROs) that bear lithium in the transition metal layers.

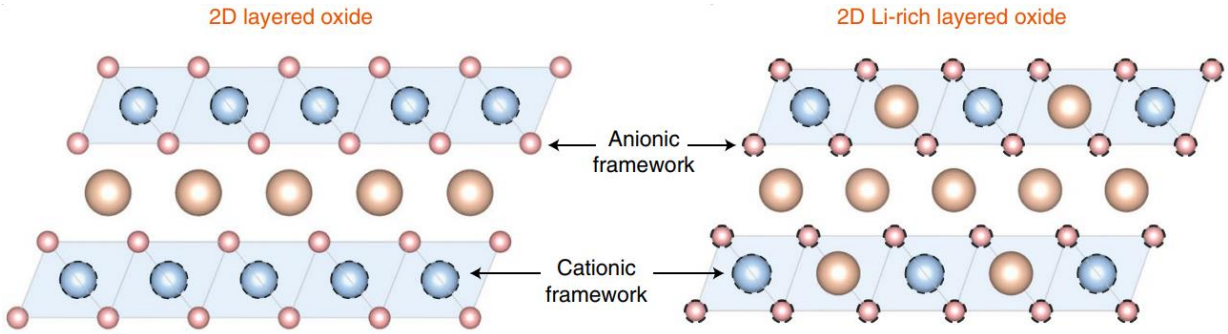

Figure 4.1: Comparison between the structure of a layered oxide such as $LiCoO_2$ (Left) and a Lithium rich layered oxide (Right). Oxygen, Transition metal and Lithium are the red, blue and yellow atoms respectively. [15]

These materials possess very large reversible specific capacities able to exceed 250 mAh/g, which are attributed to the participation of the oxygen in the redox reaction during cycling.[16], [17] However, structural changes often involving oxygen release result in low initial coulombic efficiencies (typically around 80%) and significantly reduce capacity retention over time. Additionally, thermal stability is a concern, as structural instability and oxygen loss, among other factors, also contribute to the lowering of the onset temperature of thermal decomposition.[18], [19] Such materials have been very recently commercialized for use in electric vehicles. [20]

A very unique characteristic of this type of materials is their first oxidation upon battery charge that shows a plateau above 4.5 V, commonly referred to as "activation", which results in a significant irreversible capacity. This results in a lithium inventory loss from the initial charge, which remains trapped in the negative electrode throughout subsequent cycles. Below is an example of such a reaction with an LRO of general formula $Li_{1+z}M_{1-z}O_2$ where z is the amount of lithium excess., In the following equations, y represents the amount of lithium that cannot be incorporated back into the positive electrode material after the first oxidation and x the amount of lithium involved in the

reversible deintercalation/intercalation process. The amount of Li consumed for SEI formation is not considered in the reactions.

1) First charge of LRO // Graphite cell:

$$Li_{1+z}M_{1-z}O_2 + (x+y)\,C_6 \rightarrow xLiC_6 + yLiC_6 + Li_{1+z-x-y}M_{1-z}O_2$$

2) Subsequent charge & discharge of LRO // Graphite cell:

$$xLiC_6 + yLiC_6 + Li_{1+z-x-y}M_{1-z}O_2 \leftrightarrow Li_{1+z-y}M_{1-z}O_2 + xC_6 + yLiC_6$$

A limited number of studies have suggested the possibility of accommodating the excess lithium ions (y) within the positive electrode itself by combining an LRO with a compound that can reversibly host lithium ions in the same electrode. This approach would enable the utilization of all the lithium, reducing the need for excess active material in the negative electrode and thereby enhancing the overall energy density of the battery. This can be done either by simple blending or as a coating. In the seminal work by Lee and Manthiram [21], [22] the LRO $Li[Li_{0.2}Mn_{0.54}Ni_{0.13}Co_{0.13}]O_2$ was combined with V_2O_5, $Li_4Mn_5O_{12}$ or LiV_3O_8 which can act as the lithium acceptor. This allowed them to optimize the first cycle efficiency as lithium could be reinserted to the lithium acceptor after the first charge, thereby reducing the amount of lithium retained in the negative electrode, and therefore the need for excess graphite. It is interesting to note that, with this approach, the amount of lithium inserted in the electrode during the first discharge could exceed the amount extracted through the first charge if the negative electrode can provide this extra lithium e.g. in a half cell vs lithium metal. Another similar strategy developed later has been the modification of an LRO to form surface and bulk domains of γ-MnO_2 (the delithiated form of LMO), [23], [24], [25] or coating with amorphous $FePO_4$. [26] Both strategies were shown to improve the first cycle coulombic efficiency for the positive electrode.

In the present work a simpler related strategy is proposed in which blending involves LRO and a chemically delithiated compound as lithium acceptor, in this case λ-Mn_2O_4 or $FePO_4$. This concept is validated with a lithium rich, manganese rich and cobalt free

layered oxide with formula $Li_{1.125}Ni_{0.312}Mn_{0.563}O_2$ (LRO). Blending with λ-MnO_2 or $FePO_4$ should a priori effectively reduce and even suppress the first cycle irreversible capacity and improve the thermal properties of the positive electrode.

Comparing this approach to the reaction scheme mentioned earlier would yield two scenarios depending if the materials react prior to cell operation (during mixing and electrode fabrication) or not. Considering no reactivity, the reaction with the appropriate amount of $FePO_4$ would be as follows:

1) First charge of (LRO+ $FePO_4$) // Graphite cell.

$$yFePO_4 + Li_{1.125}Ni_{0.312}Mn_{0.563}O_2 + (x+y)C_6 \rightarrow yFePO_4 + Li_{1.125-x-y}Ni_{0.312}Mn_{0.563}O_2 + xLiC_6 + yLiC_6$$

2) Subsequent charge & discharge of (LRO+ $FePO_4$) // Graphite cell.

$$yFePO_4 + Li_{1.125-x-y}Ni_{0.312}Mn_{0.563}O_2 + xLiC_6 + yLiC_6 \leftrightarrow yLiFePO_4 + Li_{1.125-y}Ni_{0.312}Mn_{0.563}O_2 + (x+y)C_6$$

In this case, no graphite remains lithiated after discharge and the entirety of lithium is able to be accomodated back in the positive electrode, so that the reversible capacity of the cell is higher.

Conversely, if materials react during electrode fabrication or cell assembly, a direct reaction would take place:

$$yFePO_4 + Li_{1.125-z}Ni_{0.312}Mn_{0.563}O_2 \rightarrow (y-z)FePO_4 + zLiFePO_4 + Li_{1.125-z}Ni_{0.312}Mn_{0.563}O_2$$

the amount z will be determined by the compositions at which the electrode is at equilibrium.

4.2 Experimental Details

4.2.1 Blend Preparation

To prepare the blends under study, λ-MnO_2 was synthesized from commercial $LiMn_2O_4$ which was chemically delithiated as described by Hunter J.[27] in acidic aqueous medium according to the reaction:

$$H^+ + LiMn_2O_4 \rightarrow Li^+ + 1.5\ \lambda\text{-}MnO_2 + 0.5\ Mn^{2+} + OH^-$$

To carry out the reaction, around 200ml of 0.1M HCl solution was prepared, 5g of $LiMn_2O_4$ was added to the solution and the suspension stirred for 48h at room temperature. Immediately after mixing, the colour of the suspension turned from dark blue/black to dark red. The dark red powder was then centrifuged, washed and dried at 70ºC overnight. This reaction was carried out using LMOs with two different average particle sizes, one with <500nm diameter (Sigma-Aldrich) and one with D_{50} = 12-18µm (MTI corp.).

To obtain $FePO_4$, commercial carbon-coated $LiFePO_4$ (ALEEES) was chemically delithiated according to the protocol described in [28] which involves the following reaction:

$$2LiFePO_4 + Na_2S_2O_8\ (aq.) \rightarrow 2FePO_4 + Na_2SO_4\ (aq.) + Li_2SO_4\ (aq.)$$

For the reaction, a large excess of $Na_2S_2O_8$ was utilized. 15.09g of $Na_2S_2O_8$ (63.4 mmol) was dissolved in 127ml deionized water to yield a 0.5M solution and then 5g (31.7 mmol) of $LiFePO_4$ powder was added while stirring at room temperature. The suspension was left stirring overnight and afterwards the product was washed with deionized water to remove excess $Na_2S_2O_8$ and Li_2SO_4, then filtered and finally dried at 70ºC overnight. This yielded a light grey powder which was stored and dried at 120°C under vacuum prior to each use. Micrometer sized LRO (UMICORE) was used as received and always kept stored in argon filled glovebox.

4.2.2 Electrode Fabrication

For electrode preparation, Polyvinylidene fluoride (PVDF) binder (dried at 70ºC) was dissolved in N-Methyl-2-pyrrolidone (NMP) to obtain a concentration of 5% wt. Dry powders of active materials and carbon additive (C65, also previously dried at 70ºC) were mixed in the appropriate quantities to yield a slurry with 1g of total solid content to achieve an electrode formulation of 84:8:8 (Active material : Binder : Carbon

Additive). The content of $FePO_4$ or λ-MnO_2 in the blended electrode with LRO ranged from 0 to 50%. The slurry was stirred using a disperser (IKA UltraTurrax T25) and a small amount of pure NMP (approx. 1/3 of the binder solution mass) was added to adjust the viscosity while stirring to make electrode fabrication easier.

The slurry was tape casted on 18μm aluminium foil using a blade with 250μm gap. The casted electrodes were then dried under vacuum at 70ºC overnight. Disks of appropriate diameter (in this case 14mm) were then punched and further dried at 120ºC under vacuum for at least 2h using a Büchi glass oven, before introducing in an Argon filled glovebox, without any prior exposure to air.

4.2.3 Electrochemical performance

To assess the electrochemical performance of the prepared electrodes, CR2032 coin cells were assembled using lithium metal as counter electrode and a Whatman glass fiber filter as a separator, soaked in a dissolution of 1M $LiPF_6$ in 1:1 EC:DMC (Sigma-Aldrich) as electrolyte. The electrochemical tests were performed using an MPG2 potentiostat-galvanostat (Bio-logic). For each cell, the first cycle was performed at C/30 with high voltage cutoffs of 4.7V or some cases 4.8 V to activate LRO and assess its efficiency. The lower cutoff voltage was 2 V for blends with $FePO_4$ and 3.2 V for blends with λ-MnO_2. In the blends with $LiFePO_4$ and LMO, and to maintain comparability, the cutoff voltages were 4.5 - 3.2 V.

4.2.4 Thermal Stability Measurements

The thermal stability of the electrodes in contact with the electrolyte was assessed by Differential Scanning Calorimetry (DSC). In order to more easily recover the electrodes after electrochemical testing, Swagelok cells were used with 13mm diameter working electrodes dried under vacuum at 120ºC, lithium metal counter electrodes and Whatmann glass fiber separators soaked in 1M $LiPF_6$ in 1:1 EC:DMC (Sigma-Aldrich) as electrolyte. After charging at C/10 up to 4.8V for activating the lithium rich compound,

they were discharged down to 4.6V, and kept at that potential until the cell was disassembled (typically less than 6h). inside the glovebox. The positive electrodes were recovered and washed using fresh Dimethycarbonate (DMC) and scratched to separate the coating from the aluminium current collector. Around 4-5mg of the retrieved powder and 3-4mg of fresh electrolyte were placed inside a stainless steel high-pressure sample holder. The samples were then heated up to 300ºC at 10ºC/min rate under nitrogen flow using a DSC 204F1 Netzsch calorimeter.

4.2.5 X-ray diffraction

In house X-ray diffraction measurements were recorded on a Bruker D8 Advance A25 X-ray diffractometer in a 2-theta range of 3 ^{0} to 35 ^{0} using Molybdenum Ka radiation (λ = 0.7093Å) and a scan speed of 0.02 degrees per 5 seconds. The incident beam optic setup comprises a Johansson monochromator, 6 mm divergence slit (DS) and 2.5 degree vertical Soller slit. The diffracted beam optic setup includes 2.5 degree vertical Soller slit. The detector used is a LYNXEYE XE-T (1D mode) with a 4.075 degrees PSD opening.

The operando XRD measurements were carried out on BL-04 (MSPD) beamline of ALBA synchrotron (proposal number 2024028311) using 30 keV photon energy (λ=0.4138 Å) in transmission geometry using a MYTHEN2 high-throughput position sensitive detector for the 2θ range 1° to 60°. The cells used were specially adapted Hohsen CR2032 coin cells (Institute for Applied Materials - Energy Storage Systems Karlsruhe Institute of Technology), bearing a thin (130µm) glass window on both sides and a hole on the stainless steel spacer. Beneath the metallic lithium used as a negative electrode, a Kapton disk was used to support the soft metal from entering the spacer hole, and as such improve the cell pressure. A VSP potentiostat-galvanostat (Bio-Logic, France) was utilized for the electrochemical testing. The cells went through a C/30 initial charging up to 4.8 V followed by a C/10 discharge down to 2 V while acquiring their diffraction patterns. For the measurement, the cells were mounted on an 8 coin cell carousel-like

holder enabling sequential data acquisition [29]. The whole setup allowed the acquisition of one pattern per approximately 10 minutes. Patterns were processed and refined when required using FullProf software in conjunction with FullProfApp.[30], [31]

4.3 Results and Discussion

The delithiated active materials were analyzed by X-ray diffraction prior to their utilization in order to verify the success of the reaction as well as the existence of impurities. Le Bail refinement of its diffraction pattern shown in Figure 4.2 shows a good match with the expected pattern of $FePO_4$ and λ-MnO_2, with no additional peaks being observed in the patterns. Furthermore, Figure 4.3 shows the XRD pattern of the pure LRO.

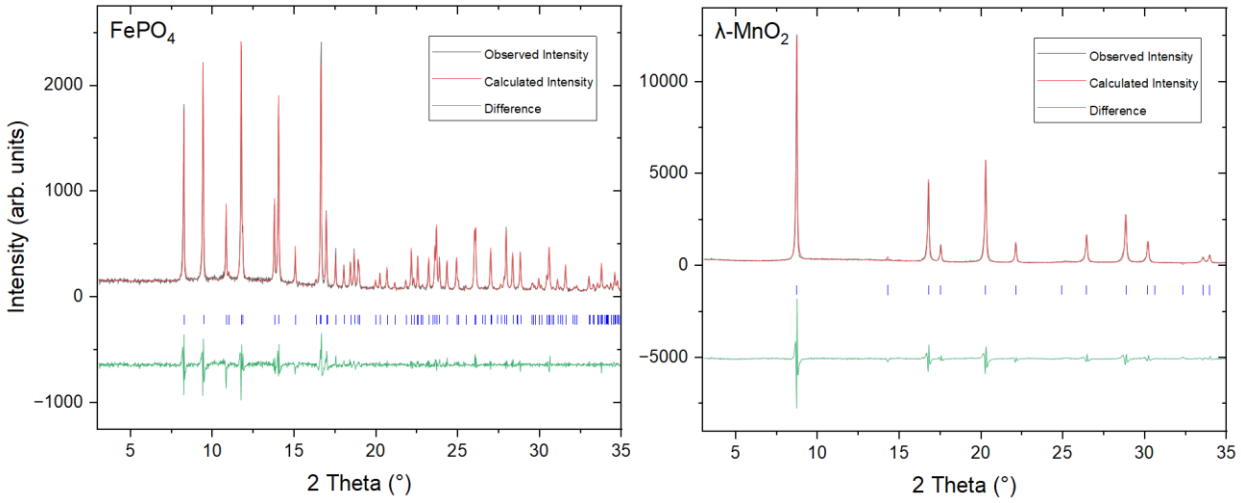

Figure 4.2: X-ray diffraction patterns and Le Bail refinement corresponding to as prepared $FePO_4$ (left) and λ-MnO_2 (right) . (λ =0.7093 Å).

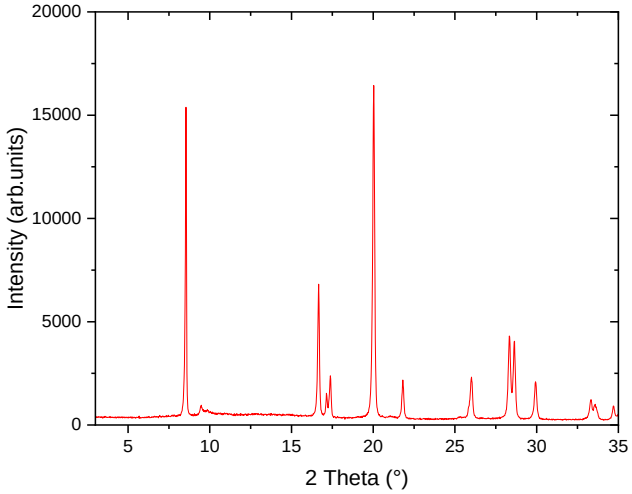

Figure 4.3: X-ray diffraction pattern of the LRO used. (λ =0.7093 Å)

4.3.1 Study of LRO and λ-MnO_2 blended electrodes

Figure 4.4 depicts the first cycle voltage vs. capacity profiles for coin cells assembled with working electrodes containing a mixture of LRO and different amounts of nanosized λ-MnO_2. They all exhibit reversible specific capacities approximately in the range of 90-120 mAh/g which is significantly lower than what was expected. (see Table 4.1) Furthermore, the high voltage "activation" plateau of LRO expected during the first charge is not clearly visible in any of the blends, the expected increase of the initial cycle coulombic efficiency is not evidenced and no clear patterns are observed.

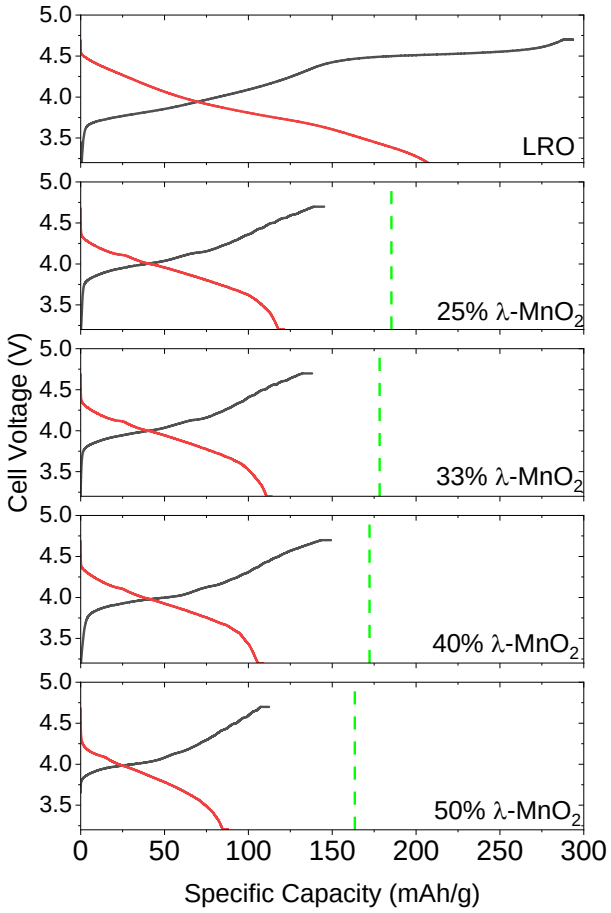

Figure 4.4: Voltage vs Capacity plots of the first cycle of cells with positive electrodes consisting of blends of LRO with nanosized λ-MnO_2. Oxidation is depicted in black and reduction in red. Green lines show the expected capacity of each blend calculated considering the relative amounts of the components.

Table 4.1: Capacity values for LRO : λ-MnO_2 blends, deduced from curves depicted in Figure 4.4. The expected specific capacities are calculated considering the capacities obtained for the pure LRO and LMO.

Composition	***1st charge specific capacity***	***1st discharge specific capacity***	***Initial cycle coulombic efficiency***	***Expected specific capacity***
LRO	*294 mAh/g*	*207 mAh/g*	*70%*	-
25% λ-MnO2	*145 mAh/g*	*121 mAh/g*	*83 %*	*185 mAh/g*
33% λ-MnO2	*138 mAh/g*	*114 mAh/g*	*83 %*	*178 mAh/g*
40% λ-MnO2	*149 mAh/g*	*109 mAh/g*	*73 %*	*172 mAh/g*
50% λ-MnO2	*111 mAh/g*	*88 mAh/g*	*79 %*	*163 mAh/g*

This unexpected behavior led us to speculate about the possibility of direct reaction beween λ-MnO_2 and LRO, which may be favored by its oxidizing character. Moreover, oxidation of LRO would enhance its sensitivity to humidity and result in its degradation during the electrode preparation process, which could be the explanation for the low reversible capacity and efficiency. To test this hypothesis, a new tape-casted laminate was made in the argon filed glovebox with micron size λ-MnO_2, in an attempt to limit its reactivity decreasing the contact area between the two active materials.

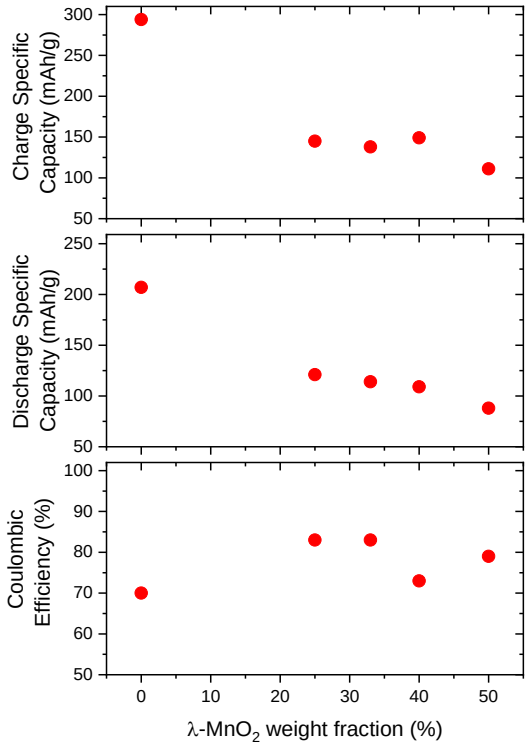

Figure 4.5: Charge (top) and discharge (middle) specific capacities as well as coulombic efficiency (bottom) as a function of nanometric λ-MnO_2 for the blends of it with LRO.

As prepared electrodes (both in air and in argon) were scratched and the powders sealed in capillaries. Synchrotron XRD patterns are depicted in Figure 4.6 focusing on two representative Q-ranges that include peaks corresponding to both λ-MnO_2 and LRO (the latter marked with an asterisk), together with the patterns corresponding to pristine λ-MnO_2 powders used to prepare blended electrodes. The patterns of the two pure λ-MnO_2 powders are very similar. It is evident that the peaks corresponding to nanometric sized λ-MnO_2, appear at lower angles for the blended electrode. This translates to larger cell volume, which is indicative of a higher degree of lithiation, and confirms that lithium has transferred from LRO to λ-MnO_2 during electrode fabrication in air, or storage.

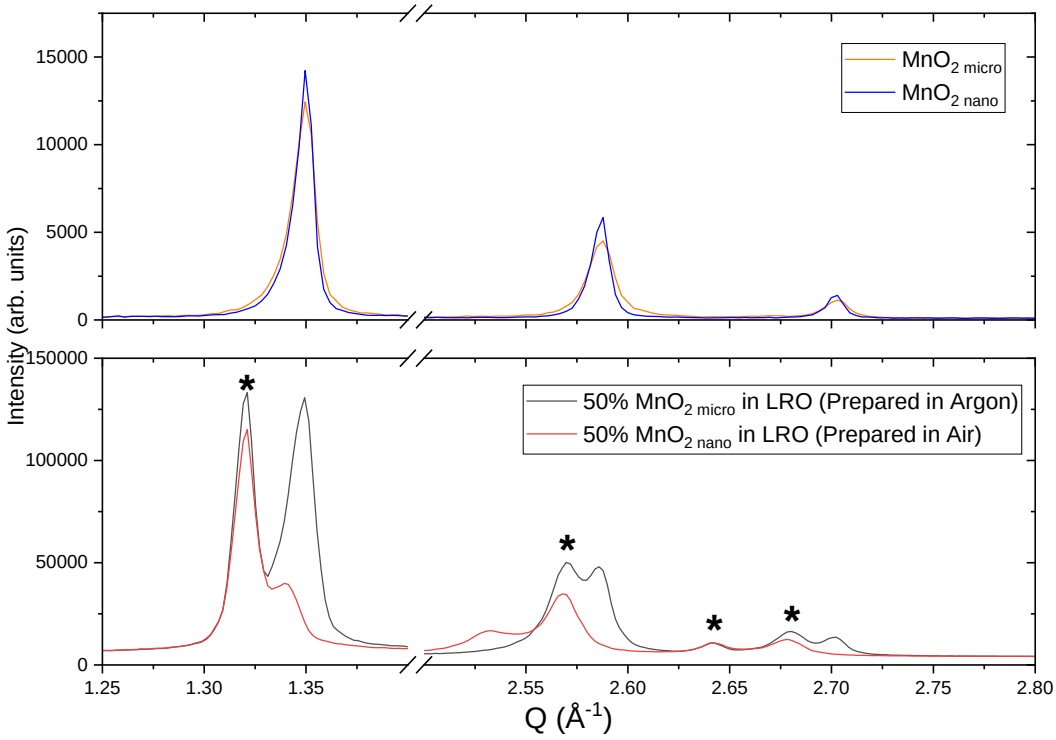

Figure 4.6: (Top) Comparison of diffraction patterns obtained for nanometric MnO_2 (blue line) and micrometric MnO_2 (orange line) pristine powders. Patterns were collected using Mo Ka radiation (Bottom). Comparison of electrodes bearing 50%wt. MnO_2 in LRO, one prepared with micrometric MnO_2 under Argon (black line) and the other with nanometric MnO_2 in air (Red line). Patterns were collected at ALBA synchrotron using 38keV photon energy (λ=0.3268Å).

Figure 4.7 shows the comparison between the voltage vs capacity profiles of two blended electrodes with 50% λ-MnO_2 content, one prepared in open air with nanosized λ-MnO_2 and the other in the glovebox with micron sized λ-MnO_2. In agreement with lower reactivity between the blend components during the electrode preparation, capacity values are larger for the latter (142mAh/h vs. 88mAh/g), which is consistent with the observation of the high voltage plateau corresponding to LRO. Furthermore, the coulombic efficiency reached 98% instead of the previous 79%. When this is compared to pure LRO's coulombic efficiency of 70% the positive impact of blending LRO with a lithium acceptor such as λ-MnO_2 becomes clear. When compared to the

expected theoretical capacity, with this approach the blend achieves 87% of the expected, significant improvement over the 54% achieved previously.

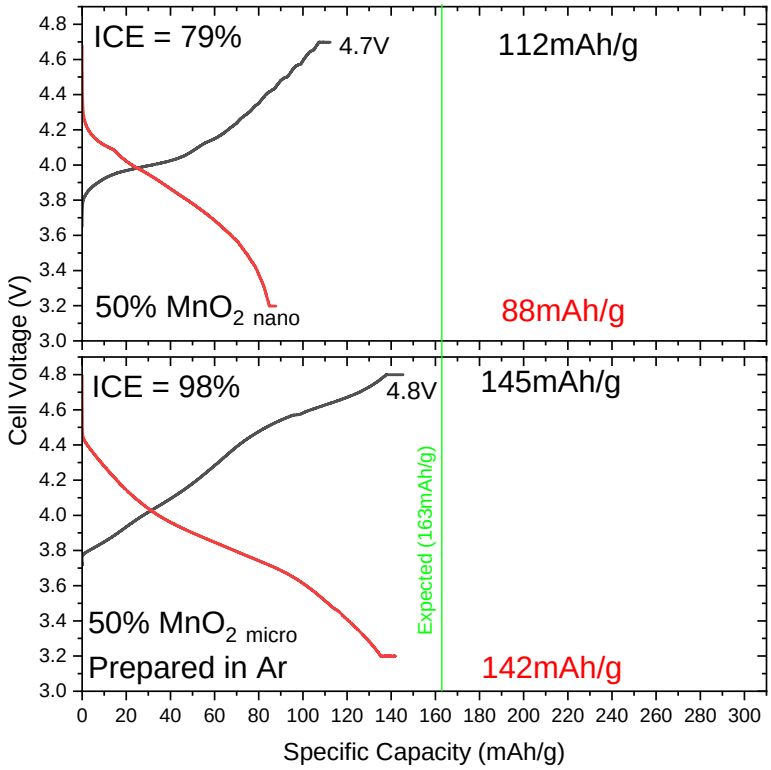

Figure 4.7: Voltage vs capacity curves for the 2 blends prepared by adding 50%wt λ-MnO2 in LRO. Top bears sub micrometer sized λ-MnO2 and was prepared in air while the bottom was prepared using micrometric λ-MnO2 particle in an argon filled glovebox. Oxidation is depicted in black and reduction in red. Green lines show the expected capacity of the blend.

4.3.2 Study of LRO and $FePO_4$ blended electrodes

With the aim of fabricating blends with a less oxidizing delithiated material so that reactivity during the preparation process could be diminished, electrodes containing LRO blended with $FePO_4$ were studied.

In order to assess lithium exchange between the blend components during and after casting, as well as when the final electrode is exposed to electrolyte, XRD patterns were taken on the dry laminates before and after being immersed in electrolyte for 1 week

(see Figure 4.8). The patterns show no appreciable differences and no $LiFePO_4$ peaks were present in any of the two cases, which enables us to conclude that in this system there is no reaction between the electrode blend components prior to battery operation.

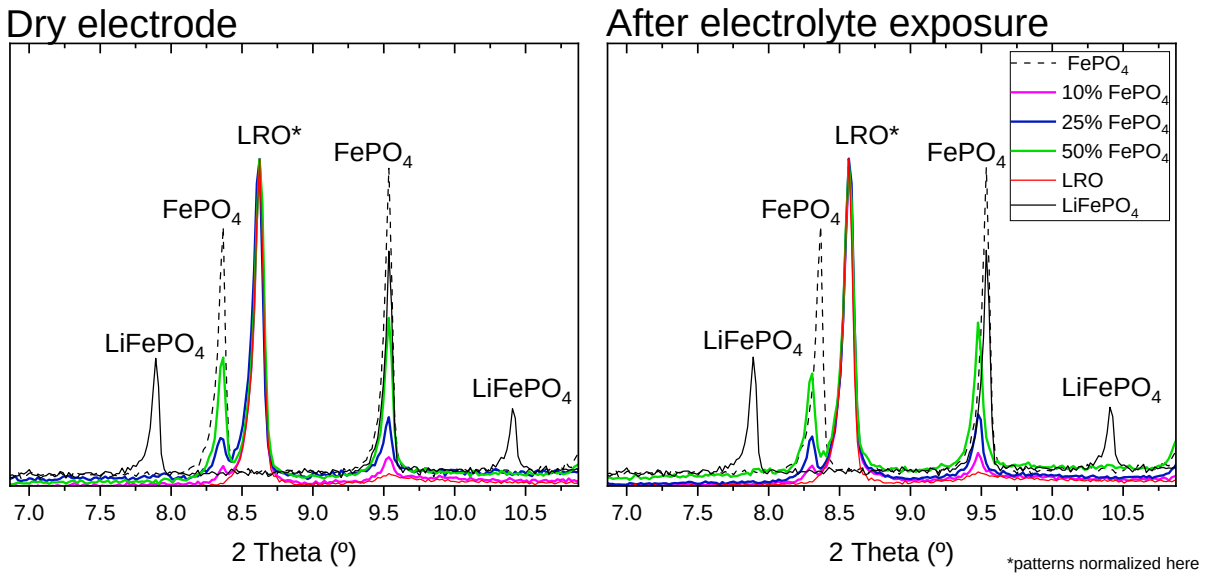

Figure 4.8: X-Ray diffraction patterns of electrode as prepared (left) and after 1 week in electrolyte (right).

Figure 4.9 depicts the voltage vs. capacity profile for the first cycle recorded for all cells containing LRO:$FePO_4$ blends as positive electrodes together with capacity and coulombic efficiency values. In all electrodes, upon the first oxidation, the high voltage plateau of LRO is witnessed around 4.6V with its capacity getting smaller as the LRO fraction in the blend decreases. Another feature present in all blends is a small plateau in the beginning of oxidation, around 3.5V, which is the characteristic voltage for the $LiFePO_4$ to $FePO_4$ phase transition, which is clearly indicative of the existence of $LiFePO_4$ in the "as assembled" cell. There is no clear trend observed in the magnitude of this plateau as a function of blend composition as seen in Figure 4.9. Since no reaction between the blend components prior to cycling was detected by XRD (see Figure 4.8) one can conclude that either there was indeed some reactivity but the amount of $LiFePO_4$ formed was too small to be detected by XRD or the presence of $LiFePO_4$ in the

electrodes is due to micro-shorts suffered by the cell during the assembling/handling process prior to testing. Upon reduction, all cells exhibit a very similar voltage vs. capacity profile starting with a sloping region and turning into a flat plateau around 3.5V, with the plateau becoming longer and the sloping region shorter as the amount of $FePO_4$ in the blend increases.

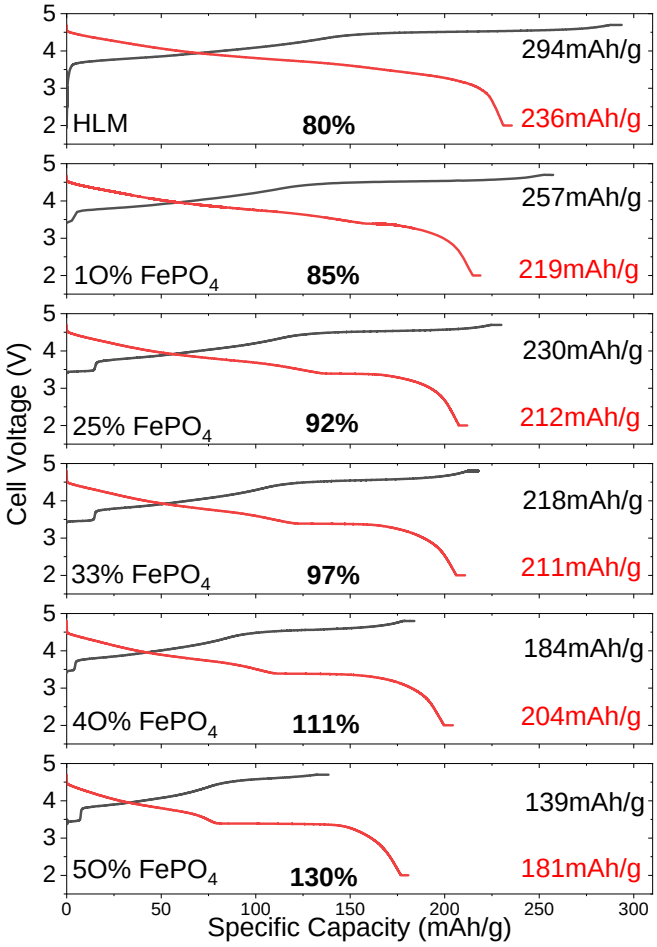

Figure 4.9: Voltage vs capacity curves for the blends of LRO with $FePO_4$ with different compositions showing the increase in the first cycle efficiency. First charge (black) and discharge (red) specific capacity values are also included as well as the first cycle coulombic efficiency (Bold).

The decrease in capacity upon the first oxidation with increasing amount of $FePO_4$ can be rationalized as due to its intrinsic composition (see Table 4.2 for expected specific capacity values). Along the same trend, the capacity upon reduction also decreases, it

remains though relatively close to the expected, as seen in Table 4.2. Yet, and in spite of this expected trend in the electrode capacity, the coulombic efficiency is drastically improved by blending, with the sample containing 33% $FePO_4$ being the closest to 100% (Figure 4.10 and Table 4.2). It is to be noted that the coulombic efficiency values exceeding 100% are related to the fact that cells were assembled with lithium metal counter electrodes, so that the lithium reservoir is extremely large, and in full cells using graphite counter electrodes values would never exceed 100%. Thus, the optimal composition application-wise would be 33% $FePO_4$, as the coulombic efficiency already approaches 100% and the theoretical capacities are higher than for higher contents of $FePO_4$.

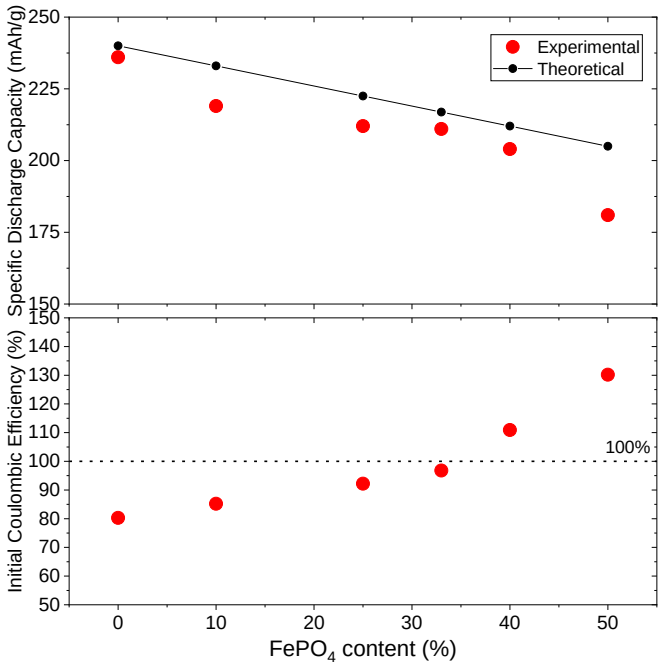

Figure 4.10: Experimentally measured and theoretical specific capacities (top) of the electrodes studied (top) and 1st cycle coulombic efficiencies (bottom) of the studied electrodes. The black points and line show the theoretical capacity of the blends.

Table 4.2: Electrochemical Performance values of LRO with $FePO_4$ blends.

Composition	**1st charge specific capacity**	**1st discharge specific capacity**	**Initial cycle coulombic efficiency**	**Expected specific capacity**
LRO	*294 mAh/g*	*236 mAh/g*	*80.3%*	-
10% $FePO_4$	*257 mAh/g*	*219 mAh/g*	*85.2%*	*233 mAh/g*
25% $FePO_4$	*230 mAh/g*	*212 mAh/g*	*92.2%*	*222 mAh/g*
33% $FePO_4$	*218 mAh/g*	*211 mAh/g*	*97.8%*	*217 mAh/g*
40% $FePO_4$	*184 mAh/g*	*204 mAh/g*	*110.9%*	*212 mAh/g*
50% $FePO_4$	*139 mAh/g*	*181 mAh/g*	*130.2%*	*205 mAh/g*

4.3.3 The impact of blending LRO with $FePO_4$ in the thermal stability of the electrode

To test the effect of blending in the thermal stability, oxidized electrodes containing only LRO and LRO with 50% $FePO_4$ were evaluated by DSC (see experimental section). Figure 4.11 shows the heat flow samples as a function of temperature for both electrodes, which exhibit a large exothermic peak in the 220-250ºC which is tentatively assigned to reactions involving the electrolyte and released O_2 in the electrode.[32], [33] The solid vertical lines show the temperature where heat flow peaks. The positive impact of blending is observed as the blended electrode exhibits the most intense peak almost 20ºC higher than pure LRO (244.9 ºC compared to 226.8ºC).

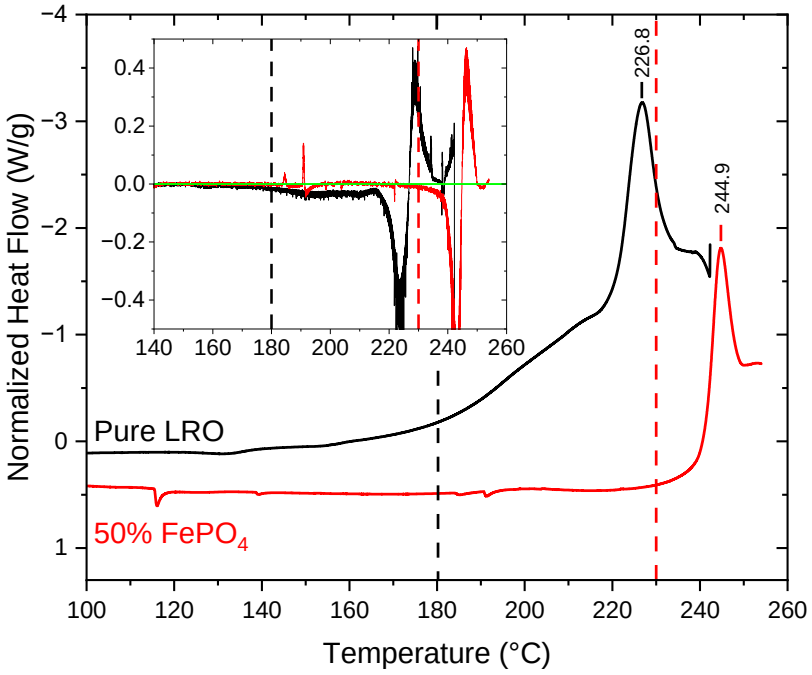

Figure 4.11: DSC traces of pure LRO (black line) and 50% LRO – $FePO_4$ blend (red line) showing the different reaction temperature. Vertical lines show approximately the onset of the exothermic event. Heating rate was 10 °C/min. The inset figure shows the 1st derivative of heat flow as a function of temperature. The green line marks the zero value of the derivative.

Aside the temperature, the shape of the peaks also differs significantly. In the case of the pure LRO, a second exothermic process seems to take place at lower temperature appearing as a shoulder peak which is not evident for the blend. Such double peak profile has been witnessed before in similar systems[34]. The first peak is related to the active material decomposition while the second to the decomposition of the binder and the reduction of the active material by carbon black. This leads to a very significant difference in the onset temperature between the two samples as shown roughly by the two dashed lines placed at 180°C and 230°C respectively (values determined from derivative curves). These lines represent the point where exothermic side reactions are initiating and heat generation causes the battery to enter a positive feedback loop (i.e. rising temperatures lead to increased rates of exothermic reactions creating a cycle that

accelerates thermal degradation). The difference of 50°C between the two samples is substantial, which coupled to the seemingly lower amount of heat released, makes the blended electrode considerably less prone to thermal runaway.

4.3.4 Operando synchrotron X-ray diffraction(XRD) studies of blended electrodes containing LRO and $FePO_4$.

In order to gain further insight into the electrode dynamics in LRO:$FePO_4$ blends, operando synchrotron X-ray diffraction was conducted to compare the behavior of 33% and 50% $FePO_4$ containing blends to that of pure LRO.

Electrodes containing only LRO as active material

The evolution of the XRD patterns of LRO upon the first oxidation at C/30 up to 4.8V is depicted in Figure 4.12, in an angular region covering four representative diffraction peaks for this compound. The first diffraction peak close to 5° corresponds to the (003) reflection which, in the case of the layered (R-3m) NMC-type materials, directly probes the interlayer distance between the MO_2 slabs (where M denotes transition metal). As shown in previous works, the interlayer distance during lithium extraction in Li_xMO_2 (NMC-type layered oxides) is the result of competing O−O coulombic repulsions and van der Waals attractions between adjacent layers. Therefore, an increase of the interlayer distance is observed during the first part of the reaction (up to $Li_{0.4}MO_2$ approximately) due to the depletion of screening Li^+ layers, which is followed by an abrupt decrease upon deeper charging resulting from the fact that Van der Waals forces become preponderant. Also, the lack of alkali ions in the interlayer space leads to structural degradation with migration of transition metal ions to neighbouring tetrahedral or oxygen evolution. In lithium rich oxides (LRO), the evolution of the interlayer distance is softer thanks to coulombic attractive forces between remaining Li^+ ions and vacancies from adjacent layers.[35] After charging to 4.8 V a shoulder peak has been observed to appear at the right of the (0 0 3) peak, suggesting the growth of a new phase with an increased M/O ratio (i.e. densified) as a result of O_2 release and Mn

migration to vacant octahedral sites.[36], [37] Such cation migration reduces the number of available sites for lithium, which explains capacity losses over subsequent cycles. Additionally, clusters of vacancies and the formation of molecular oxygen occur in the core of the material. This oxygen, unable to escape the structure, is partially and reversibly reduced during the next discharge.[38], [39] However, there is still debate regarding the exact nature of the species formed from the oxidation of O^{2-} anions, and a peroxo-type dimer $(O_2)^{2-}$, or a superoxo-type electron-hole pair $(O_2)^{-}$ have been proposed.[40], [41], [42]

Our results are in agreement with previous observations as the (003) peak shifts initially towards lower angles and then reverse direction in the last part of the oxidation, when the activation plateau of LRO is reached and a shoulder appears towards higher angles.

The (101) and (012) peaks can be seen monotonically shifting towards higher angles until the end of oxidation. The position of these peaks is also affected by the a and b cell parameters (which in this case are equal) which appear to decrease as lithium is extracted from the compound. A sequential LeBail refinement was performed on the patterns in order to quantify and highlight the dependence of cell parameters. The obtained results are shown in Figure 4.13.

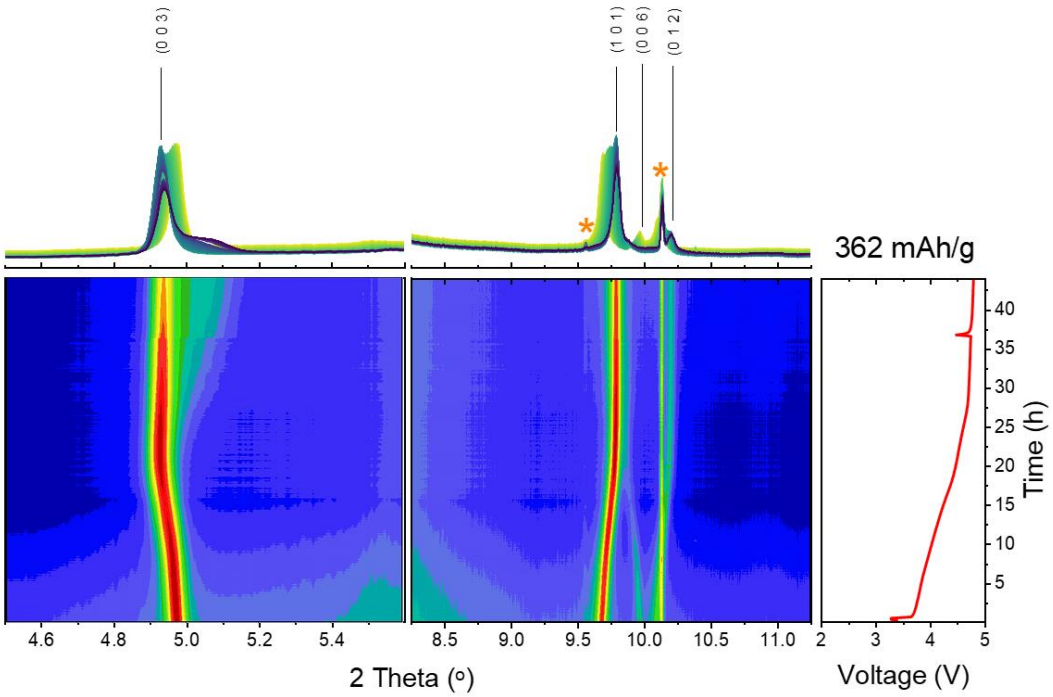

Figure 4.22: Evolution of diffraction patterns at selected angular ranges during the first oxidation up to 4.8V at C/30 for the cell containing an electrode with pure LRO as active material (left) and corresponding evolution of potential (right).

Initially, the cell parameters were 2.86453(7) Å and 14.2629(6) Å for a,b and c respectively. A monotonic decrease of a and b is observed, reaching a minimum of approximately 2.837 Å at 4.7 V and then very slightly increasing thereafter, up to roughly 2.839 Å at the end of charge. For the c parameter, an initial, almost linear, increase is observed until roughly 4.55 V, where a maximum is achieved, close to 14.396 Å. At higher voltages, a fast contraction in the c direction is observed, reaching a minimum of about 14.346 Å. This evolution, as well as the extent of change observed, aligns nicely with published data of similar systems studied with neutron diffraction. [43]

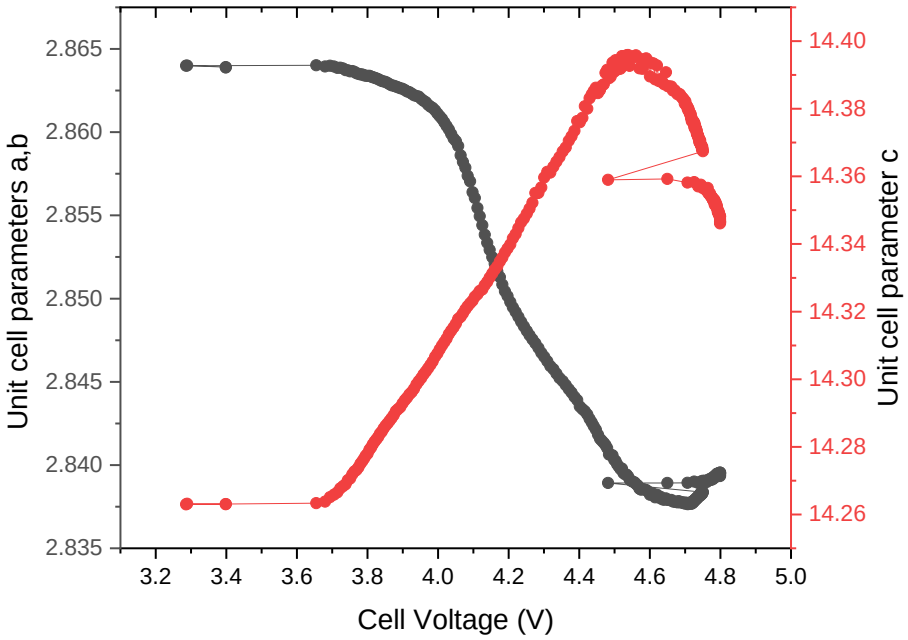

Figure 4.33: Evolution of cell parameters as a function of voltage for the first oxidation of LRO at a rate of C/30.

Following the first oxidation, the cell was discharged at C/10 until 2 V and the evolution of the diffraction patterns throughout the first reduction is depicted in Figure 4.14. The evolution in the position of the peaks throughout the process is minor when compared to oxidation (see corresponding plots in Figures 4.12 and 4.13), and no major changes in the intensity are detected either. This is a surprising result, as the capacity upon this first reduction is 198 mAh/g which corresponds to 0.66 mol of lithium per formula unit.

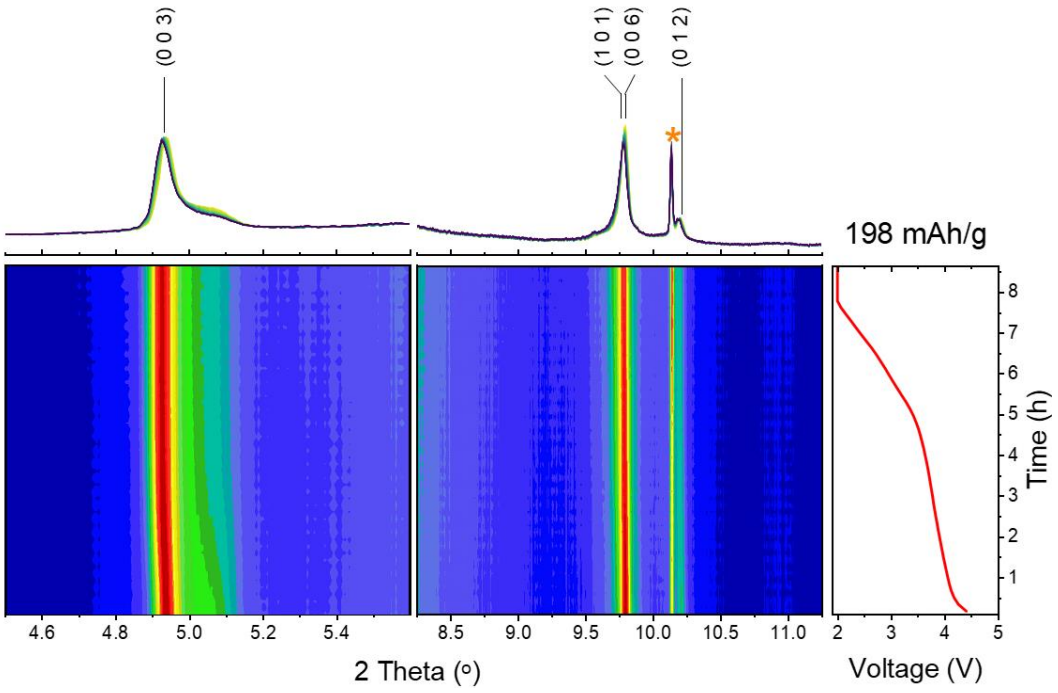

Figure 4.4: Evolution of diffraction patterns at selected angular ranges during the first reduction down to 2 V at C/10 for the LRO cell (left). Voltage evolution during the reduction (right). The peak marked with an asterisk is due to the aluminium current collector.

Interestingly, all four peaks (003), (101), (006) and (012) shift slightly towards lower angles, as happened during the last part of the oxidation, which indicates that the c lattice parameter remains somewhat contracted, and even slightly increases in agreement with the irreversible structural change occurring upon oxidation. The (012) peak shifts also to lower angles, which is the opposite trend to the one observed at the end of oxidation, indicating that the a lattice parameter gradually increases as lithium is reinserted into the material due to reduction of transition metals. Changes in the intensity of the peaks upon reduction are only minor. The most significant change is observed in the shoulder peak next to the (003) reflection, whose area appears to reduce. This could be indicative of the reduction of oxygen trapped in the crystal, as discussed earlier. While it has been proved that the absence of evolution in the diffraction peaks can be related to the inhibition of the electrochemical reaction in the area directly irradiated by the beam [44], [45]. This is unlikely to be the case here, as a clear evolution was observed during oxidation.

Electrodes containing 50% and 33% $FePO_4$ in LRO

Figure 4.15 shows the evolution of the diffraction patterns of the blended electrodes during the first oxidation in the same angular ranges discussed above. As expected, the patterns show peaks corresponding to $FePO_4$ but also some low intensity ones of $LiFePO_4$ too. This is in agreement with the electrochemical results in coin cell (see Figure 4.9) where a small plateau assigned to the oxidation of $LiFePO_4$ appears in the beginning first charge. It should be noted that in this case, since synchrotron radiation is used, phases in very small weight fractions can be seen. Upon oxidation, the position of (003) and (006) peaks of LRO shift to lower angles, changing direction towards the end of charge. On the other hand, the (101) and (012) peaks monotonically shift towards higher angles as in the case of the electrode containing only LRO. Strikingly, no shoulders appear at the end of the first oxidation for the blended electrode, which clearly deserves further investigation. On the other hand, no changes are expected for peaks corresponding to $FePO_4$, as it cannot be further oxidized. However, reflections corresponding to $LiFePO_4$ are expected to disappear in the very beginning of charge, as indeed is observed.

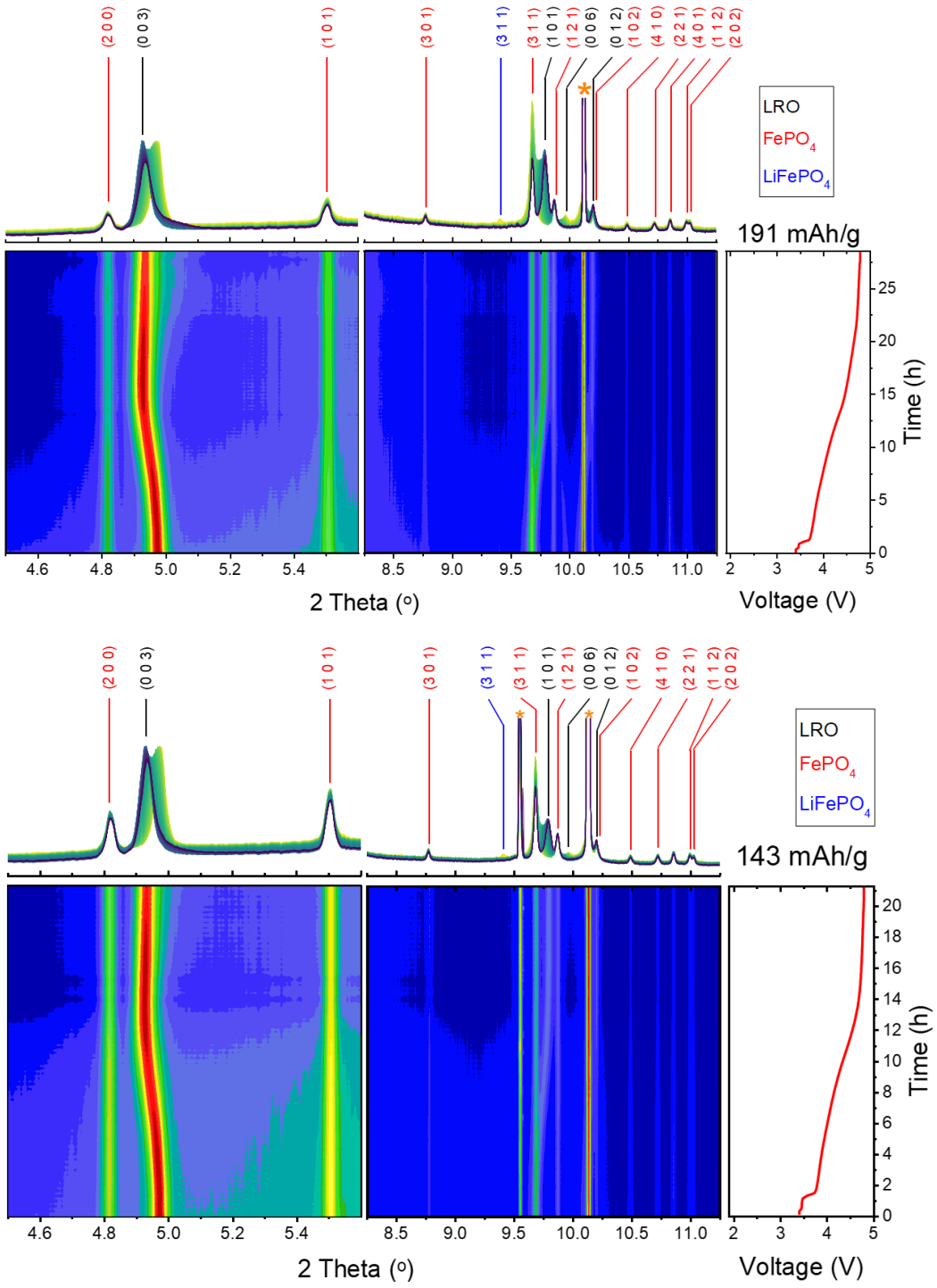

Figure 4.55: Evolution of diffraction patterns at selected angular ranges during the first oxidation up to 4.8V at C/30 rate for the 33% $FePO_4$ (top) and 50% $FePO_4$ (bottom) blend (left). Voltage evolution during oxidation (right). Asterisks mark peaks related to the cell setup and not the materials.

Figure 4.16 shows the overlap of the final patterns of the first oxidation taken for the 3 samples highlighting the area around the (003) peak of LRO. It becomes clear that the size of the shoulder peak differs between the three, appearing to reduce when the $FePO_4$ fraction is increased. This suggests that the existence of $FePO_4$ could potentially influence the generation of the densified phase at high potentials yet would require further research to understand the mechanism of this interaction.

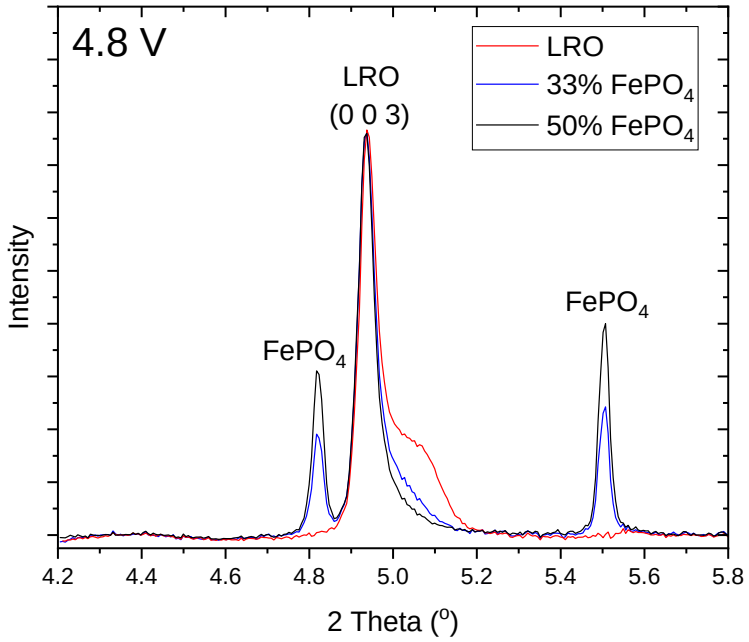

Figure 4.66: Comparison of the diffraction pattern in the angular range around the (003) peak of LRO after the end of oxidation at C/30 and 1h of constant voltage at 4.8V for electrodes containing only LRO or blends with different fractions of $FePO_4$.

During the subsequent reduction of the cells bearing blended electrodes, significant shifts were observed in the position of the peaks corresponding to LRO, which differs from what was observed for the electrode pure LRO electrode. The (003) peak shifts towards lower angles, as also witnessed in the pure compound. However, at approximately 3.7 V, it changes direction towards higher angles. This shift indicates an initial elongation of the interlayer distance followed by a reduction. As for the (101)

peak, it appears to monotonically move towards lower angles for both samples, indicating an overall expansion of the a,b dimensions of the unit cell. The large overlap of the LRO (0 1 2) peak with the (1 0 2) peak of $FePO_4$ combined with their proximity to the large aluminium peak, prevents a definitive analysis of the intensity, however it appears to decrease. When compared to the cell of pure LRO, the mechanism of lithiation of LRO in the blends seems to resemble more closely its delithiation process.

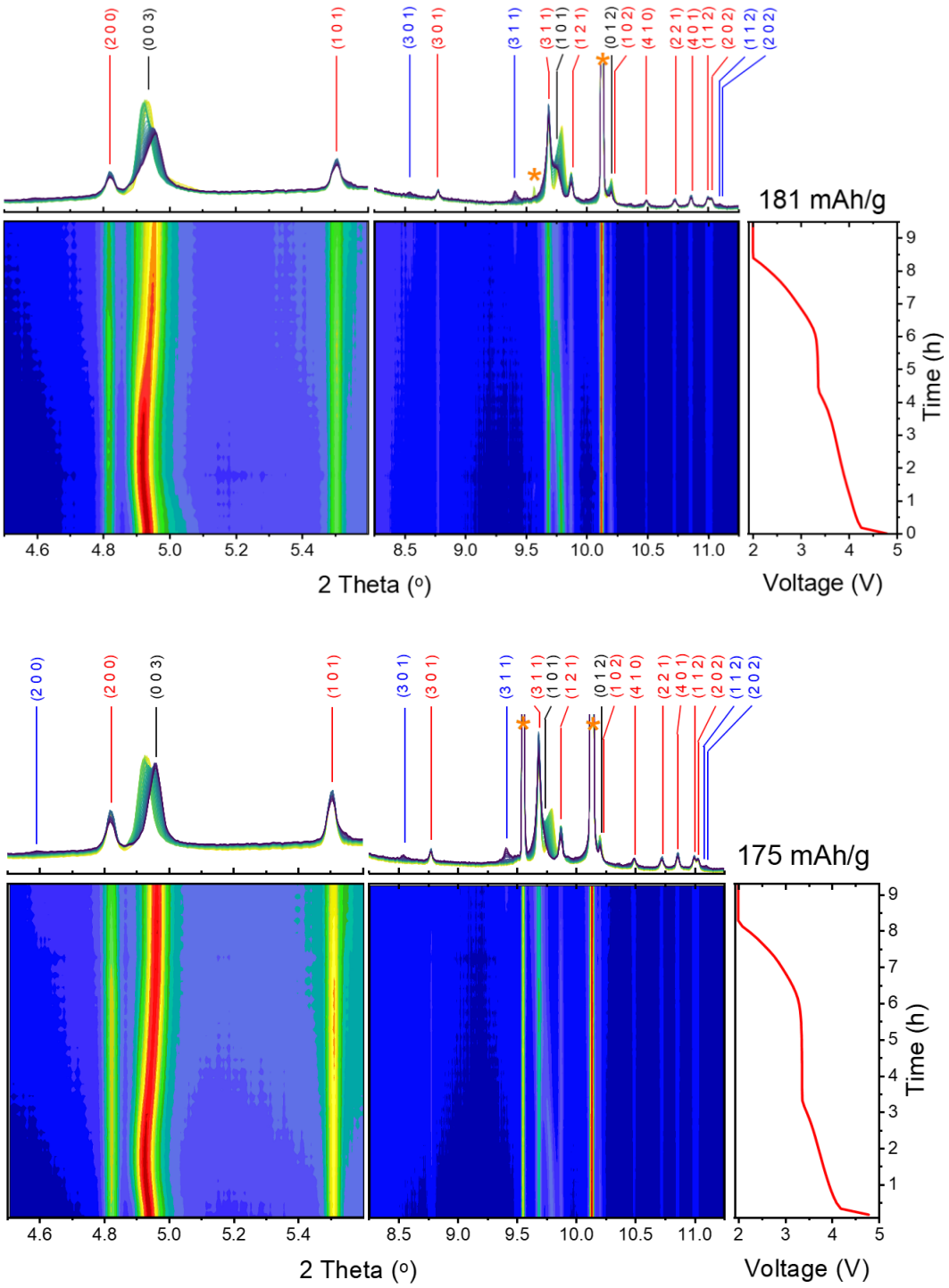

Figure 4.77: Evolution of diffraction patterns at selected angular ranges during the first reduction down to 2V at C/10 rate for the samples bearing blended electrodes, 33% $FePO_4$ (top) 50% $FePO_4$ (bottom) in LRO. Voltage evolution during the reduction (right). Asterisks mark peaks related to the setup and not the materials.

On the other hand, the peaks corresponding to $FePO_4$ gradually decrease in intensity during reduction while the peaks due to $LiFePO_4$ reappear towards the end of the process. Strikingly, the peaks corresponding to $FePO_4$ have not completely disappeared at the end of reduction, which may be related to an incomplete reaction. This would be in agreement with the fact that the specific capacity for the reduction step was somewhat lower than the theoretical value (see Table 4.2), although similar to the one obtained in coin cell. Beam-related phenomena also cannot be completely excluded.

Overall, the operando study does clearly show an effect of blending in the structural evolution of LRO during the first cycle, which seems to result in larger reversibility of the LRO processes taking place, as seen in Figure 4.18 where the patterns measured at the end of the discharge are overlapped to the ones taken just after cell mounting. Our results suggest that the existence of $FePO_4$ might have an impact in preventing the generation of the densified phase at high voltage and improves the reversibility of the structural characteristics – two phenomena possibly linked with each other. Yet, these are only preliminary hypotheses derived from the results obtained, which should be further refined to complete the evaluation of cell parameter evolution and further studied using complementary techniques, such as X-ray absorption.

.

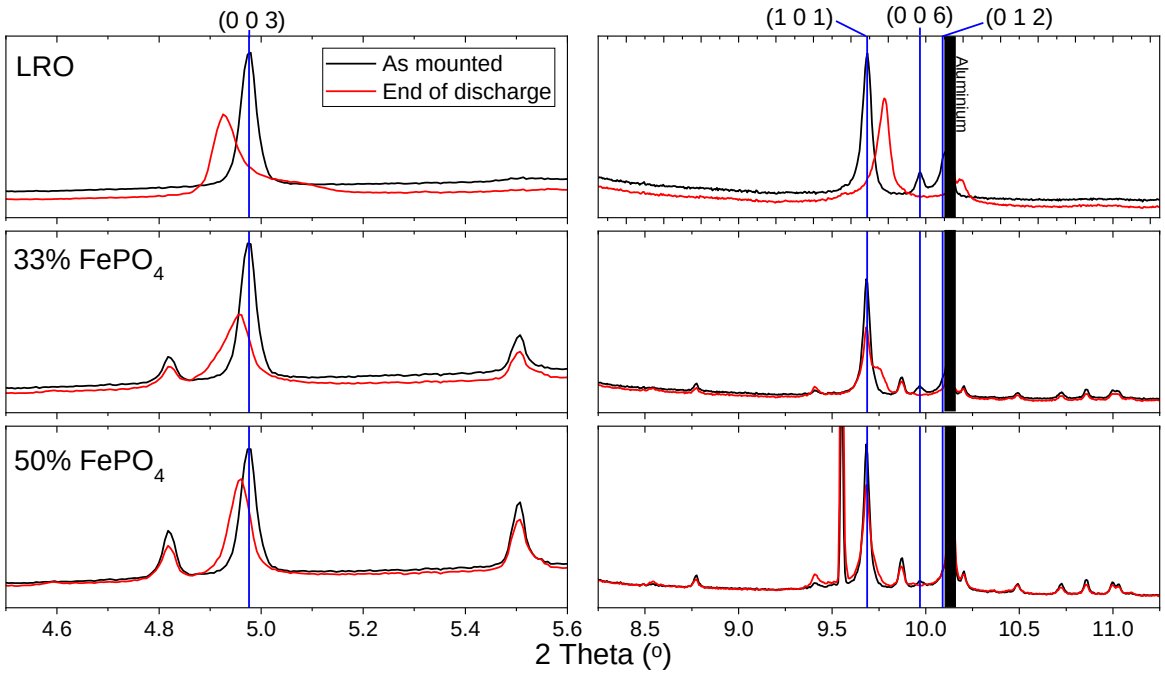

Figure 4.88: Comparison of the first, "as mounted" pattern of each cell (black) with the one at the end of discharge (red) for selected angular ranges. The LRO peaks are highlighted with blue lines. The black area covers a peak of the aluminium foil to improve visibility.

4.3.5 Effect of blending on the evolution of capacity upon cycling

In order to assess the evolution of capacity upon cycling for the blended electrodes, the assumption was made that a blend of LRO with $FePO_4$ or λ-MnO_2 would, after the first cycle, exhibit the same behaviour as those consisting of LRO mixed with $LiFePO_4$ (LFP) or $LiMn_2O_4$ (LMO), respectively. Thus, blends with the pristine lithiated materials were used for this part of the study to reduce the impact of the delithiation step that would have to be optimized for practical application.

The electrochemical testing protocol included a first oxidation up to 4.6V at C/30 and then after testing them in CC-CV protocol from 4.5 to 3.2V and different rates, they were cycled in CC mode at 1C for 160 cycles. Figure 4.19 shows the capacity vs. cycle number of the resulting blends at different rates, from C/10 up to 3C. As expected, the overall specific capacity of the blended electrodes is always lower than the one for pure LRO.

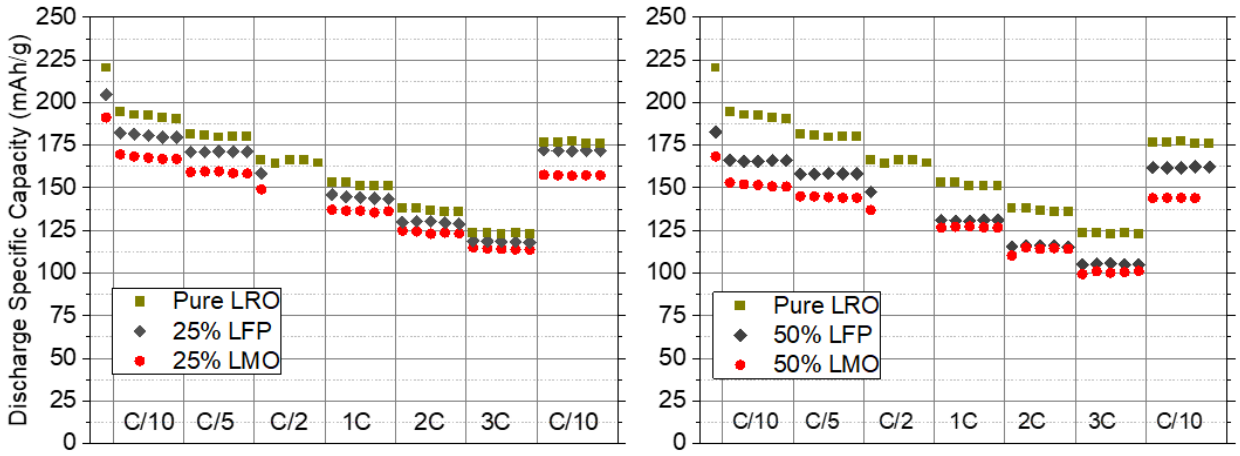

Figure 4.19: Discharge specific capability for multiple rates in the voltage window 4.5-3.2V (Except 1st cycle to 4.6V) of blends of 75% (left) and 50% (right) LRO with LMO or LFP.

Figure 4.20 shows the evolution of capacity upon cycling for 160 cycles for the same cells, after their activation at C/30 and rate testing. Interestingly, the capacity for pure LRO drops quickly during the first 10 cycles to values below the ones obtained for the blend containing 25% $LiFePO_4$. After only 25 cycles, the $LiFePO_4$ containing blends exhibit the highest specific capacities of the set, with the blend containing 50% $LiFePO_4$ exhibiting the lowest fading. The ultimate reason for this behaviour is not clear at the moment and while it may be related to a lower degree of transition metal dissolution, post-mortem studies would be needed to confirm this hypothesis. Furthermore, $LiFePO_4$ is generally known to perform well in long cycling tests and this could explain that the blend with the highest amount of it performs better.

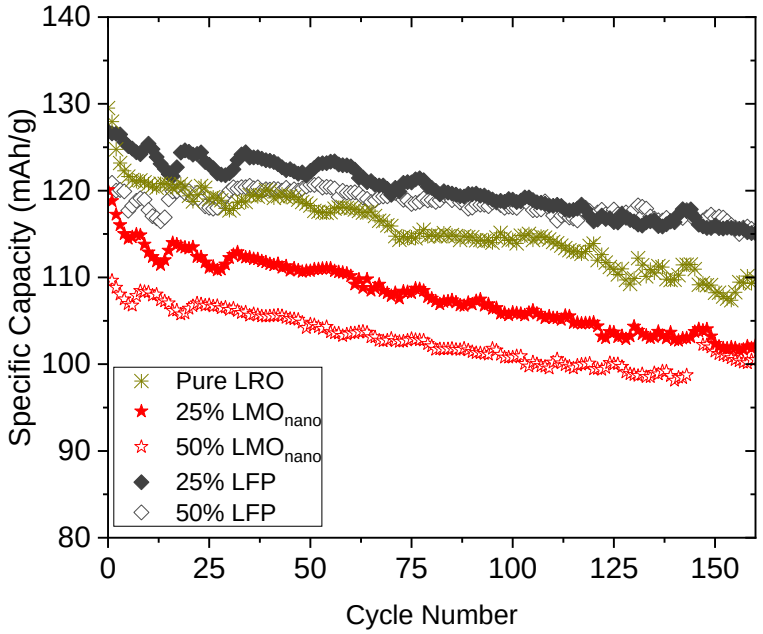

Figure 4.20: Capacity vs cycle number for 160 cycles at 1C between 4.5-3.2V done after prior activation and rate testing (see Figure 4.19). The oscillations observed are attributed to temperature fluctuations during measurement.

The average discharge voltage and energy achieved upon discharge are plotted in Figure 4.21 In terms of voltage, LRO falls nicely in between the blends with an average value of around 3.7V. When LMO is added, the voltage increases, as expected from the LMO operation potential, to reach 3.8V and 3.85V for the blends containing 25% and 50% LMO respectively. On the other hand, if $LiFePO_4$ is added to the blend, voltage is decreased to 3.62V and 3.5V for the blends containing 25% and 50% $LiFePO_4$ respectively. Regarding the energy delivered upon discharge, after only 2 cycles, the 25% $LiFePO_4$ blends deliver the highest energy, outperforming the pristine LRO and all other blends, which is related to the much higher capacity retention of $LiFePO_4$ compared to LMO containing blends, and to the higher voltage of 25 % $LiFePO_4$ as compared to 50% $LiFePO_4$.

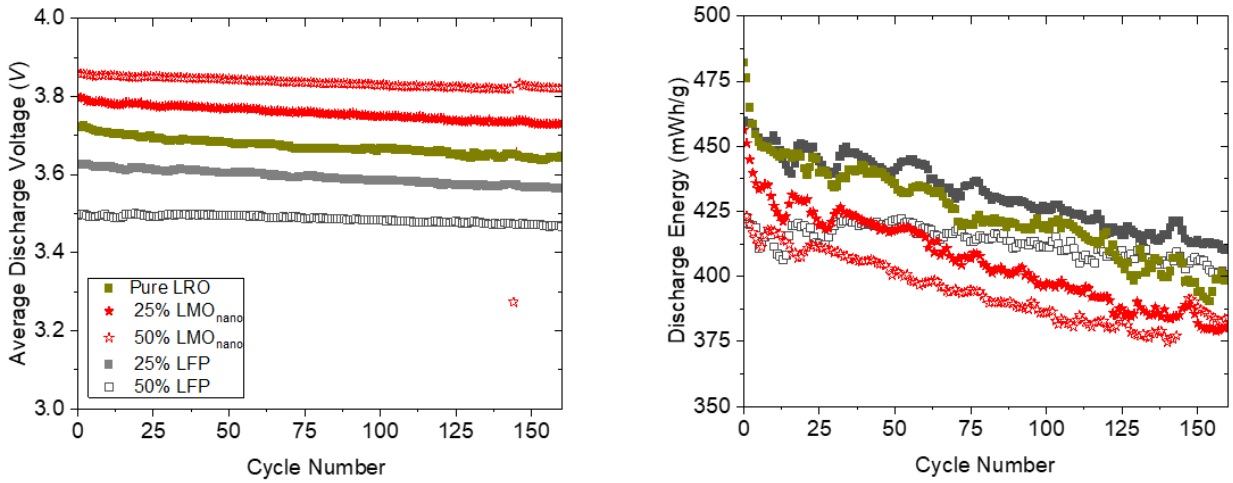

Figure 4.9: Average discharge voltage (left) and energy (right) of 160 cycles at 1C between 4.5-3.2V done after prior activation and rate testing (see Figure 4.19). The oscillations observed are attributed to temperature fluctuations during measurement

Overall, although the specific reasons for the observed improvement in capacity retention require further investigation, blending LRO with $LiFePO_4$ seems to contribute to improving electrochemical performance. Coupled to the effect on thermal stability described in previous sections, this finding encourages further research into this system.

4.4 Conclusions

A cobalt free, lithium rich layered oxide (LRO) with chemical composition $Li_{1.125}Ni_{0.312}Mn_{0.563}O_2$ was blended with chemically delithiated active materials, namely $FePO_4$ and λ-MnO_2 to observe and improve its performance. It was shown that blending with delithiated materials can result in a significant enhancement of the coulombic efficiency upon the first cycle, which is typically related to the so-called "activation process" in LRO. This is due to the fact that the delithiated compound can accommodate the lithium that would otherwise become inactive and stored at the negative electrode throughout the cell's lifetime. For the LRO – $FePO_4$ system, an amount of 33% $FePO_4$ was found to exhibit near zero first cycle irreversible capacity in half cells. The λ-MnO_2 – LRO system appeared to be more complicated and it was observed that greater care needs

to be taken when LRO is blended with materials of higher voltage due to the induction of increased sensitivity to humidity. DSC experiments showed that by adding $FePO_4$ to LRO, the temperature at which reactivity is observed shifts towards higher values and reduces the heat released which would render the electrodes safer for commercial use. Operando synchrotron X-Ray diffraction was also performed to the samples, to follow the structural evolution in the blend components upon operation and confirm the expected activity of $FePO_4$. Interestingly, the evolution of LRO during first reduction seems to be influenced by the presence of FePO4, which deserves further investigation. Finally, long term cycling experiments revealed that, after a few cycles, blends with $LiFePO_4$ exhibit better retention than pure LRO or blends with LMO, which paves the way for further studies in the system.

References

[1] M. S. Whittingham, "Lithium batteries and cathode materials," Chem Rev, vol. 104, no. 10, pp. 4271–4301, Oct. 2004, doi: 10.1021/cr020731c.

[2] A. Manthiram, "A reflection on lithium-ion battery cathode chemistry," Dec. 01, 2020, Nature Research. doi: 10.1038/s41467-020-15355-0.

[3] M. Casas-Cabanas, A. Ponrouch, and M. R. Palacín, "Blended Positive Electrodes for Li-Ion Batteries: From Empiricism to Rational Design," Jan. 01, 2021, John Wiley and Sons Inc. doi: 10.1002/ijch.202000099.

[4] A. J. Smith, S. R. Smith, T. Byrne, J. C. Burns, and J. R. Dahn, " Synergies in Blended LiMn 2 O 4 and Li[Ni 1/3 Mn 1/3 Co 1/3]O 2 Positive Electrodes ," J Electrochem Soc, vol. 159, no. 10, pp. A1696–A1701, 2012, doi: 10.1149/2.056210jes.

[5] C. Taubert, H. Y. Tran, M. Fleischhammer, P. Axmann, and M. Wohlfahrt-Mehrens, "LiMn2O4 spinel/LiNi0.8Co 0.15Al0.05O2 blends as cathode materials for lithium-ion batteries," in AABC 2010 - Advanced Automotive Battery Conference, 2010. doi: 10.1149/1.3560582.

[6] D. Chatzogiannakis et al., "Towards understanding the functional mechanism and synergistic effects of LiMn2O4 - LiNi0.5Mn0.3Co0.2O2 blended positive electrodes for Lithium-ion batteries," J Power Sources, vol. 591, p. 233804, 2024, doi: https://doi.org/10.1016/j.jpowsour.2023.233804.

[7] D. H. Doughty and E. P. Roth, "A General Discussion of Li Ion Battery Safety," Electrochem Soc Interface, vol. 21, no. 2, p. 37, Jan. 2012, doi: 10.1149/2.F03122if.

[8] Y. Dai and A. Panahi, "Thermal runaway process in lithium-ion batteries: A review," Next Energy, vol. 6, p. 100186, Jan. 2025, doi: 10.1016/j.nxener.2024.100186.

[9] J. Hou et al., "Unlocking the self-supported thermal runaway of high-energy lithium-ion batteries," Energy Storage Mater, vol. 39, pp. 395–402, Aug. 2021, doi: 10.1016/j.ensm.2021.04.035.

[10] H. Yang et al., "Simultaneously Dual Modification of Ni-Rich Layered Oxide Cathode for High-Energy Lithium-Ion Batteries," Adv Funct Mater, vol. 29, no. 13, Mar. 2019, doi: 10.1002/adfm.201808825.

[11] R. W. Schmitz et al., "Investigations on novel electrolytes, solvents and SEI additives for use in lithium-ion batteries: Systematic electrochemical characterization and detailed analysis by spectroscopic methods," Dec. 01, 2014, Elsevier Ltd. doi: 10.1016/j.progsolidstchem.2014.04.003.

[12] G. Sun et al., "Synergistic Effect between LiNi0.5Co0.2Mn0.3O2 and LiFe0.15Mn0.85PO4/C on Rate and Thermal Performance for Lithium Ion Batteries," ACS

Appl Mater Interfaces, vol. 10, no. 19, pp. 16458–16466, May 2018, doi: 10.1021/acsami.8b02102.

[13] P. Rozier and J. M. Tarascon, "Review—Li-Rich Layered Oxide Cathodes for Next-Generation Li-Ion Batteries: Chances and Challenges," J Electrochem Soc, vol. 162, no. 14, pp. A2490–A2499, 2015, doi: 10.1149/2.0111514jes.

[14] W. Zuo et al., "Li-rich cathodes for rechargeable Li-based batteries: Reaction mechanisms and advanced characterization techniques," Dec. 01, 2020, Royal Society of Chemistry. doi: 10.1039/d0ee01694b.

[15] G. Assat and J. M. Tarascon, "Fundamental understanding and practical challenges of anionic redox activity in Li-ion batteries," Nat Energy, vol. 3, no. 5, pp. 373–386, May 2018, doi: 10.1038/s41560-018-0097-0.

[16] G. Assat and J. M. Tarascon, "Fundamental understanding and practical challenges of anionic redox activity in Li-ion batteries," Nat Energy, vol. 3, no. 5, pp. 373–386, May 2018, doi: 10.1038/s41560-018-0097-0.

[17] H. Y. Jang et al., "Structurally robust lithium-rich layered oxides for high-energy and long-lasting cathodes," Nat Commun, vol. 15, no. 1, Dec. 2024, doi: 10.1038/s41467-024-45490-x.

[18] Z. Deng et al., "Challenges of thermal stability of high-energy layered oxide cathode materials for lithium-ion batteries: A review," Oct. 01, 2023, Elsevier B.V. doi: 10.1016/j.mattod.2023.07.024.

[19] H. Pan et al., "The Roles of Ni and Mn in the Thermal Stability of Lithium-Rich Manganese-Rich Oxide Cathode," Adv Energy Mater, vol. 13, no. 15, Apr. 2023, doi: 10.1002/aenm.202203989.

[20] "Umicore starts industrialization of manganese-rich battery materials technology for electric vehicles," https://www.umicore.com/en/news-stories/umicore-starts-industrialization-of-manganese-rich-battery-materials-technology-for-electric-vehicles, Feb. 12, 2023.

[21] J. Gao, J. Kim, and A. Manthiram, "High capacity Li[Li0.2Mn0.54Ni0.13Co0.13]O2-V2O5 composite cathodes with low irreversible capacity loss for lithium ion batteries," Electrochem commun, vol. 11, no. 1, pp. 84–86, Jan. 2009, doi: 10.1016/j.elecom.2008.10.036.

[22] J. Gao and A. Manthiram, "Eliminating the irreversible capacity loss of high capacity layered Li[Li0.2Mn0.54Ni0.13Co0.13]O2 cathode by blending with other lithium insertion hosts," J Power Sources, vol. 191, no. 2, pp. 644–647, Jun. 2009, doi: 10.1016/j.jpowsour.2009.02.005.

[23] L. Zhou, Z. Yin, Z. Ding, X. Li, Z. Wang, and Y. Wang, "Bulk and surface reconstructed Li-rich Mn-based cathode material for lithium ion batteries with eliminating irreversible capacity loss," Journal of Electroanalytical Chemistry, vol. 829, pp. 7–15, Nov. 2018, doi: 10.1016/j.jelechem.2018.09.043.

[24] X. Hu et al., "Structural and electrochemical characterization of NH4F-pretreated lithium-rich layered Li[Li0.2Ni0.13Co0.13Mn0.54]O2 cathodes for lithium-ion batteries," Ceram Int, vol. 44, no. 12, pp. 14370–14376, Aug. 2018, doi: 10.1016/j.ceramint.2018.05.046.

[25] J. Zheng et al., "The effects of persulfate treatment on the electrochemical properties of Li[Li 0.2Mn 0.54Ni 0.13Co 0.13]O 2 cathode material," J Power Sources, vol. 221, pp. 108–113, Jan. 2013, doi: 10.1016/j.jpowsour.2012.06.084.

[26] Z. Wang, E. Liu, C. He, C. Shi, J. Li, and N. Zhao, "Effect of amorphous FePO4 coating on structure and electrochemical performance of Li1.2Ni0.13Co 0.13Mn0.54O2 as cathode material for Li-ion batteries," J Power Sources, vol. 236, pp. 25–32, 2013, doi: 10.1016/j.jpowsour.2013.02.022.

[27] J. C. Hunter, "Preparation of a New Crystal Form of Manganese Dioxide: A-MnO," 1981.

[28] M. Galceran, A. Guerfi, M. Armand, K. Zaghib, and M. Casas-Cabanas, " The Critical Role of Carbon in the Chemical Delithiation Kinetics of LiFePO 4 ," J Electrochem Soc, vol. 167, no. 7, p. 070538, Jan. 2020, doi: 10.1149/1945-7111/ab7ce3.

[29] M. Herklotz et al., "A novel high-throughput setup for in situ powder diffraction on coin cell batteries," J Appl Crystallogr, vol. 49, no. 1, pp. 340–345, Feb. 2016, doi: 10.1107/S1600576715022165.

[30] J. Rodriguez-Carvajal, "Recent advances in magnetic structure determination neutron powder diffraction," 1993.

[31] O. Arcelus et al., "FullProfAPP: a graphical user interface for the streamlined automation of powder diffraction data analysis," J Appl Crystallogr, vol. 57, pp. 1676–1690, Oct. 2024, doi: 10.1107/S1600576724006885.

[32] Z. Zhang, D. Fouchard, and J. R. Rea, "Differential scanning calorimetry material studies: implications for the safety of lithium-ion cells," 1998.

[33] J. Hou et al., "Unlocking the self-supported thermal runaway of high-energy lithium-ion batteries," Energy Storage Mater, vol. 39, pp. 395–402, Aug. 2021, doi: 10.1016/j.ensm.2021.04.035.

[34] J. Geder, J. H. Song, S. H. Kang, and D. Y. W. Yu, "Thermal stability of lithium-rich manganese-based cathode," Solid State Ion, vol. 268, no. PB, pp. 242–246, Dec. 2014, doi: 10.1016/j.ssi.2014.05.020.

[35] B. Mortemard de Boisse et al., "Coulombic self-ordering upon charging a large-capacity layered cathode material for rechargeable batteries," Nat Commun, vol. 10, no. 1, Dec. 2019, doi: 10.1038/s41467-019-09409-1.

[36] W. Yin et al., "Structural evolution at the oxidative and reductive limits in the first electrochemical cycle of Li1.2Ni0.13Mn0.54Co0.13O2," Nat Commun, vol. 11, no. 1, Dec. 2020, doi: 10.1038/s41467-020-14927-4.

[37] D. Qian, B. Xu, M. Chi, and Y. S. Meng, "Uncovering the roles of oxygen vacancies in cation migration in lithium excess layered oxides," in Physical Chemistry Chemical Physics, Royal Society of Chemistry, Jul. 2014, pp. 14665–14668. doi: 10.1039/c4cp01799d.

[38] H. Koga et al., "Operando X-ray absorption study of the redox processes involved upon cycling of the li-rich layered oxide Li1.20Mn0.54Co 0.13Ni0.13O2 in li ion batteries," Journal of Physical Chemistry C, vol. 118, no. 11, pp. 5700–5709, Mar. 2014, doi: 10.1021/jp412197z.

[39] A. Ito, Y. Sato, T. Sanada, M. Hatano, H. Horie, and Y. Ohsawa, "In situ X-ray absorption spectroscopic study of Li-rich layered cathode material Li[Ni0.17Li0.2Co0.07Mn 0.56]O2," J Power Sources, vol. 196, no. 16, pp. 6828–6834, Aug. 2011, doi: 10.1016/j.jpowsour.2010.09.105.

[40] M. Sathiya, J. B. Leriche, E. Salager, D. Gourier, J. M. Tarascon, and H. Vezin, "Electron paramagnetic resonance imaging for real-time monitoring of Li-ion batteries," Nat Commun, vol. 6, Feb. 2015, doi: 10.1038/ncomms7276.

[41] R. A. House et al., "First-cycle voltage hysteresis in Li-rich 3d cathodes associated with molecular O2 trapped in the bulk," Nat Energy, vol. 5, no. 10, pp. 777–785, Oct. 2020, doi: 10.1038/s41560-020-00697-2.

[42] R. A. House et al., "Covalency does not suppress O2 formation in 4d and 5d Li-rich O-redox cathodes," Nat Commun, vol. 12, no. 1, Dec. 2021, doi: 10.1038/s41467-021-23154-4.

[43] H. Liu et al., "Operando Lithium Dynamics in the Li-Rich Layered Oxide Cathode Material via Neutron Diffraction," Adv Energy Mater, vol. 6, no. 7, Apr. 2016, doi: 10.1002/aenm.201502143.

[44] T. Jousseaume, J. F. Colin, M. Chandesris, S. Lyonnard, and S. Tardif, "How Beam Damage Can Skew Synchrotron Operando Studies of Batteries," ACS Energy Lett, vol. 8, no. 8, pp. 3323–3329, Aug. 2023, doi: 10.1021/acsenergylett.3c00815.

[45] A. P. Black et al., "Beam Effects in Synchrotron Radiation Operando Characterization of Battery Materials: X-Ray Diffraction and Absorption Study of LiNi0.33Mn0.33Co0.33O2

and LiFePO4 Electrodes," Chemistry of Materials, vol. 36, no. 11, pp. 5596–5610, Jun. 2024, doi: 10.1021/acs.chemmater.4c00597.

5. Decoupling silicon and graphite contribution in high silicon blended electrodes

5.1 Introduction

The incremental but steady progress in Li-ion battery performance has broadened their field of application from portable electronics to transportation and beyond. Improving energy density has been a primary research focus, with the use of alloy-based negative electrodes, such as silicon, showing breakthrough potential thanks to their high capacities. Unfortunately, commercial use remains limited to the addition of a small percentage of silicon to the graphite negative electrode (8-10% in most cases), as the very high capacity involves significant volume changes (more than three times of original value) which introduce strains in both the particles and the solid electrolyte interphase (SEI) that cause severe capacity fading. [1], [2], [3], [4], [5], [6], [7]

The behaviour of graphite and silicon is well known, with each material involving different redox steps associated with the formation of different phases. In graphite anodes, lithium intercalation occurs through a "staging" mechanism, where lithium ions progressively occupy specific interlayers between the carbon layers, allowing for a gradual and controlled increase in lithium concentration during the electrochemical reaction. The stages include Stage IV, (where lithium occupies every fourth interlayer; Stage III, with lithium in every third interlayer; Stage II, where lithium fills every second interlayer; and finally, Stage I, the fully lithiated phase, in which lithium ions occupy all available interlayer spaces to form LiC_6. Stage II corresponds to $Li_{0.5}C_6$, while there are some discrepancies regarding the composition of stages III and IV [8] In the case of silicon, the mechanism is slightly different depending whether the starting material is amorphous or crystalline and crystalline silicon will first transform into an amorphous Li_xSi phase ($0<x<3.75$). [9]Crystalline $Li_{15}Si_4$ will ultimately form at high levels of lithiation (potential below ca. 50 mV), although the formation of this phase is typically not fully reversible.[10], [11] Upon delithiation, this crystalline phase transforms back into the amorphous phase.[12] When blending crystalline silicon with graphite, one would expect first lithiation of silicon to produce the amorphous alloy, then lithiation of graphite with formation of stages, and finally formation of $Li_{15}Si_4$ at low potential. Upon

oxidation, and due to the lower polarization exhibited by graphite, graphite would delithiate prior to the delithiation of either $Li_{15}Si_4$ or Li_xSi.

Despite a myriad of papers devoted to the electrochemical characterization of Si/C electrodes, mechanistic studies are more scarce. Meaningful insights were reported by Yao et al. [13] from an operando energy dispersive X-ray diffraction study in coin cells with electrodes containing 73% of graphite and 15% of Si nanoparticles (wt.%) operating at C/30. By quantifying the amount of lithium in the graphite crystalline phases they were able to confirm the expected mechanism described above and the differential capacity dQ/dV exhibited both the peaks corresponding to graphite and silicon. Interestingly, the peaks corresponding to graphite in the Si/Graphite electrodes were observed at the same potential as in cells containing no silicon in the working electrode. This would point at the absence of interaction between the two active material components present in the electrode in the operation conditions investigated. Indeed, studies of Si/Graphite blends have often assumed that the capacities of both materials were simply additive [14] yet, one could wonder if this is always the case, as the transfer of lithium between two active materials present in the same electrode is well documented in the more studied blended positive electrode materials. [15], [16], [17], [18], [19]

Indeed, the possibility of transfer of lithium from LiC_6 to silicon was already discussed by Richter et al. when investigating the ageing mechanism and low temperature operation of Si/graphite electrodes containing 3.5% wt. of micrometric Si. [20] This was further studied by Heubner et al. [21] using the same three electrode experimental setup they had developed to study blended positive electrodes.[22] This setup uses a lithium counter electrode and two connected working electrodes each containing one of the pure blend components, allowing the measurement of the current flowing between them during cell operation. In that study, an electrode containing graphite was used on one side and a sputtered silicon thin film on the other, and the deconvolution of the respective contributions to the capacity enabled to confirm lithium redistribution

within the electrode, with silicon being beneficial not only in terms of capacity but also in terms of rate capability.

The aim of this work is to extend the study by Heubner et al. to assess also the influence of temperature and investigate composite electrodes, creating a setup more representative of those in commercial cells. A previously reported Si/graphite mixture, prepared by a wet ball milling process, along with its individual components, were chosen as active materials for this study. This composite electrode was selected due to the good performance achieved even with high silicon loadings (30 % in wt.), providing a valuable reference point for comparing our results. [23]

5.2 Experimental Details

5.2.1 Electrode Fabrication

The graphite electrode was cast using a protocol adapted from one used for positive electrodes using N-Methyl-2-pyrrolidone (NMP, Sigma-Aldrich) as a solvent, Polyvinylidene fluoride, PVDF (Solvay) binder and C65 carbon additive (Imerys). Initially, a 5%wt. solution of the binder was made using magnetic stirring. The graphite powder used was also purchased from Imerys (D_{50} = 12-13μm). The graphite and C65 powders were premixed and then added to a previously weighted amount of the binder solution while vigorously stirring using an IKA T 25 digital ULTRA-TURRAX® until a homogeneous slurry was obtained. A small amount of pure NMP was added during this process to adjust the viscosity. Crystalline silicon nanoparticles (Alfa-Aesar) with diameters of less than 50nm were used for the silicon electrodes. In this case, electrodes were cast from a water-based slurry using lithium poly-acrylic acid (Li-PAA),[24] a water-soluble binder frequently used for silicon which allows forming a more stable SEI and exhibits a stronger interaction with silicon compared to other aqueous-based binders such as CMC. This particular binder was the same one used in the reference composite electrode [23]. In order to prepare the slurry, the carbon additive and silicon

nanoparticles were initially ball-milled for 20 minutes prior to their use. After that, the process followed was identical to the one described above for graphite using water instead of NMP. Most electrodes fabricated with pure silicon faced issues such as partial dewetting after casting or delamination and cracking of the film from the from the copper substrate after drying. To address these issues, adjustments were made to the slurry viscosity and tape casting which enabled some improvement. The best electrodes had enough adhesion to be assembled and tested, delivering satisfactory electrochemical performance despite still exhibiting some surface cracking. The silicon graphite blended electrode is described in reference [23] with FLG (few layer graphene) being used as conducting additive. All the electrodes prepared contained 80% wt. active material, 10% wt. binder and 10% wt. carbon additive. Scanning Electron Microscopy (SEM) images of the electrodes and the active materials are included in the supporting information Sand were taken with a FEI Quanta 200 ESEM FEG microscope.

5.2.2 Electrochemical testing

All the electrochemical tests were conducted using a VMP3 (Biologic, France). Cells underwent an initial formation cycle between 0.005V and 0.9V vs. Li/Li^+ at room temperature and were subsequently cycled at the specified temperatures (Room temperature (RT), 0 and 45°C) and rates between 0.05V and 0.9V. For all the electrochemical protocols, a 1h constant voltage step was introduced at each cutoff voltage. To prepare CR2032 coin cells, all components were first dried at 70°C to remove any moisture. Electrodes with a diameter of 14 mm were punched from the prepared laminates, and their mass is reported in Table SI 5.1. The punched electrodes were then dried in a Büchi oven under vacuum at 120°C for at least one hour. After drying, both the coin cell parts and electrodes were transferred to an argon filled glove box where the assembly took place. Lithium metal was used as a counter electrode and Whatman borosilicate glass fiber filter, soaked with electrolyte (1M $LiPF_6$ in EC:DMC) as separator.

The three electrode "decoupled blend" cell setup assembly and electrical connection are described in detail in [19] and is based on the method developed by Heubner et al.

[22] bearing a lithium metal counter electrode between two working electrodes. Both working electrodes are maintained at the same potential using a potentiostat channel (ΔV = 0V). During testing, they are cycled against the lithium metal and the current flowing to/from each working electrode is recorded.

For the measurements done at 0 °C and 45 °C, a recirculating bath (Thermo Scientific) filled with silicone oil was employed. The first cycle of all cells was performed at room temperature. Afterwards, they were placed inside individual airtight plastic bags, submerged in the oil, and allowed to reach thermal equilibrium for at least 24 hours. Following this thermalization period, the desired electrochemical test was performed.

5.3 Results and Discussion

First, the electrochemical properties of the individual components were characterized in coin cells to assess their individual behaviours under different conditions. Next, the blended electrode was characterized, and finally, the decoupled blend setup was evaluated to follow lithium dynamics.

5.3.1 Electrochemical testing

5.3.1.1 Graphite electrodes

The electrochemical performance of graphite electrodes was assessed by Galvanostatic Cycling with Potential Limitation (GCPL) initially down to 0.005V for the formation cycle and then cycled between 0.9V and 0.05V. Tests were done at room temperature (RT) and also at higher (45°C) and lower (0°C) temperatures. Figure 5.1 shows the voltage profile after the formation cycle as a function of the specific capacity at C/20.

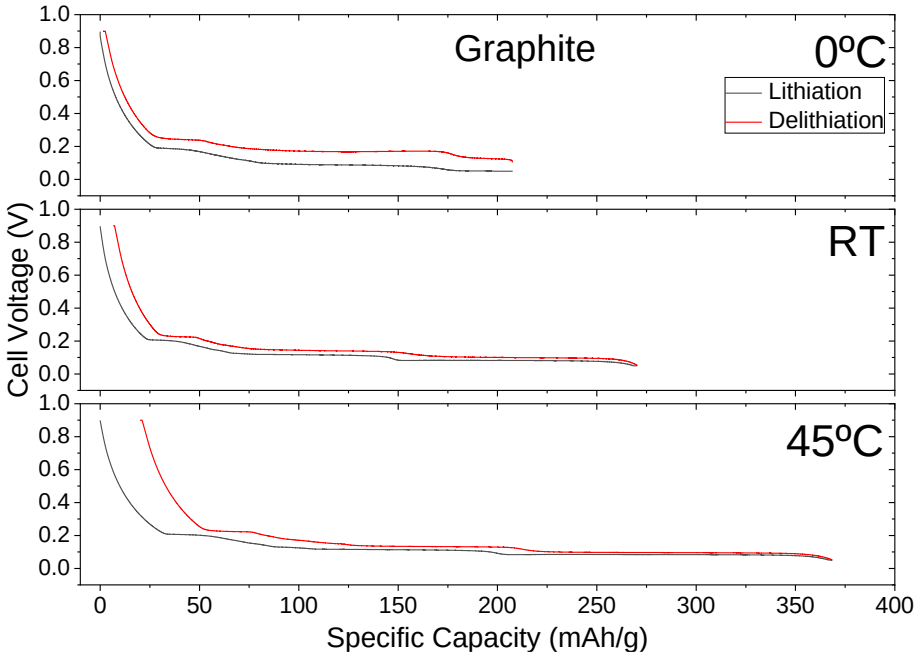

Figure 5.1: Cell voltage as a function of specific capacity for the first cycle after formation for graphite half cells at C/20 and three different temperatures: 0ºC (top), RT (middle) and 45ºC (bottom)., Both lithiation (black lines) and delithiation (red lines) curves are depicted.

In agreement with the well-known behaviour of graphite, both lithiation and delithiation curves exhibit distinct plateaus that correspond to the formation of different stages. The results indicate that temperature plays an important role in the performance of the electrodes, and this is reflected in three different aspects. Firstly, an impact on the reversible specific capacities is observed, monotonically increasing from 205 mAh/g for 0ºC to 263 mAh/g for RT and finally 348 mAh/g for 45ºC. Second, coulombic efficiencies were also slightly different, with 99%, 97% and 95% for 0ºC, 25ºC and 45ºC respectively. Last, a difference is witnessed in the polarization of the cells as a function of temperature. This is the potential difference between the profiles during reduction (intercalation of lithium) and oxidation (de-intercalation of lithium) caused by internal resistances and reaction kinetics which at low temperature can also be impacted by the decreased ionic conductivity of the electrolyte. Figure 5.2 shows the differential specific capacity (dQ/dV) as a function of cell voltage for the curves depicted in Figure 5.1. The peak potential values are reported both upon oxidation and reduction in Table 5.1.

As expected, the cell polarization decreases consistently with increasing temperature. This difference ranges from 0.080V for Stage II at 0°C to 0.012V for Stage I at 45°C. At 0°C, during lithiation, only a portion of stage I is visible due to the cutoff voltage, and therefore the cutoff voltage value was taken (0.05V). Interestingly, for a given temperature, all three peaks exhibit comparable potential differences between charge and discharge. The values of the peaks are roughly consistent with previously reported data at both low [25] and high [26] temperatures.

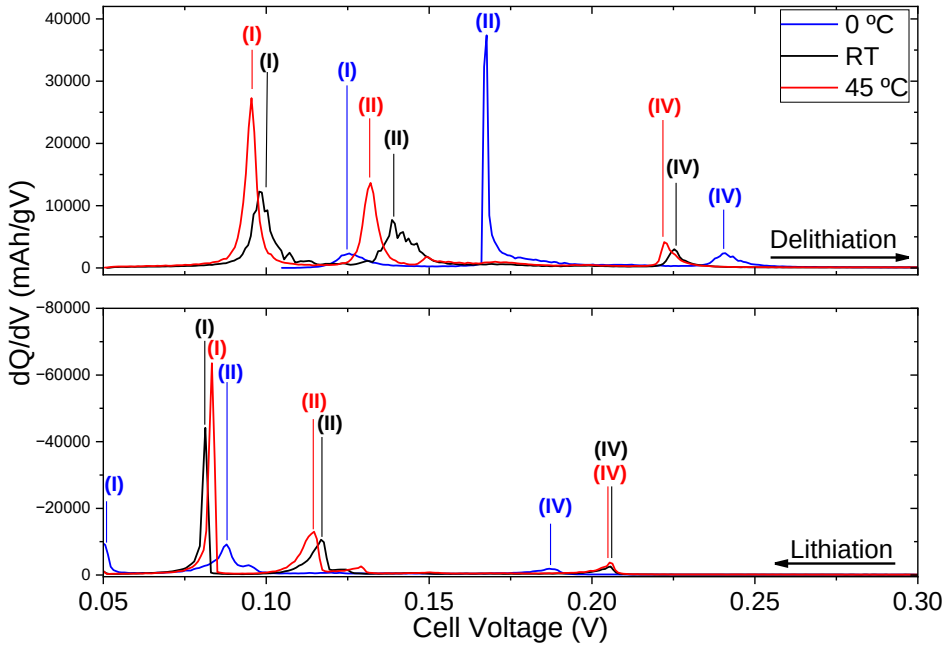

Figure 5.2: Differential specific capacity (dQ/dV) of graphite electrodes at C/20 for the temperatures studied, 0°C (blue lines), RT (black lines) and 45°C (red lines) during delithiation (top) and lithiation (bottom). Each peak is assigned to the corresponding graphite stage (I,II,IV). The voltage range depicted is chosen for better visibility and contains all observed peaks.

Table 5.3: Voltage values of the dQ/dV maxima for graphite half cells measured at 0°C, RT and 40°C

	Stage I			**Stage II**			**Stage IV**		
	Lithiation	*De-lithiation*	**Difference**	*Lithiation*	*De-lithiation*	**Difference**	*Lithiation*	*De-lithiation*	**Difference**
0°C	*0.05 V*	*0.126 V*	***0.076 V***	*0.088 V*	*0.168 V*	***0.080 V***	*0.168 V*	*0.240 V*	***0.072 V***
RT	*0.081 V*	*0.098 V*	***0.017 V***	*0.117 V*	*0.139 V*	***0.022 V***	*0.205 V*	*0.224 V*	***0.019 V***
45°C	*0.083 V*	*0.095 V*	***0.012 V***	*0.115 V*	*0.132 V*	***0.017 V***	*0.205 V*	*0.222 V*	***0.017 V***

Higher rates, up to 3C, were also tested to follow the change in their specific capacity with increasing rate. Note that the capacities reported correspond to the constant current portion of the cycling protocol, excluding capacity contributed during the constant voltage step. For the coulombic efficiency, however, the total capacity is taken into account (both constant current and constant voltage steps). An example is shown in Figure 5.3 depicting how capacity values are taken.

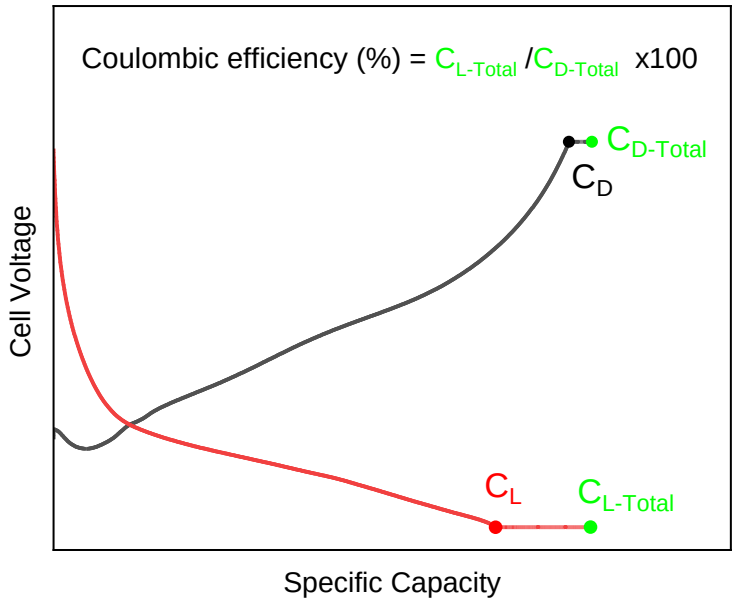

Figure 5.3: Graphic illustration of the procedure to calculate the coulombic efficiency and the specific capacities of lithiation (C_L) and delithiation (C_D)

Figure 5.4 depicts the specific capacities obtained for both lithiation and delithiation processes. Interestingly, delithiation exhibits higher capacities at all temperatures, with almost unchanged capacity across cycling rates at 45°C and RT. At 0°C, however, the capacity gradually decreases from around 200 mAh/g at C/20 down to around 85 mAh/g at rates higher than 1C. As expected, lower temperatures lead to an overall reduction in capacity which could be partially attributed to the lower ionic conductivity of the electrolyte at low temperatures. [27]

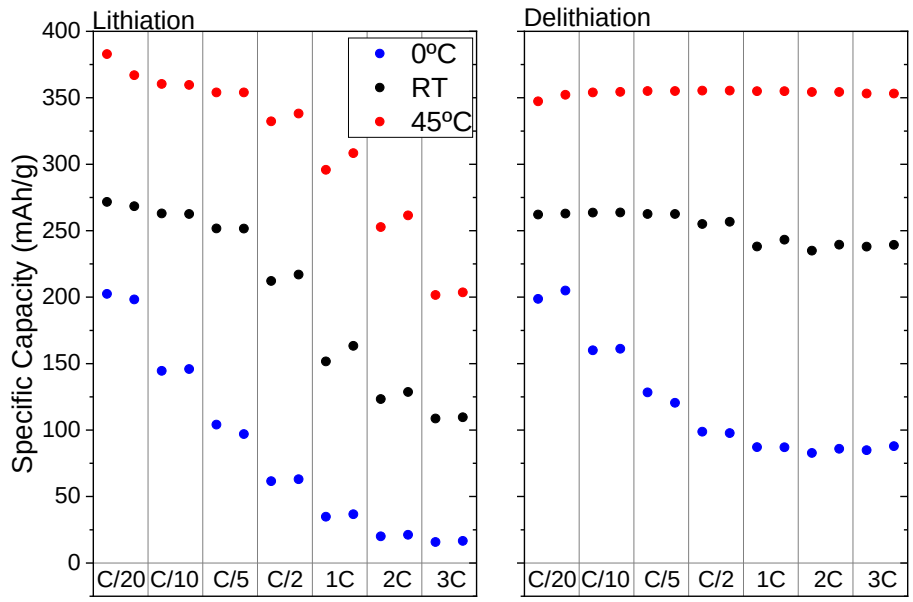

Figure 5.4: Specific capacities measured for graphite at the three temperatures studied for different lithiation and delithiation rates.

5.3.1.2 Silicon electrodes

The potential vs. composition profile of electrodes containing only silicon as active material, measured at C/20 and within the same voltage range, exhibit a sloping behaviour (see Figure 5.5) [10] .

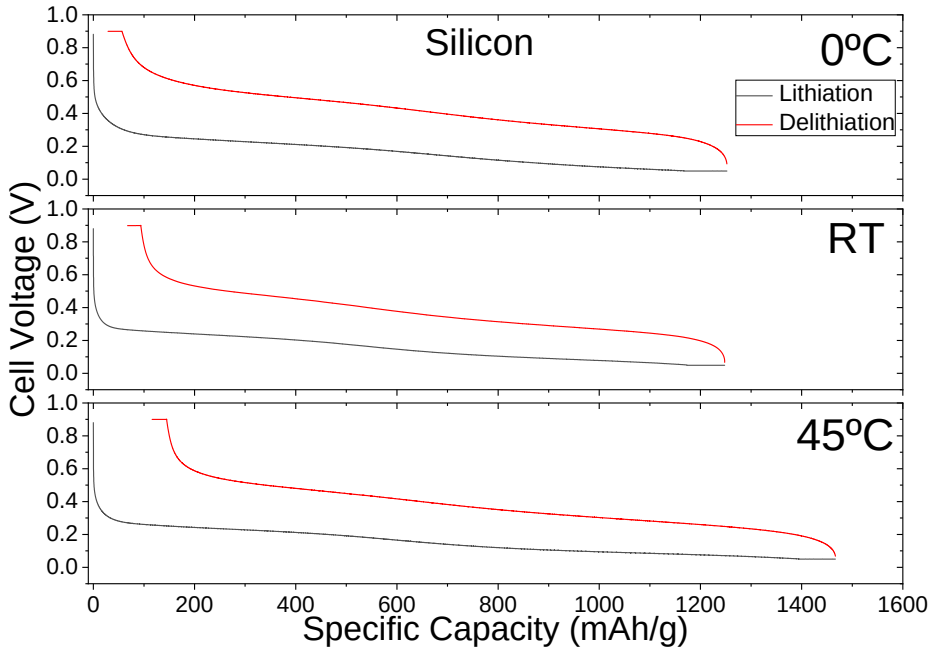

Figure 5.5: Cell voltage as a function of specific capacity for the silicon half cells at C/20 at three different temperatures. 0ºC (top), RT (middle) and 45ºC (bottom), Both lithiation (black lines) and delithiation (red lines) steps are depicted.

The impact of temperature on specific capacity and lithiation reversibility is also significant, with higher temperatures generally exhibiting enhanced specific capacity, and similar values being achieved at 0ºC and RT (1222 mAh/g and 1181 mAh/g for 0ºC and RT respectively), in contrast with the case of graphite. A notable increase in the specific capacity was observed at 45ºC, reaching 1350 mAh/g. Temperature also seems to influence the reversibility of the lithiation process, as the coulombic efficiency decreases when the temperature is increased, with 98% at 0ºC, 95% at 25ºC, and 92% at 45ºC.

The plot of dQ/dV vs. potential exhibits two very broad peaks centered at higher voltages than those observed for graphite (see Figure 5.6). For this work they will be labeled A and B, with A being the one appearing at lower potentials. This behaviour is consistent with previous results in the literature.[9], [12] Peak B corresponds to the transformation of amorphous-Si → amorphous-Li_2Si while peak A the amorphous-Li_2Si

→ *amorphous-$Li_{3.5}Si$.[28] Similarly to graphite the low voltage process is limited by the cutoff voltage at low temperatures and therefore, its value cannot be accurately determined as it appears below 0.05V. Interestingly, at RT and 45ºC the position of the peaks is the same. Moving to low temperature causes a shift of the peaks towards higher voltages during delithiation. During lithiation, peak A is also shifted, in this case towards lower voltages, but peak B shows a very subtle shift, if any.*

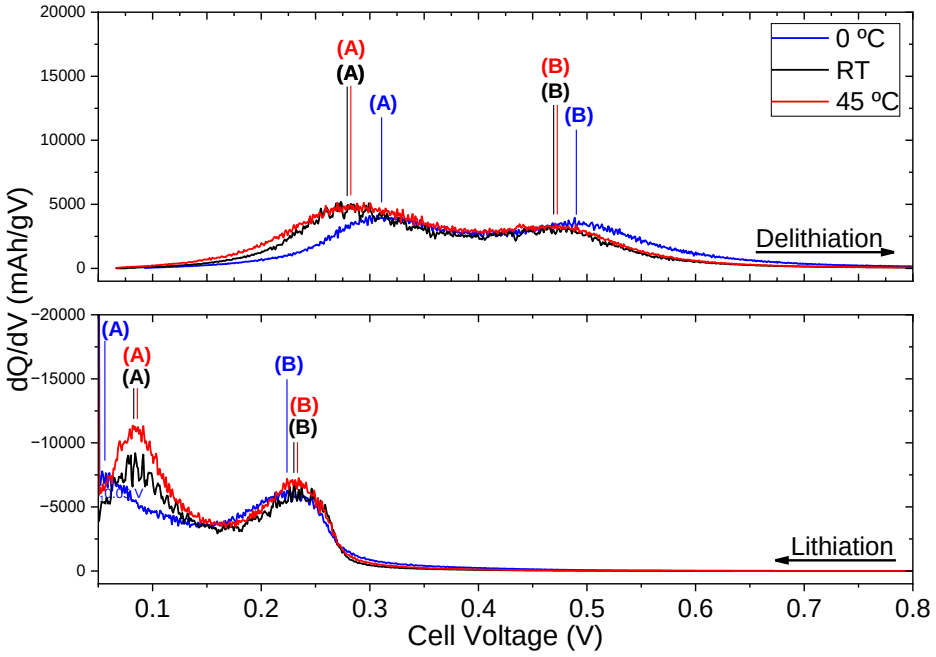

Figure 5.6: Differential specific capacity (dQ/dV) of silicon electrodes at C/20 for the temperatures studied, 0ºC (blue lines), RT (black lines) and 45ºC (red lines) during delithiation (top) and lithiation (bottom). The two peaks corresponding to silicon were labelled as A and B (see text).. The voltage range depicted is chosen for better visibility and contains all observed peaks.

Table 5.2 includes the corresponding voltage values as well as their difference between charge and discharge processes. Even though silicon and graphite curves are not directly comparable due to the breadth of the peaks, silicon exhibits larger potential differences than graphite and its activity extending to much higher voltages, in agreement with their well-known behaviour (see Introduction section). Indeed, silicon is still active at voltages higher than 0.5 V whereas graphite completed its delithiation below 0.3 V.

Table 5.4: Voltage values of the dQ/dV maxima for silicon half cells measured at 0°C, RT and 40°C

	Silicon A			**Silicon B**		
	Lithiation	*Delithiation*	***Difference***	*Lithiation*	*Delithiation*	***Difference***
0°C	*0.05*	*0.31*	***0.26***	*0.22*	*0.49*	***0.27***
RT	*0.08*	*0.28*	***0.20***	*0.23*	*0.47*	***0.24***
45°C	*0.08*	*0.28*	***0.20***	*0.23*	*0.47*	***0.24***

Capacities obtained at higher rates for silicon are shown in Figure 5.7, calculated using the same protocol described in Figure 5.3. Contrary to what was expected, the lower temperature cell outperforms the other two. This cannot be explained in terms of kinetics since higher temperatures should promote a faster and more complete reaction and also higher ionic conductivity for the electrolyte is expected. Yet, higher temperatures can both result in side reactions related to electrolyte decomposition and/or accelerate degradation processes related to silicon itself, causing more severe mechanical breakdown and faster SEI growth.

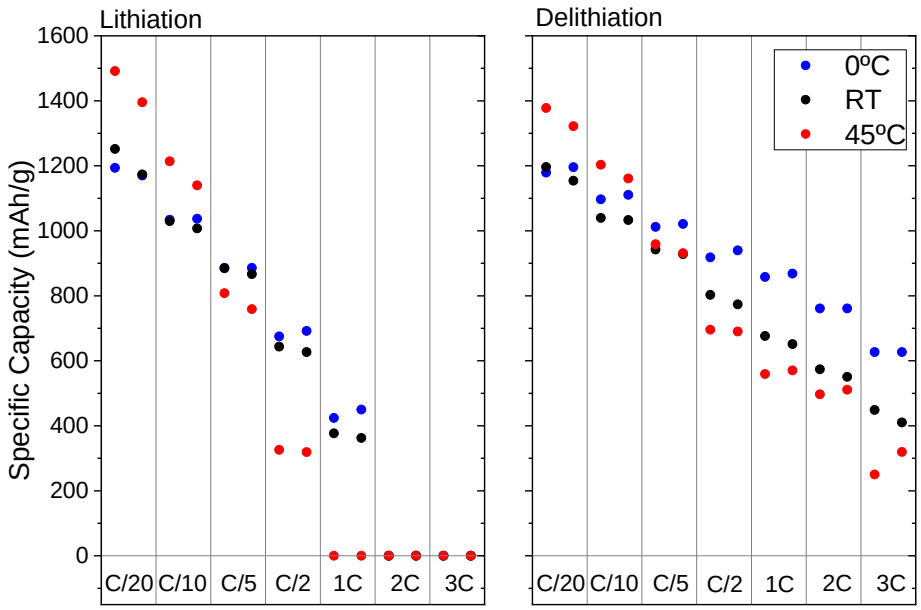

Figure 5.7: Specific capacities measured for silicon in the three temperatures studied for different rates of lithiation and delithiation.

On the other hand, the rate capability of pure silicon is worse than that of graphite, as the capacity rapidly decays with increasing rate, and there is no available capacity above 1C during lithiation. It should be also noted that, as explained in the Experimental section, obtaining a homogeneous laminate of pure silicon represented a challenge, further exacerbating performance issues at higher rates.

5.3.1.3 Blended electrodes

In order to understand the effect of blending graphite and silicon in a single electrode, a laminate with an active mass consisting of 30% silicon and 70% graphite by mass was tested in half-cell configuration. The same tests as for the pure components were run for all temperatures and Figure 5.8 shows the corresponding voltages curves as a function of capacity.

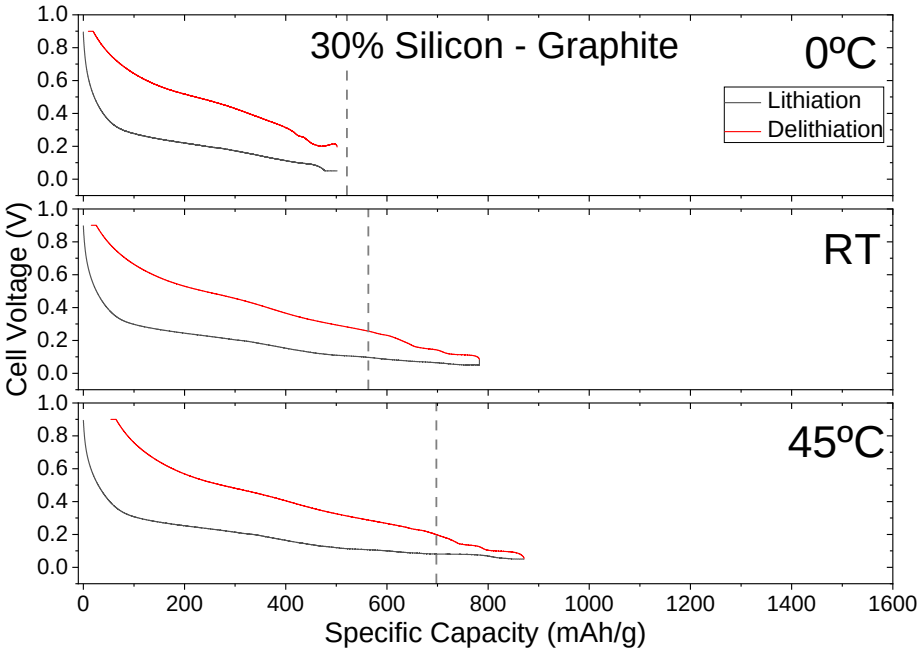

Figure 5.8: Cell voltage as a function of specific capacity at C/20 for the blended (70% graphite – 30% silicon) half cells at three different temperatures. 0ºC (top), RT (middle) and 45ºC (bottom), Both lithiation (black lines) and delithiation (red lines) steps are depicted. The theoretical capacity value for the blend is also included (grey dashed line).

As expected, the overall specific capacities obtained by the blended electrodes fall between those of the pure components. Table 5.3 shows the reversible specific capacities and coulombic efficiencies obtained for all measured samples (pure components and blends). Interestingly, the coulombic efficiencies appear to reduce at higher temperatures as observed for the components.

Table 5.3: Values of reversible capacities obtained for all the studied samples and temperatures, together with coulombic efficiencies.

	Graphite		Silicon		Blend	
	Reversible Capacity (mAh/g)	Coulombic Efficiency	Reversible Capacity (mAh/g)	Coulombic Efficiency	Reversible Capacity (mAh/g)	Coulombic Efficiency
0 ºC	205	99 %	1222	98 %	492	98 %
RT	263	97 %	1181	95 %	766	98 %
45 ºC	348	95 %	1350	92 %	871	94%

The expected lithiation capacity of the blend was calculated for each temperature using the rule of mixture formula shown below :

$$C_{30\%\,Blend} = 0.3\,C_{Silicon} + 0.7\,C_{Graphite}$$

Where $C_{Silicon}$ and $C_{Graphite}$ correspond to the values measured for the pure electrodes at each temperature and given in Table 5.3. The calculated values are compared to the measured ones in Table 5.4, together with the difference between the two:

Table 5.4: Total specific capacity values obtained for silicon, graphite, blended electrode and the expected capacity of the latter. All values are in mAh/g.

	Silicon	Graphite	Rule of mixture	Blend
0 ºC	1252	208	521	502 (-4%)
RT	1248	270	563	783 (+28%)
45 ºC	1467	368	698	871 (+20%)

The values indicate that there is a significant gain in capacity by blending, even at C/20 which contrasts with the behaviour observed previously in positive electrode materials, where this improvement was only seen at high rates.[19] This gain is however lost at low temperatures which may be related to the kinetics of the materials themselves but could also be influenced by the lower electrolyte ionic conductivity.

The rate capability of the blended electrodes was also evaluated. Figure 5.9 shows the specific capacities obtained at each rate and temperature for both lithiation and delithiation processes. Similarly to the pure components, lithiation capacities are more affected by increasing rates. As expected, samples tested at higher temperatures deliver higher capacities and exhibit weaker dependence on rate. However, and contrary to pure silicon, even at 0 ºC some capacity is achieved at 3C.

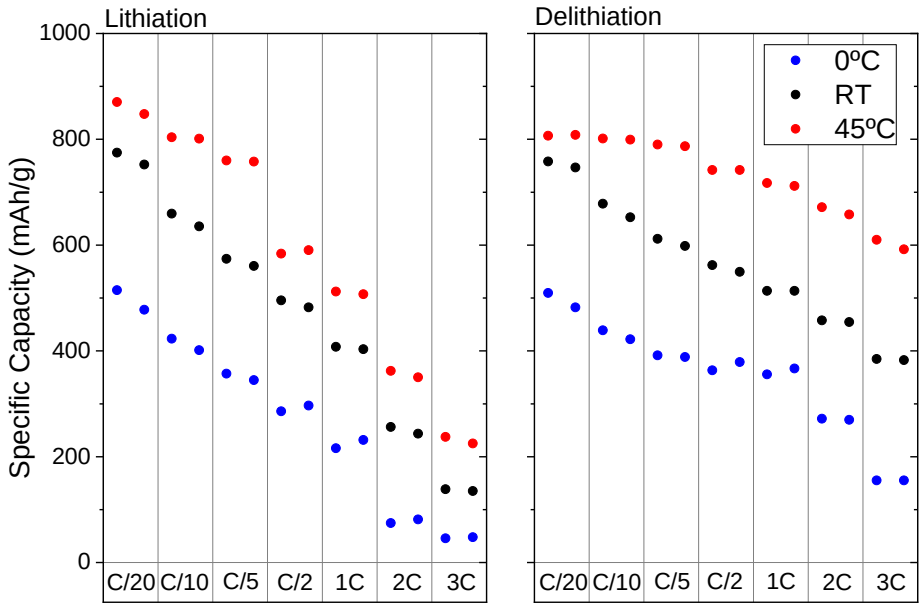

Figure 5.9: Specific capacities measured for the blended electrode in the three temperatures studied for different rates of lithiation and delithiation.

To gain understanding in the dynamics of each component in the blend and compare with the pure components, Figure 5.10 shows the differential capacity of the blended electrodes for the three different temperatures. The processes related to each of the components can be identified. The peaks of silicon and graphite are indicated in the figure with a letter corresponding to the process related i.e. lithiation stages for graphite and the A or B processes for silicon.

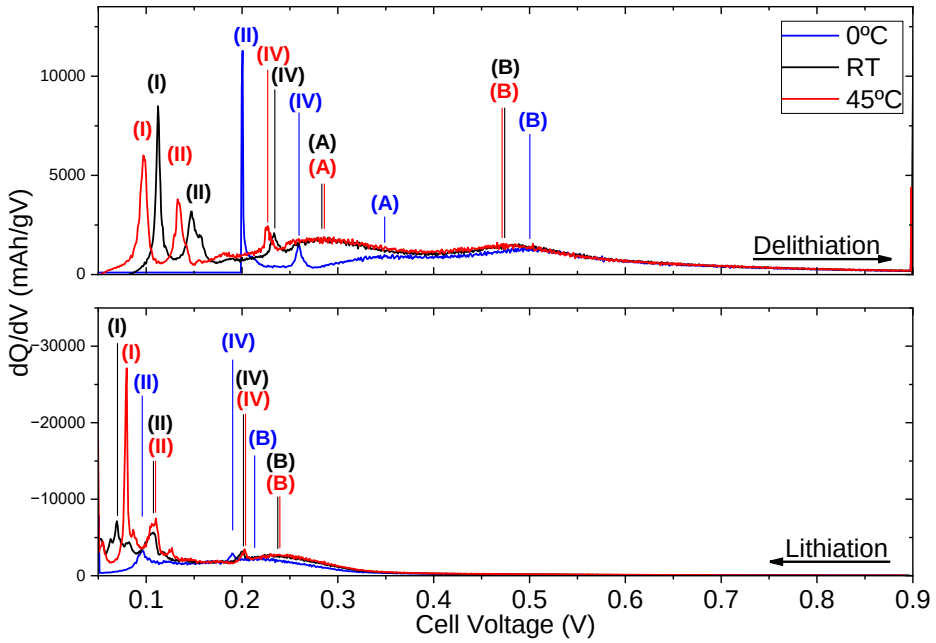

Figure 5.10: Differential specific capacity (dQ/dV) of the blended electrodes for the temperatures studied, 0ºC (blue lines), RT (black lines) and 45ºC (red lines) during delithiation (top) and lithiation (bottom). Above each peak is its assignment. The two peaks of silicon were labeled as A and B while the three peaks of graphite with I,II and IV, that denote the corresponding stages.

For all temperatures, the samples show the characteristics of both components with very clear sharp peaks due to graphite and two broader processes at higher voltages due to silicon. The potentials at which peaks are observed are included in Table 5.5, together with the values achieved for the components (see previous sections) as well as their calculated differences.

Table 5.5: Tables depicting the peak potentials as determined from the dQ/dV plots (Fig 5.10) for pure components and the blended electrode at the different temperatures tested. In the last column, the position difference of each peak between the blend and the pure electrode is written in parenthesis. "N.D." indicates non-distinguishable.

Temperature 0ºC	*Lithiation*			*Delithiation*		
	Silicon	*Graphite*	***Blend***	*Silicon*	*Graphite*	***Blend***
Graphite I	-	*0.05 V*	-	-	*0.126 V*	-
Graphite II	-	*0.088 V*	***0.096 (+0.008V)***	-	*0.168 V*	***0.200 (+0.032)***
Graphite IV	-	*0.168 V*	***0.190 (+0.022)***	-	*0.240 V*	***0.260 (+0.020)***
Silicon A	*0.05*	-	*N.D.*	*0.31*	-	***0.36 (+0.05)***
Silicon B	*0.22*	-	***0.21 (-0.01)***	*0.49*	-	***0.5 (+0.01)***

Temperature RT	*Lithiation*			*Delithiation*		
	Silicon	*Graphite*	***Blend***	*Silicon*	*Graphite*	***Blend***
Graphite I	-	*0.081 V*	***0.069 (-0.012)***	-	*0.098 V*	***0.112 (+0.014)***
Graphite II	-	*0.117 V*	***0.107 (-0.010)***	-	*0.139 V*	***0.146 (+0.007)***
Graphite IV	-	*0.205 V*	***0.2 (-0.05)***	-	*0.224 V*	***0.233 (+0.009)***
Silicon A	*0.08*	-	*N.D.*	*0.28*	-	***0.28 (+0)***
Silicon B	*0.23*	-	***0.23 (+0)***	*0.47*	-	***0.47 (+0)***

Temperature 45ºC	*Lithiation*			*Delithiation*		
	Silicon	*Graphite*	***Blend***	*Silicon*	*Graphite*	***Blend***
Graphite I	-	*0.083 V*	***0.080 (-0.003)***	-	*0.095 V*	***0.097 (+0.002)***
Graphite II	-	*0.115 V*	***0.108 (-0.007)***	-	*0.132 V*	***0.133 (+0.001)***
Graphite IV	-	*0.205 V*	***0.203 (-0.002)***	-	*0.222 V*	***0.227 (+0.005)***
Silicon A	*0.08*	-	*N.D.*	*0.28*	-	***0.28 (+0)***
Silicon B	*0.23*	-	***0.23 (+0)***	*0.47*	-	***0.47 (+0)***

For the ambient and high temperature, the peak voltages of the silicon processes seem to remain unaffected by the blending. For the case of graphite, a few mV decrease of the characteristic potentials is observed during lithiation and increase during delithiation. This would be in agreement with the introduction of silicon increasing the polarization of the graphite processes in the electrode. When compared in magnitude, the shift observed at RT is larger than the one at 45 ºC which is likely attributed to the faster kinetics of graphite at the higher temperature. Nevertheless, these aspects need

to be further investigated as the opposite trend (increase of potential for graphite processes for both lithiation and delithiation) is observed at 0°C. Interestingly lithiation's potential increase has also been reported at room temperature for electrodes containing 15% of Si nanopowder tested at similar rates. [13]The electrode formulation of that study though, differed significantly from the one used here (2% vs 10% carbon additive) as well as cycling protocol.

5.3.2 Decoupled blend study

To study the contribution of each material to the final blend, the decoupled blend three electrode cell was assembled with each of the two working electrodes containing only one of the blend components, with a ratio between them approaching the one of the true blended electrode described above. The active masses of the electrodes used were equal to 4.05mg and 1.40mg for graphite and silicon respectively, yielding a graphite:silicon mass ratio of 74:26 close to the 70:30 of the blended electrode. To test how representative of the true blend this electrode was, Figure 5.11 depicts the differential capacity measured for the coin cell with blended electrode and the decoupled blend cell, at C/20 and RT. Voltage vs capacity curve is also given in Figure SI 5.5. Despite the difficulties of this system, the cell reproduces the behaviour fairly well.

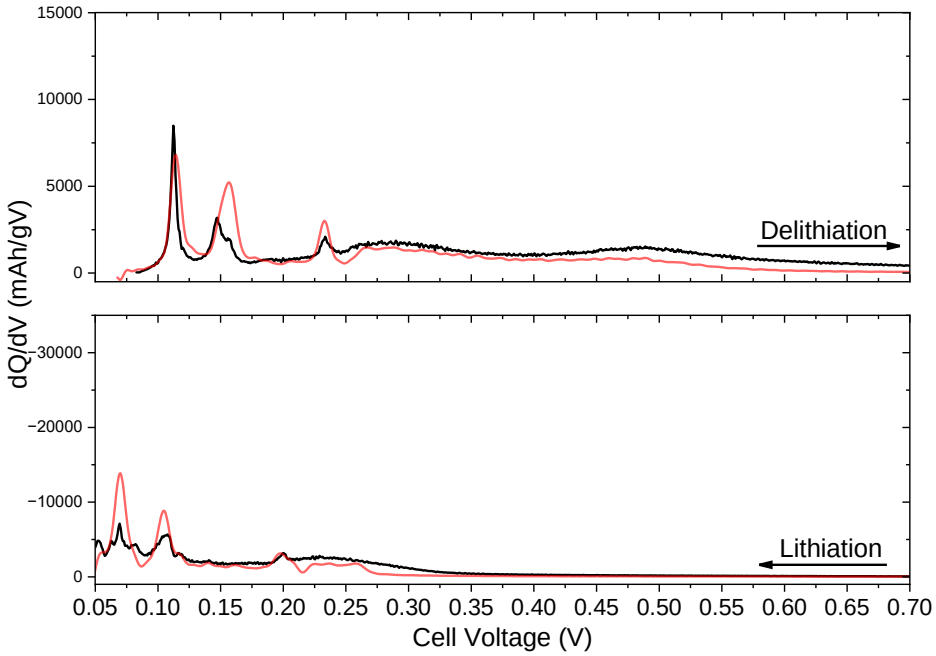

Figure 5.11: Differential specific capacity curves for the coin cell bearing the 30%wt. silicon – 70%wt. graphite blended electrode (black lines) and the decoupled blend with two working electrodes with mass ratios 26% silicon – 74% graphite. Both measurements are at a C/20 rate and at RT. Top graph shows the delithiation and bottom one the lithiation step. Decoupled blend data was smoothened for better visibility.

This cell configuration allows the measurement of the current going to each of the two working electrodes, allowing for the assessment of the electrochemical stress applied to each component and the identification of the voltage regions in which each of the materials act. Figure 5.12 shows the voltage of the cell as a function time for the decoupled blend. On the same x axis, a grey line represents the current flowing solely into graphite, while a thin dashed line indicates the total current delivered by the cell. The dark yellow and grey areas essentially represent the amount of charge stored or released by silicon and graphite respectively. The active masses of the electrodes are given in Table SI 5.2.

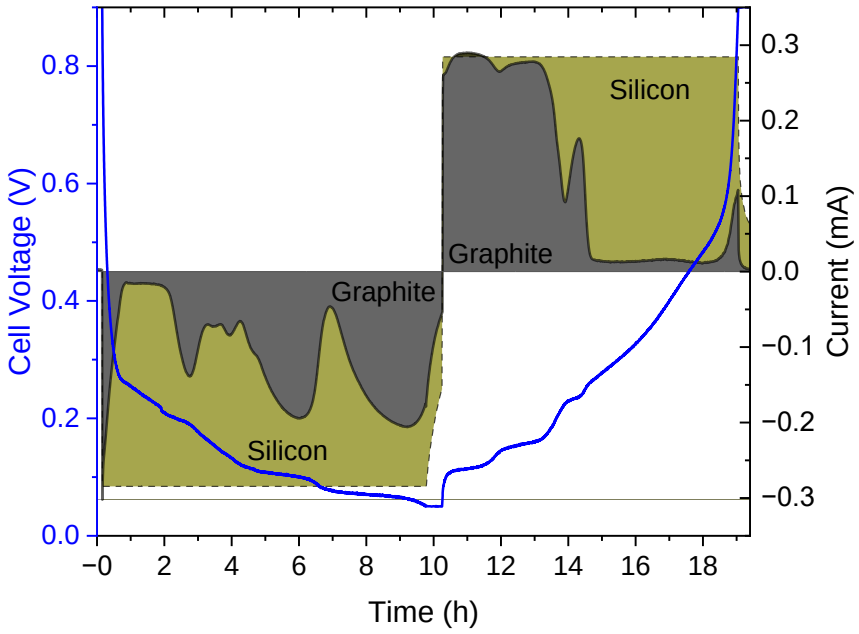

Figure 5.12: Voltage vs.time curve of the decoupled blend cell (blue line) and current flowing into graphite (grey line) at C/20 for the cell with 74:26 %wt ratio of graphite to silicon. Total cell current is also included (thin dashed line). The grey and dark yellow areas indicate the charge distribution between graphite and silicon respectively.

It is evident from the data depicted in Figure 5.12 that the charge distribution is significantly different between the lithiation and the delithiation steps, which is in contrast with the positive electrode blends studied in a previous work.[29] During lithiation, the activity of graphite exhibits three well defined peaks that align with the three plateaus that appear on the voltage curve. These plateaus, as discussed earlier, correspond to the formation of graphite stages, namely from lower to higher voltage they represent stage I, II and IV. As can be expected, the contribution of graphite increases significantly when the voltage of the cell coincides with the voltage of the plateaus. Two similar current maxima were witnessed at 0.1 V and 0.06 V, each corresponding to roughly 70% of the cell's total current On the other hand, the silicon, remains active throughout the lithiation process. Unlike graphite, its processes do not happen at well-defined potential values, and therefore its contribution fluctuates in

response to the state of graphite. This is shown by the fact that silicon's current reaches minima whenever the voltage corresponds to one of the graphite's processes. In contrast, during delithiation, the graphite current has a value equal to that going to the cell until the voltage reaches 0.2 V, meaning that the entirety of lithium extracted at this point comes from graphite. After this point, silicon becomes the active component. These results are in agreement with previously published data on blended silicon graphite electrodes of different formulations derived from operando synchrotron XRD [13], small and wide angle X-ray scattering (SAXS & WAXS). [14]Interestingly, this behaviour is also similar to the one reported for the decoupled blend cell using a thin film silicon electrode, in much lower weight fraction, instead of a composite one. [21]

By knowing the current going to each material and its capacity one can calculate the effective rate each material experiences at any point of the cycling process. Figure 5.13 shows the effective C-rate for both silicon and graphite for the cycle under discussion. The red dashed line indicates the nominal C-rate as calculated by the cell´s total capacity (taking 1C currents for graphite and silicon as 372 mA/g and 4000 mA/g respectively). Both materials´ C-rate fluctuate around this nominal value, but graphite exhibits much higher deviations. When silicon exhibits a rate peak of 0.065C (c.a. C/15) during delithiation, graphite reaches values up to 0.19 C (c.a. C/5) which is almost 4 times the programmed rate (0.05C or C/20). The overall fluctuation range depends on the capacity of a material included in a blend rather than its mass. In this case, even though silicon is in significant lower weight fraction than graphite, its capacity is larger and as such is less prone to C-rate fluctuations.

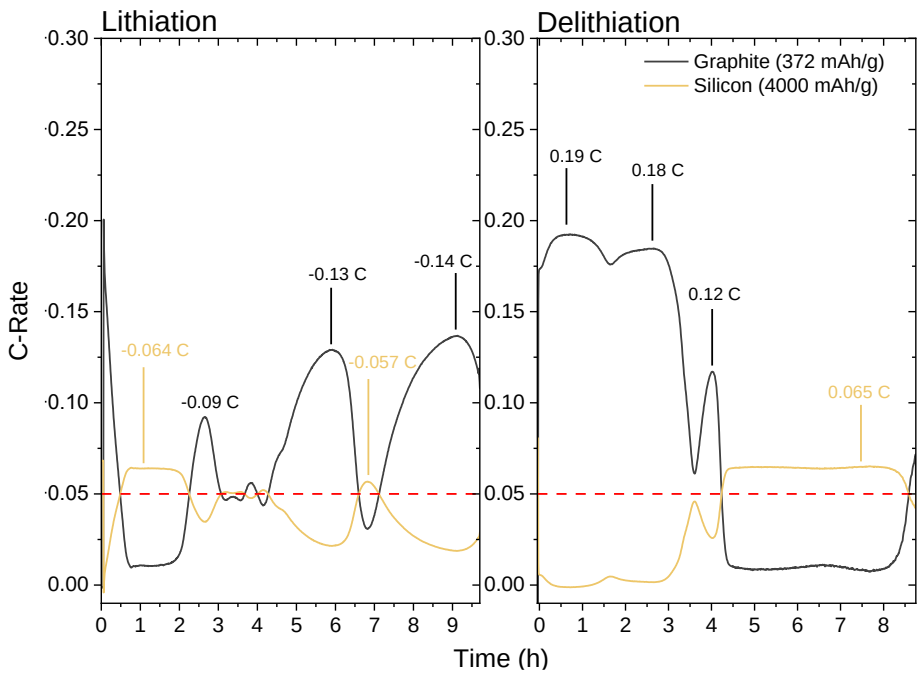

Figure 5.13: Calculated effective C-rate for both graphite (grey lines) and silicon (yellow lines) for the decoupled blend at C/20, with explicit values corresponding to maximum observed C-rates observed in both lithiation and delithiation. The red dashed line indicates the nominal C-rate of the cell.

During lithiation, and due to silicon´s peaks shifting towards lower potentials, a larger overlap between the two materials´ activities is seen. This overlap allows achieving peak C-rate values closer to the nominal C-rate (although with a larger variation observed for graphite). This indicates that the current is shared between both components, moderating each other's "electrochemical stress". On the other hand, during delithiation, the processes of graphite and silicon happen at significantly different potentials, resulting in less overlap. Consequently, graphite handles all of the cell's current in the beginning of the delithiation, which is clearly reflected in the calculated C=rate. This effective increase in C-rate is likely linked to the increase of the overpotential observed in the blended electrodes as seen earlier for the blended electrode coin cells (Table 5.5).

It should be noted that, as described in the experimental section, the assembly of the decoupled cell described in the previous paragraph was complex due to the fact that fabricating electrodes with pure silicon as active material is far from being trivial. This

raises a methodological question about whether the results obtained genuinely reflect the behavior of real blended electrodes. While indirectly this highlights the importance of electrode formulation, which is beyond the scope of this study but has been to be relevant in some positive electrode blend compositions [30], [31], it underscores the challenge of replicating the exact electrochemical environment and interactions present in true blended electrodes for this system. Therefore, in order to further advance in the understanding of this system, a three-electrode cell with a different configuration was assembled: pure graphite as one of the working electrodes and a silicon graphite blended electrode as the other. This cell will be referred to as SiGr:Gr cell while the one with pure working electrodes as Si:Gr. Even though the data obtained is expected to be more complex, the SiGr:Gr configuration minimizes the influence of the silicon electrode's quality.

Figure 5.14 below shows the voltage vs time curve for the SiGr:Gr cell. The blended electrode had the same silicon content as the ones used previously, however, since the setup is assembled with a pure graphite electrode, the overall silicon share of the whole cell reduced. The active mass of the cell was calculated to be 9% silicon. Interestingly, this is closer to the amount of silicon found in commercial cells. Table SI 5.2 includes the details of the electrodes used.

The lithiation steps observed for this decoupled SiGr:Gr cell are almost identical to those of the Si:Gr cell. As discussed earlier, during lithiation, the processes for both materials overlap, resulting in a more cooperative behaviour of the electrode. In this case, adding graphite to the silicon electrode is unlikely to substantially alter the current profile, except for lowering the current of the pure graphite electrode, as some of it will now be directed toward the graphite present in the blended electrode.

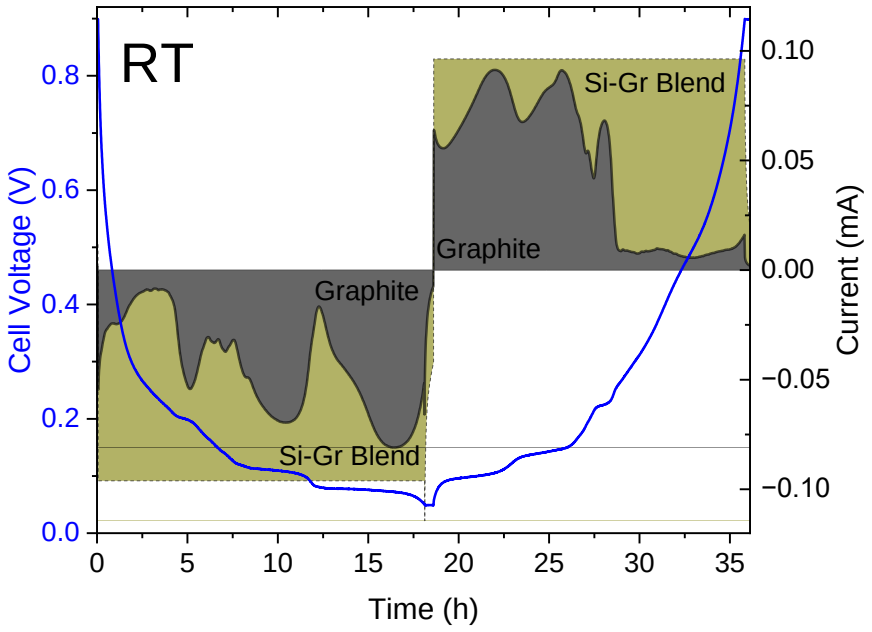

Figure 5.14: Voltage vs time curve of the decoupled blend cell (blue line) and current flowing into graphite (grey line) at C/20 for SiGr:Gr cell. Total cell current is also included (thin dashed line). The grey and dark yellow areas indicate the charge distribution between graphite and silicon-graphite electrodes respectively.

To further understand the dynamics in each electrode and the effect of blending, the pure graphite and silicon currents for this cell can be calculated. Such calculation requires the assumption that graphite performs identically in both electrodes, and therefore the specific currents of both types of graphite are considered equal:

$$(1) \qquad \frac{I_{Gr}^{pure}}{m_{Gr}^{pure}} = \frac{I_{Gr}^{blended}}{m_{Gr}^{blended}} \qquad or \qquad I_{Gr}^{blended} = \frac{m_{Gr}^{blended}}{m_{Gr}^{pure}} \; I_{Gr}^{pure}$$

Where I_{Gr}^{pure} , $I_{Gr}^{blended}$ are the currents and m_{Gr}^{pure}, $m_{Gr}^{blended}$ the mass of graphite in the pure graphite and the silicon graphite blended electrode respectively.

Furthermore, the total current of the cell is the sum of the currents of the two electrodes yielding eq.2:

$$(2) \qquad I_{cell} = I_{Gr}^{pure} + I_{SiGr}$$

and since the current of the blended electrode is equal to the sum of the currents of its active components:

$$(3) \qquad I_{cell} = I_{Gr}^{pure} + I_{Gr}^{blended} + I_{Si}^{blended}$$

Combining eq.3 and eq.1 yields:

$$(4) \qquad I_{cell} = I_{Gr}^{pure} + \frac{m_{Gr}^{blended}}{m_{Gr}^{pure}} I_{Gr}^{pure} + I_{Si}^{blended} = (1 + \frac{m_{Gr}^{blended}}{m_{Gr}^{pure}}) I_{Gr}^{pure} + I_{Si}^{blended}$$

And when one calculates $I_{Si}^{blended}$ and by applying eq. 3 can also calculate the total graphite current I_{Gr}.

Figure 5.15 shows the comparison of graphite current in the Si:Gr decoupled cell as compared to the SiGr:Gr one, calculated as described above. Note that at voltages above 0.3V during lithiation, due to the low activity of both components, the measurements bear significant error and do not provide valuable information. For better comparison two different Y-axis scales were used to account for the capacity difference of the two cells.

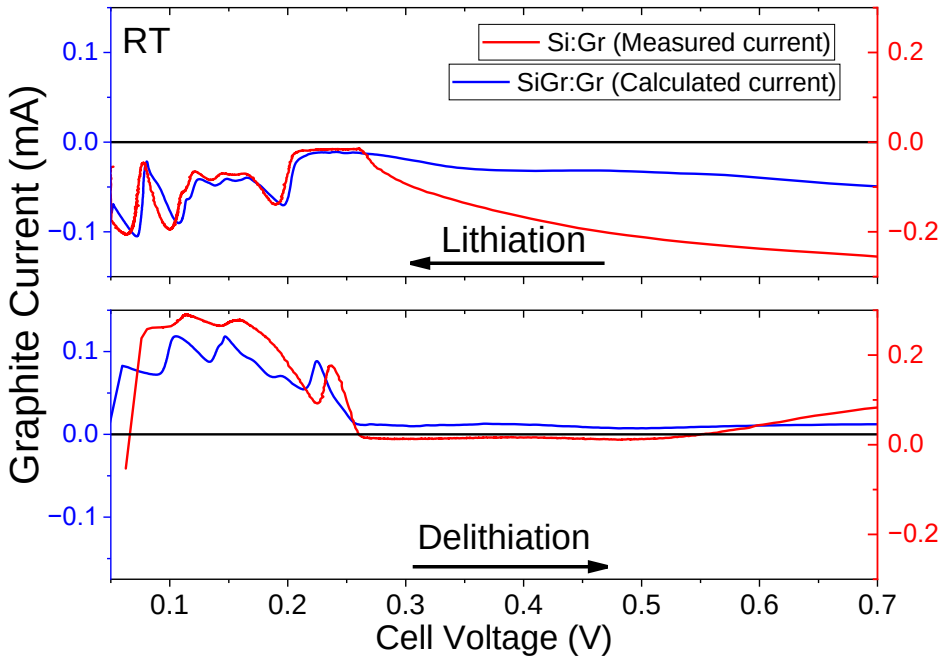

Figure 5.15: Comparison of graphite's current vs. voltage for two decoupled blend cells at C/20. Red line and Y-axis represent the Si:Gr cell and blue line and Y-Axis represent the SiGr:Gr cell).

For the lithiation step, in the range of 0.3 V to 0.05V (where most of the capacity is delivered), the two cells qualitatively show identical characteristics with 3 well defined peaks of the graphite stages, as discussed earlier. A slight shift towards lower potentials is witnessed for the Si:Gr cell. This can be explained by the higher silicon content of the Si:Gr cell (26% vs 9%), which leads to significantly higher C-rates experienced by the graphite and, as such, a slightly larger polarization. During the subsequent delithiation, the curves appear more distinct. In line with the hypothesis of higher polarization of graphite in the cell with the higher silicon content, the stage peaks of graphite appear at higher potentials in the cell that bears two pure electrodes. Interestingly, the cell with the blended electrode has the peaks of graphite more well defined which could also be an effect of the higher graphite content in this cell. One should not neglect the electrode's homogeneity impact that could affect the results but for this study, the C/20 rate was deemed slow enough to yield valuable results.

Next, the current of graphite in the SiGr:Gr cell was compared to that of silicon, yielding Figure 5.16.

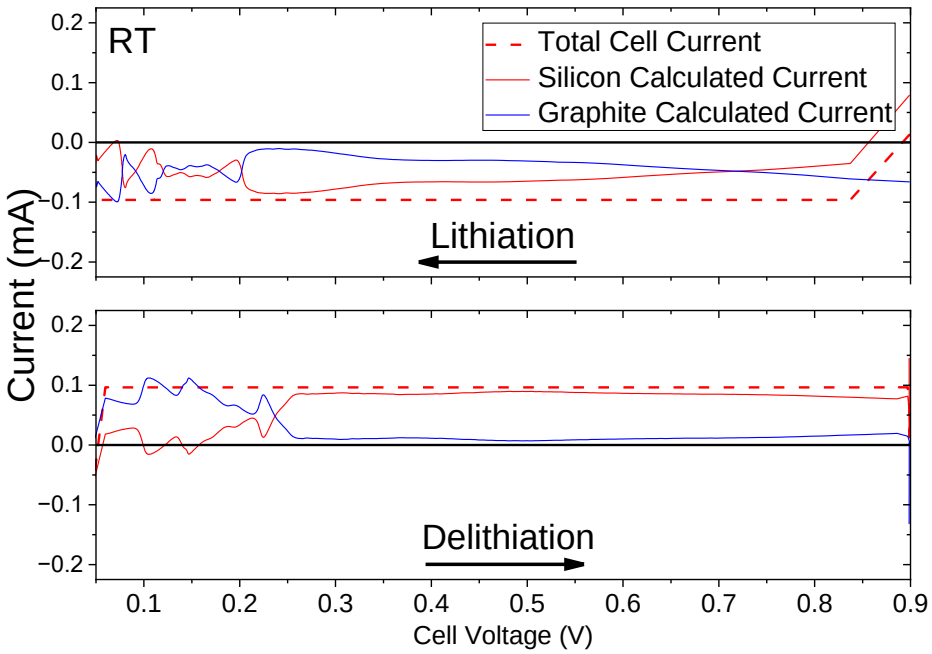

Figure 5.16: Calculated currents for silicon (red line) and graphite (blue line) of the SiGr:Gr cell at C/20. Dashed line is the cell's total current and the black line marks zero.

During lithiation, both materials are expected to act at the same time, as seen by the decoupled blend with the pure electrodes as well as the dQ/dV curves of the coin cells. The current of both silicon and graphite appears to be consistent with the discussion of Figure 5.12. An interesting phenomenon occurs though in the delithiation process as when comparing the individual component currents, they appear to slightly exceed their expected ranges. More precisely, the current of silicon appears to take negative values, while the graphite current exceeds the total current of the cell, which is not possible. The most plausible explanation is that the assumption that the two types of graphite in the cell (blended and pure) share the same specific current (eq. 1) does not apply. This would indicate that, even though both types of graphite act at the same potentials, one bears higher effective rate. Since the pure graphite's current and the cell's total current are directly measured, eq. 1 most likely overestimates the blended graphite's current. Through eq. 3 this inaccuracy also leads to the negative silicon current. It's interesting to note that this phenomenon is not observed during delithiation where both the blend's components are active. This might be linked to silicon worsening the electronic/ionic conductivity of the electrode. At the same time, another strength of this cell design becomes apparent, the ability to compare the activity of the same component in two different electrodes.

To deepen the understanding of both the system and the cell, this cell configuration bearing one blended working electrode and a pure graphite one, was also run in non-ambient temperatures, both low (0°C) and high (45°C). The cells had 18.5%wt and 20.2%wt of their active mass being silicon respectively. One has to take into account that in such systems, comprised of components with vastly different specific capacities, loading balancing is very challenging. If one tries to have electrodes of similar capacity loading, their mass loading is very different and vice-versa. The current profiles of the two experiments are presented in Figure 5.17. Even though they were measured at significantly different temperatures, both clearly show the peaks corresponding to graphite stages, appearing significantly sharper at 45°C, especially during delithiation. The peak potential values are compared in Table 5.6.

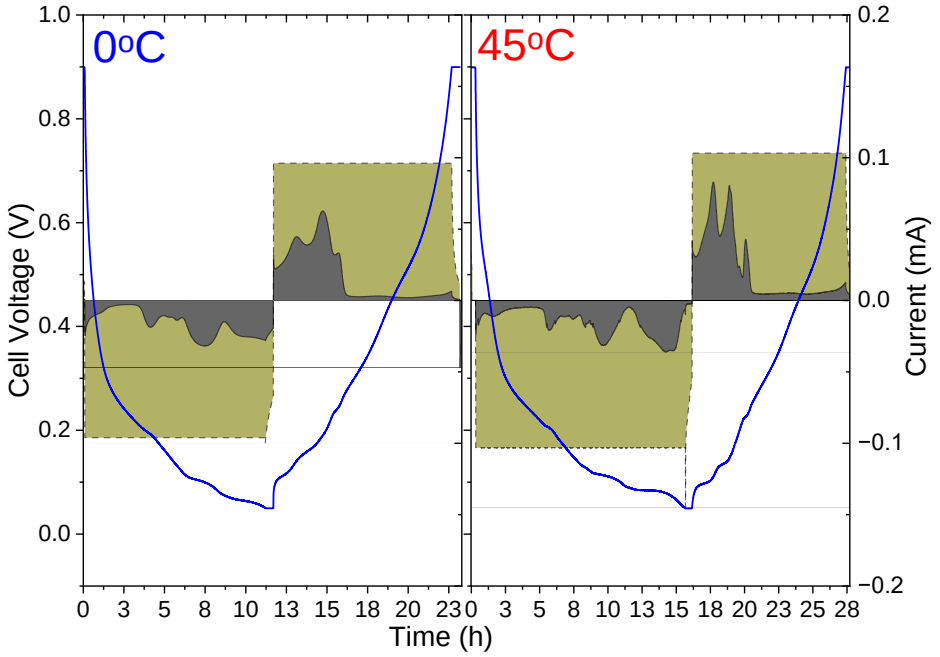

Figure 5.17: Voltage curve (blue line) and current going to graphite (grey line) of two decoupled blend cells at 0°C (left) and at 45°C (right) at C/20. Each cell had a silicon-graphite blended and a pure graphite working electrode. Total cell current is also included (thin dashed line). The grey and dark yellow areas indicate the charge exchanged with the graphite and silicon-graphite electrodes respectively.

Next, the individual component currents (I_{si} and I_{Gr}) were calculated. Figure 5.18 shows the currents for 0°C and 45°C. For both temperatures, similarly to the room temperature measurement, the delithiation currents where both materials act simultaneously, clearly show the stage peaks of graphite, which range between 0 and the cell's maximum current, as one would expect. During lithiation, where initially graphite is the mainly active component, it becomes apparent at both temperatures that the model fails to accurately calculate the current. This is indicated by the negative silicon current and the graphite current exceeding the total cell current. This is particularly true at 45°C. Further study needs to be conducted to fully understand this behaviour which might also be influenced by differences in capacity loading.

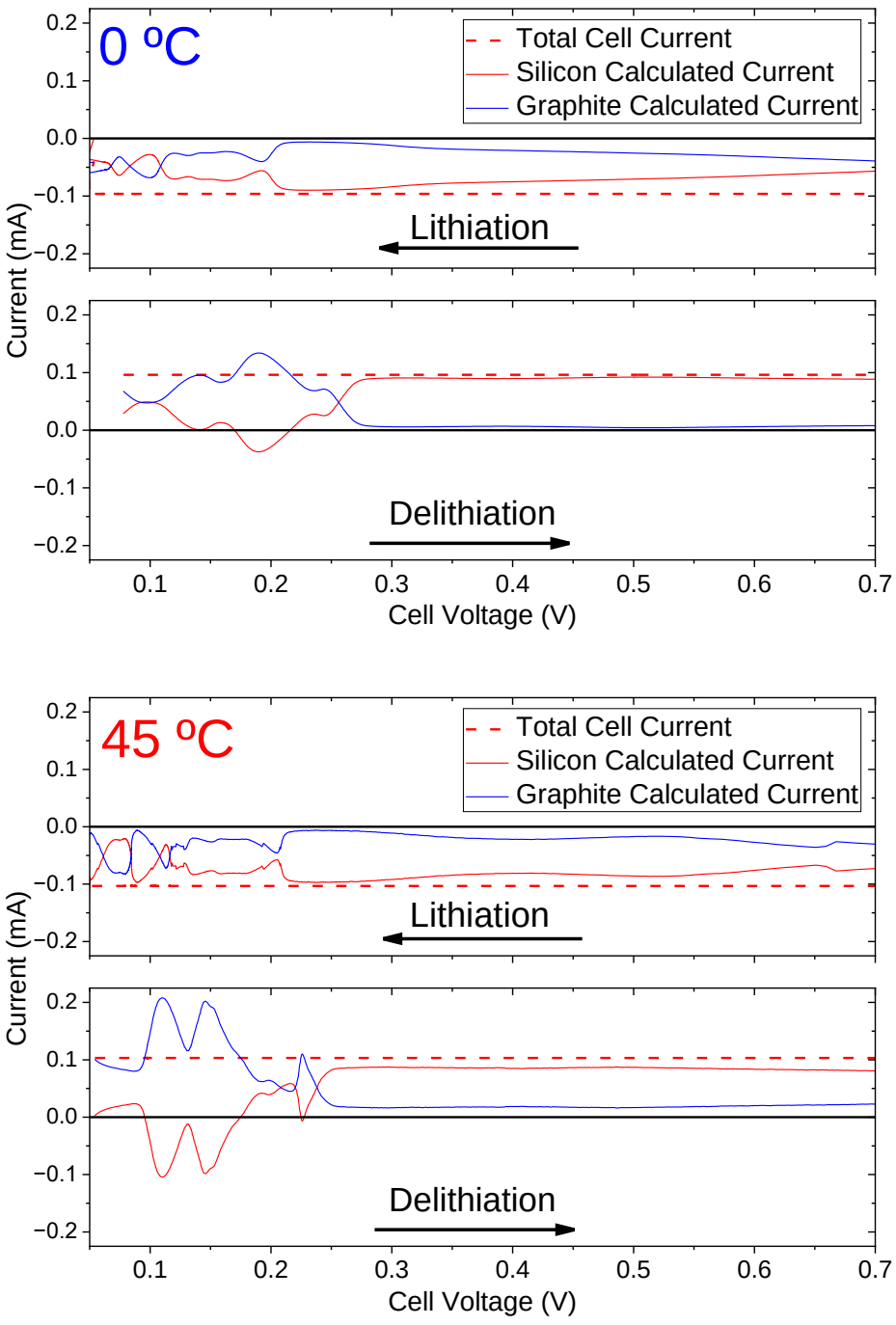

Figure 5.18: Calculated currents for silicon (red line) and graphite (blue line) for the decoupled blends measured at 0°C and 45°C.

Despite the challenges faced, one can still extract trustworthy information about the potential ranges at which graphite is active and bears higher effective rates. The aforementioned values for the 45°C, RT and 0°C measurements are presented in Table 5.6 where an excellent agreement between the values extracted from the SiGr:Gr decoupled blend setup and the coin cell with only the blended electrode.

Table 5.6: Comparison between the two cell setups : potential values for the different stages (I,II and IV) of graphite as well as their difference between lithiation and delithiation at three different temperatures (0°C ,RT and 45°C). Values for coin cells are taken from table 5.5)

	Temperature	0°C		RT		45°C	
		Coin Cell	Decoupled Blend	Coin Cell	Decoupled Blend	Coin Cell	Decoupled Blend
Graphite I	Lithiation	-	0.05	0.069	0.07	0.080	0.08
	Delithiation	-	0.14	0.112	0.10	0.097	0.11
Graphite II	Lithiation	0.096	0.10	0.107	0.11	0.108	0.11
	Delithiation	0.2	0.19	0.146	0.15	0.133	0.14
Graphite IV	Lithiation	0.190	0.19	0.20	0.20	0.203	0.21
	Delithiation	0.260	0.24	0.233	0.23	0.227	0.23

5.4 Conclusions

The results reported herein represent an extension of the study on composite blended electrodes a to cover silicon graphite blends, which are commonly used as negative electrodes in commercial Li-ion batteries. In particular, high silicon content (30% of the total active material mass) blends were studied, together with electrodes containing only the individual components, at different temperatures. Materials were studied in both coin cells as well as in a decoupled blend setup, allowing for the assessment of the

contribution of each individual component to the total cell current. Despite the difficulty to fabricate a pure silicon electrode, meaningful results were achieved.

The experiments using coin cells of both the blended and pure electrodes yield consistent results, with the blended electrode exhibiting feature of both its constituents and significant differences were observed between the lithiation and the delithiation steps. These are due to the different polarization in the redox processes related to each component and in full agreement with previously reported data. Tests done at non-ambient temperatures (0°C and 45°C) indicate that this behaviour is not significantly affected despite some changes in the potential at which graphite stages appear. Interestingly, at RT and 45°C, the capacity measured is significantly higher than the one calculated by a simple rule of mixtures even at relatively low rates (C/20).

The experiments in the decoupled cell enabled to assess the effective rate of each blend component, the behaviour of which is significantly different between charge and discharge in line with the results obtained in coin cells. Since silicon and graphite exhibit very different capacities, the effective C-rate of graphite can be significantly higher than the nominal rate, especially during the delithiation process.

Last, decoupled blend cells containing one blended and one pure working electrodes were assembled and the component specific currents were deconvoluted. Results indicate that graphite may behave differently when pure or blended with further investigation needed to assess these conclusions.

This study highlights the amount of information that can be obtained by the decoupled blends setup and revealed some aspects of the complexity that silicon graphite blends possess. The understanding of this complexity is important for the design of future blended negative electrodes, especially if higher fractions of silicon are required to achieve the demands of energy density.

5.5 Supporting Information

Table SI 5.1. Details of the electrodes characterized in this document: mass of active material, theoretical capacity, mass loading and capacity loading.

Coin Cell (Electrode ⌀ 14mm)	Mass of Active material (mg)	Capacity (mAh)	Mass Loading (mg/cm^2)	Capacity Loading (mAh/cm^2)
Graphite (0°C)	1.088	0.405	0.71	0.26
Graphite (RT)	1.21	0.450	0.79	0.29
Graphite (45°C)	1.808	0.673	1.17	0.44
Silicon (0°C)	0.848	3.392	0.55	2.20
Silicon (RT)	1.816	7.264	1.18	4.72
Silicon (45°C)	1.720	6.880	1.12	4.47
30%Si-Gr Blend (0°C)	2.672	3.902	1.74	2.54
30%Si-Gr Blend (RT)	3.440	5.023	2.23	3.26
30%Si-Gr Blend (45°C)	3.200	4.673	2.08	3.04

Table SI 5.2: Details of decoupled blend cells assembled in this work: active mass, capacity loading and total silicon content.

Decoupled blend Cell (Electrode ⌀ 9.5mm)	*Electrode*	*Active mass*	*Mass Loading (mg/cm^2)*	*Capacity Loading (mAh/cm^2)*	*Total silicon content (%wt.)*
Si-Gr (RT)	*Si*	*1.40mg*	*1.98*	*7.92*	*25.7*
	Gr	*4.05mg*	*5.71*	*2.10*	
SiGr-Gr (RT)	*Si-Gr blend*	*0.33mg Si 0.77mg Gr*	*1.55*	*2.26*	*8,9%*
	Gr	*2.60mg*	*3.67*	*1.34*	
SiGr-Gr (0°C)	*Si-Gr blend*	*0.35mg Si 0.82mg Gr*	*1.51*	*2.20*	*18.5%*
	Gr	*0.72g*	*1.02*	*0.37*	
SiGr-Gr (45°C)	*Si-Gr blend*	*0.42mg Si 0.98mg Gr*	*1.97*	*2.87*	*20.2%*
	Gr	*0.68mg*	*0.96*	*0.35*	

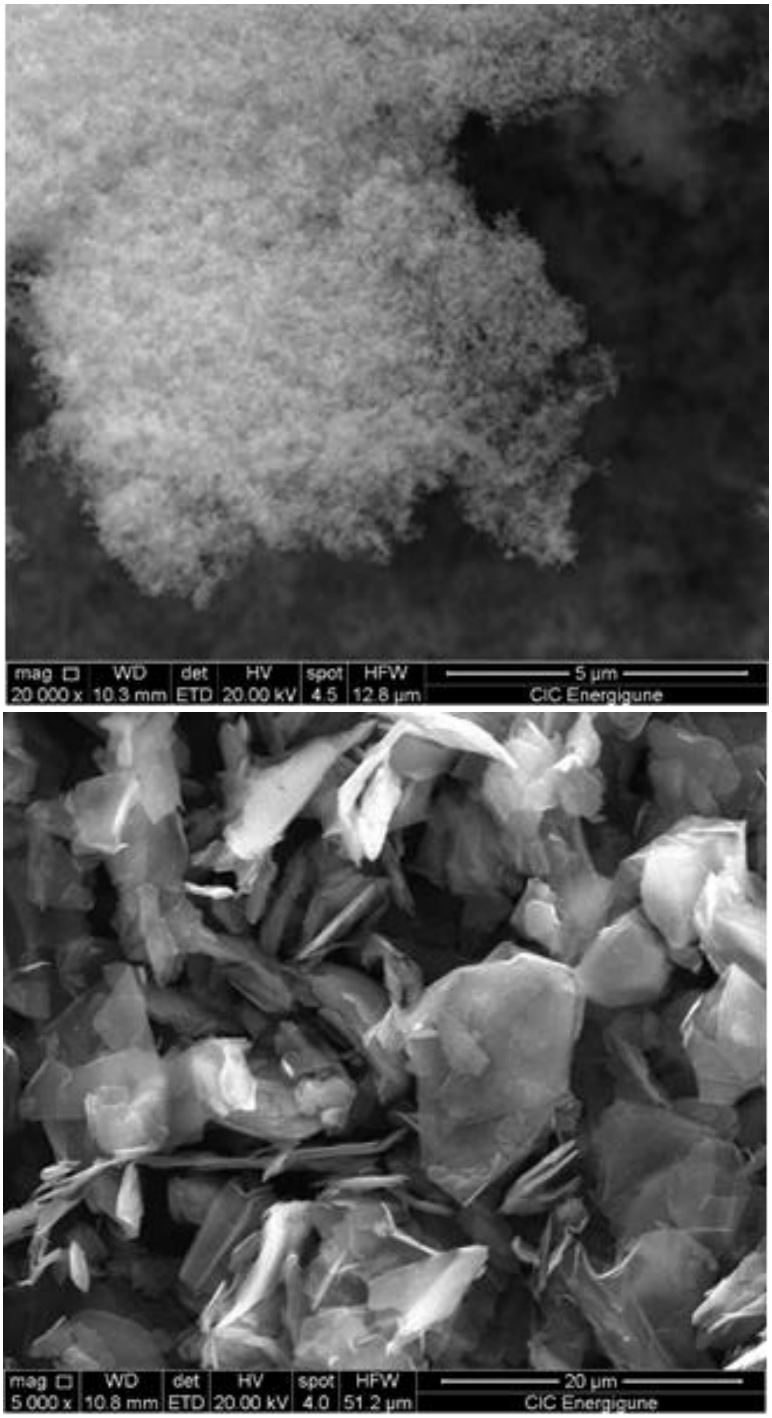

Figure SI 5.1: Typical SEM image of silicon nanoparticles (top) and graphite flakes (bottom) used in the study.

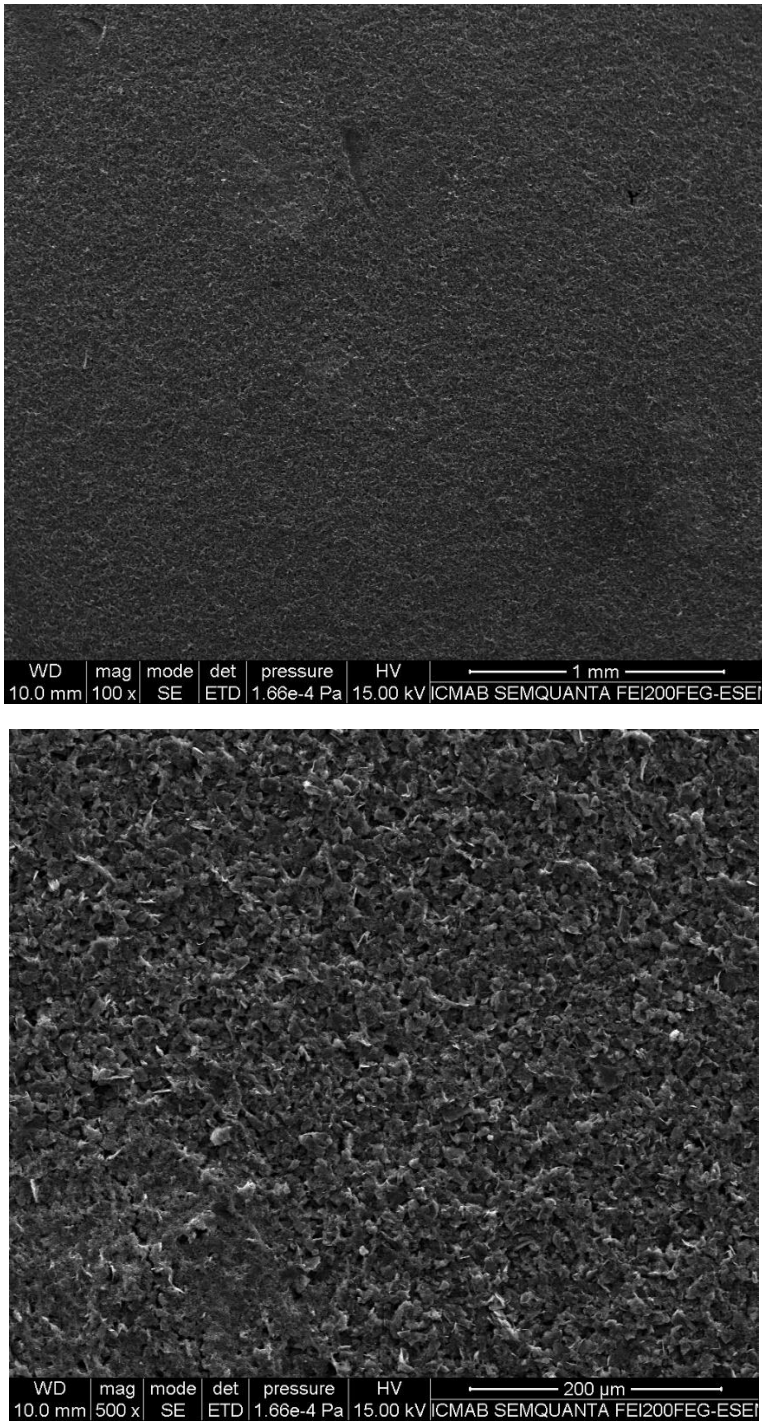

Figure SI 5.2: Typical SEM images in two different magnifications for the graphite electrodes.

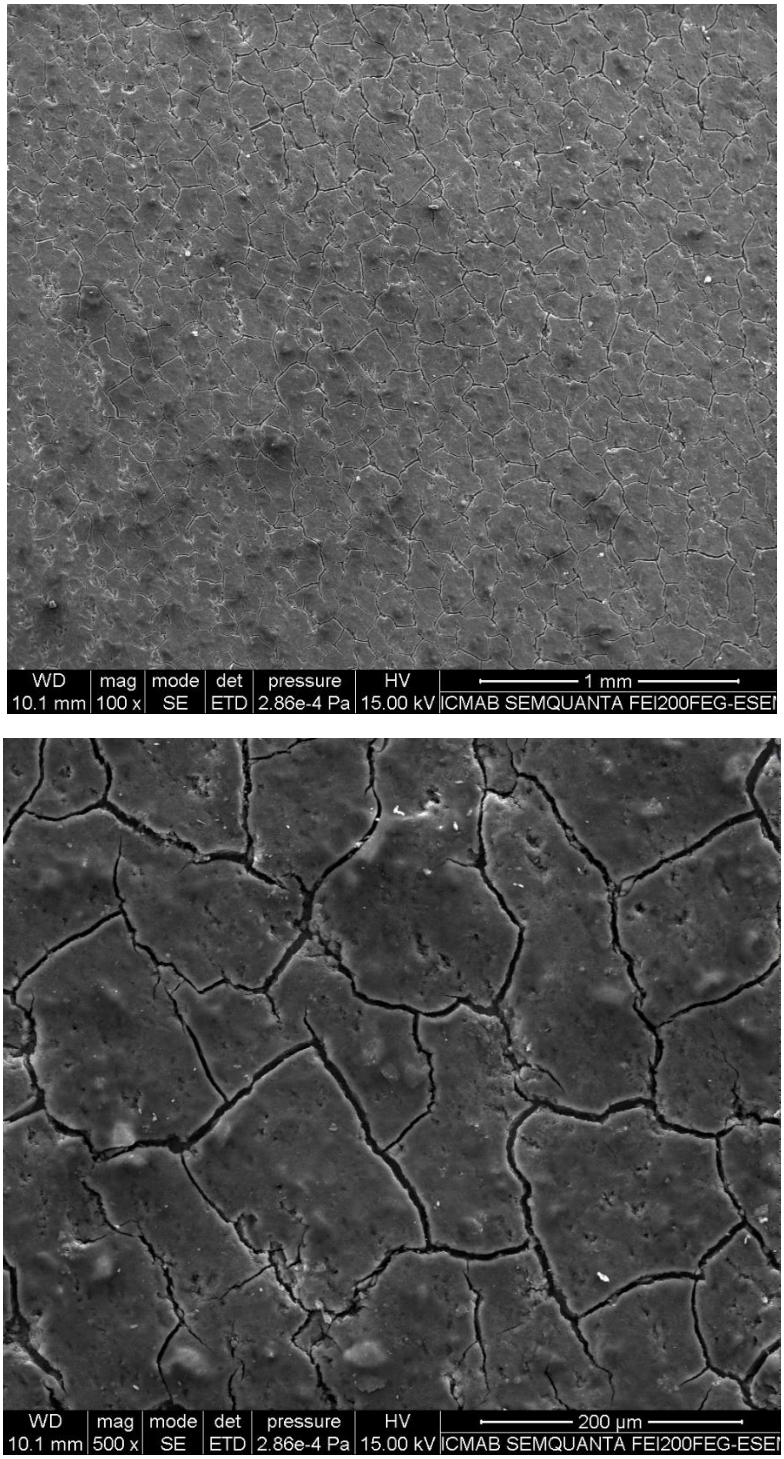

Figure SI 5.3: Typical SEM images in two different magnifications for the silicon electrodes.

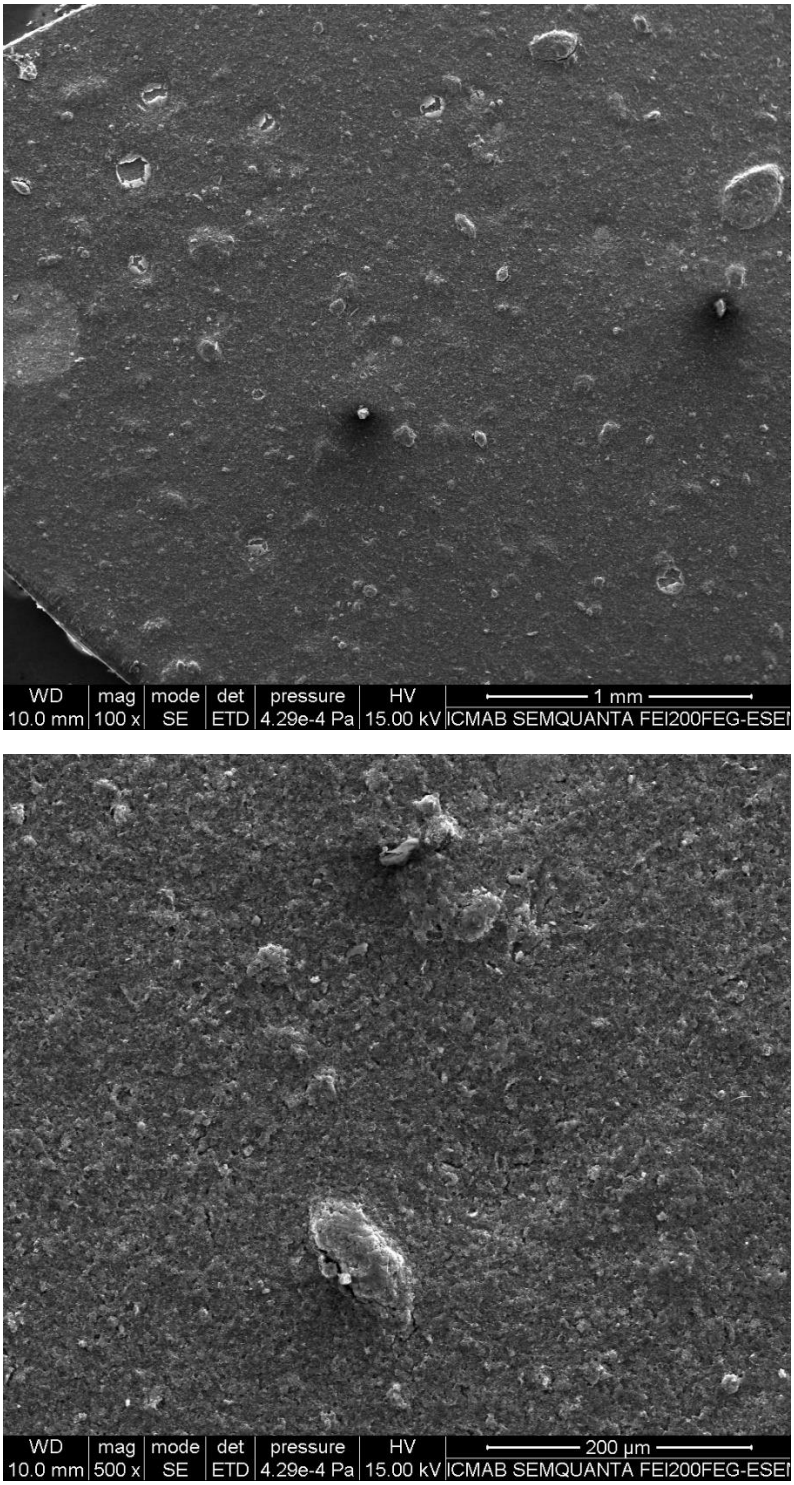

Figure SI 5.4: Typical SEM images in two different magnifications for the silicon graphite blended electrodes.

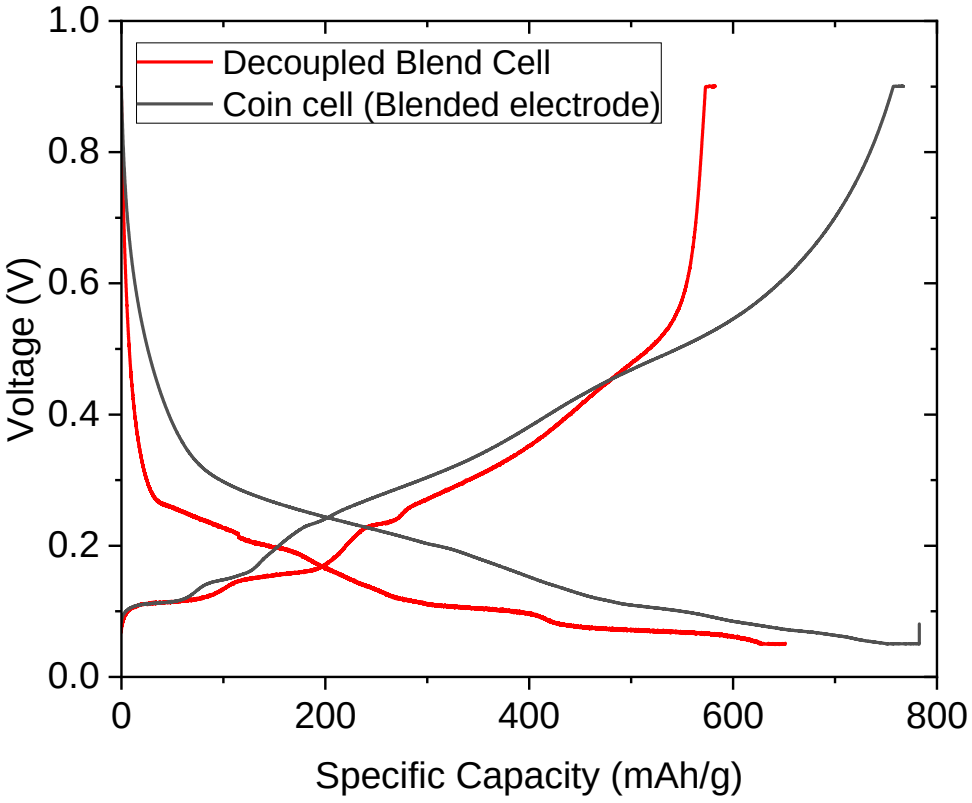

Figure SI 5.5: Comparison of voltage vs capacity curves for decoupled blend and coin cell with blended silicon graphite electrode.

References

[1] K. Feng et al., "Silicon-Based Anodes for Lithium-Ion Batteries: From Fundamentals to Practical Applications," Feb. 22, 2018, Wiley-VCH Verlag. doi: 10.1002/smll.201702737.

[2] Y. Jin, B. Zhu, Z. Lu, N. Liu, and J. Zhu, "Challenges and recent progress in the development of Si anodes for lithium-ion battery," Adv Energy Mater, vol. 7, no. 23, Dec. 2017, doi: 10.1002/aenm.201700715.

[3] S. Chae, S. H. Choi, N. Kim, J. Sung, and J. Cho, "Integration of Graphite and Silicon Anodes for the Commercialization of High-Energy Lithium-Ion Batteries," Jan. 02, 2020, Wiley-VCH Verlag. doi: 10.1002/anie.201902085.

[4] U. Kasavajjula, C. Wang, and A. J. Appleby, "Nano- and bulk-silicon-based insertion anodes for lithium-ion secondary cells," Jan. 01, 2007. doi: 10.1016/j.jpowsour.2006.09.084.

[5] H. Takezawa, S. Ito, H. Yoshizawa, and T. Abe, "Structural stabilization on SiOx film anode with large areal capacity for enhanced cyclability in lithium-ion batteries," J Power Sources, vol. 324, pp. 45–51, Aug. 2016, doi: 10.1016/j.jpowsour.2016.05.061.

[6] H. Wu and Y. Cui, "Designing nanostructured Si anodes for high energy lithium ion batteries," Oct. 2012. doi: 10.1016/j.nantod.2012.08.004.

[7] L. Martin, H. Martinez, M. Ulldemolins, B. Pecquenard, and F. Le Cras, "Evolution of the Si electrode/electrolyte interface in lithium batteries characterized by XPS and AFM techniques: The influence of vinylene carbonate additive," Solid State Ion, vol. 215, pp. 36–44, May 2012, doi: 10.1016/j.ssi.2012.03.042.

[8] M. Winter and J. O. Besenhard, "'Lithiated Carbons,'" in HANDBOOK OF BATTERY MATERIALS, 2ND EDITION, pp. 433–478.

[9] M. N. Obrovac and V. L. Chevrier, "Alloy negative electrodes for Li-ion batteries," Dec. 10, 2014, American Chemical Society. doi: 10.1021/cr500207g.

[10] M. N. Obrovac and L. J. Krause, "Reversible Cycling of Crystalline Silicon Powder," J Electrochem Soc, vol. 154, no. 2, p. A103, 2007, doi: 10.1149/1.2402112.

[11] J. Li and J. R. Dahn, "An In Situ X-Ray Diffraction Study of the Reaction of Li with Crystalline Si," J Electrochem Soc, vol. 154, no. 3, p. A156, 2007, doi: 10.1149/1.2409862.

[12] M. T. McDowell, S. W. Lee, W. D. Nix, and Y. Cui, "25th anniversary article: Understanding the lithiation of silicon and other alloying anodes for lithium-ion batteries," Sep. 2013. doi: 10.1002/adma.201301795.

[13] K. P. C. Yao, J. S. Okasinski, K. Kalaga, J. D. Almer, and D. P. Abraham, "Operando Quantification of (De)Lithiation Behavior of Silicon–Graphite Blended Electrodes for Lithium-Ion Batteries," Adv Energy Mater, vol. 9, no. 8, Feb. 2019, doi: 10.1002/aenm.201803380.

[14] C. L. Berhaut et al., "Multiscale Multiphase Lithiation and Delithiation Mechanisms in a Composite Electrode Unraveled by Simultaneous Operando Small-Angle and Wide-Angle X-Ray Scattering," ACS Nano, vol. 13, no. 10, pp. 11538–11551, Oct. 2019, doi: 10.1021/acsnano.9b05055.

[15] A. J. Smith, S. R. Smith, T. Byrne, J. C. Burns, and J. R. Dahn, " Synergies in Blended LiMn 2 O 4 and Li[Ni 1/3 Mn 1/3 Co 1/3]O 2 Positive Electrodes ," J Electrochem Soc, vol. 159, no. 10, pp. A1696–A1701, 2012, doi: 10.1149/2.056210jes.

[16] H. Y. Tran, C. Täubert, and M. Wohlfahrt-Mehrens, "Influence of the technical process parameters on structural, mechanical and electrochemical properties of LiNi0.8Co0.15Al0.05O2 based electrodes - A review," Dec. 01, 2014, Elsevier Ltd. doi: 10.1016/j.progsolidstchem.2014.04.006.

[17] C. Heubner, U. Langklotz, and A. Michaelis, "Theoretical optimization of electrode design parameters of Si based anodes for lithium-ion batteries," J Energy Storage, vol. 15, pp. 181–190, Feb. 2018, doi: 10.1016/j.est.2017.11.009.

[18] M. Casas-Cabanas, A. Ponrouch, and M. R. Palacín, "Blended Positive Electrodes for Li-Ion Batteries: From Empiricism to Rational Design," Jan. 01, 2021, John Wiley and Sons Inc. doi: 10.1002/ijch.202000099.

[19] D. Chatzogiannakis et al., "Towards understanding the functional mechanism and synergistic effects of LiMn2O4 - LiNi0.5Mn0.3Co0.2O2 blended positive electrodes for Lithium-ion batteries," J Power Sources, vol. 591, p. 233804, 2024, doi: https://doi.org/10.1016/j.jpowsour.2023.233804.

[20] K. Richter et al., "Low-Temperature Charging and Aging Mechanisms of Si/C Composite Anodes in Li-Ion Batteries: An Operando Neutron Scattering Study," ChemSusChem, vol. 13, no. 3, pp. 529–538, Feb. 2020, doi: 10.1002/cssc.201903139.

[21] C. Heubner, T. Liebmann, O. Lohrberg, S. Cangaz, S. Maletti, and A. Michaelis, "Understanding Component-Specific Contributions and Internal Dynamics in Silicon/Graphite Blended Electrodes for High-Energy Lithium-Ion Batteries," Batter Supercaps, vol. 5, no. 1, Jan. 2022, doi: 10.1002/batt.202100182.

[22] C. Heubner, T. Liebmann, C. Lämmel, M. Schneider, and A. Michaelis, "Internal dynamics of blended Li-insertion electrodes," J Energy Storage, vol. 20, pp. 101–108, Dec. 2018, doi: 10.1016/j.est.2018.09.003.

[23] M. Cabello, E. Gucciardi, A. Herrán, D. Carriazo, A. Villaverde, and T. Rojo, "Towards a High-Power Si@graphite Anode for Lithium Ion Batteries through a Wet Ball Milling Process," Molecules, vol. 25, no. 11, Jun. 2020, doi: 10.3390/molecules25112494.

[24] N. P. W. Pieczonka et al., "Lithium Polyacrylate (LiPAA) as an Advanced Binder and a Passivating Agent for High-Voltage Li-Ion Batteries," Adv Energy Mater, vol. 5, no. 23, Dec. 2015, doi: 10.1002/aenm.201501008.

[25] G. Park, N. Gunawardhana, H. Nakamura, Y. S. Lee, and M. Yoshio, "The study of electrochemical properties and lithium deposition of graphite at low temperature," J Power Sources, vol. 199, pp. 293–299, Feb. 2012, doi: 10.1016/j.jpowsour.2011.10.058.

[26] M. D. Levi, C. Wang, J. S. Gnanaraj, and D. Aurbach, "Electrochemical behavior of graphite anode at elevated temperatures in organic carbonate solutions," in Journal of Power Sources, Jun. 2003, pp. 538–542. doi: 10.1016/S0378-7753(03)00279-9.

[27] K. Xu, "Nonaqueous liquid electrolytes for lithium-based rechargeable batteries," Chem Rev, vol. 104, no. 10, pp. 4303–4417, Oct. 2004, doi: 10.1021/cr030203g.

[28] M. J. Loveridge et al., "Towards High Capacity Li-ion Batteries Based on Silicon-Graphene Composite Anodes and Sub-micron V-doped LiFePO 4 Cathodes," Sci Rep, vol. 6, Nov. 2016, doi: 10.1038/srep37787.

[29] D. Chatzogiannakis, V. Arszelewska, P. E. Cabelguen, F. Fauth, M. Casas-Cabanas, and M. R. Palacin, "Understanding charge transfer dynamics in blended positive electrodes for Li-ion batteries," Energy Storage Mater, vol. 69, May 2024, doi: 10.1016/j.ensm.2024.103414.

[30] D. Mazouzi et al., "Critical roles of binders and formulation at multiscales of silicon-based composite electrodes," Apr. 15, 2015, Elsevier. doi: 10.1016/j.jpowsour.2015.01.140.

[31] N. Besnard et al., "Multiscale Morphological and Electrical Characterization of Charge Transport Limitations to the Power Performance of Positive Electrode Blends for Lithium-Ion Batteries," Adv Energy Mater, vol. 7, no. 8, Apr. 2017, doi: 10.1002/aenm.201602239.

6. General Discussion

6.1 Global Approach

In the course of this thesis a number of positive electrode materials were tested, from currently commercial to promising next-generation candidates. An effort was made to understand the behaviour of blended electrodes, with the aim of identifying trends that could that could be useful in the design of future blends, even if they do not contain the same compounds investigated herein. Materials were chosen with the purpose of representing the largest range of properties found in commercial cells, including some close-to-market or under development options. In addition to that, the methodology developed and applied to the study of blended positive electrodes was extended to the negative side, in particular to blends of silicon and graphite (currently commercially used with few percents of silicon). Since the trend is to increase the amount of silicon in the electrodes, the results achieved provide valuable inputs for further development. Moreover, these methodologies could as well be extrapolated beyond the lithium ion technology.

This study builds on existing state-of-the art knowledge in electrode materials with the aim to understand and broaden the knowledge about internal processes in blended electrodes and aid the transition from an empirical to a rational design. Previous studies have shown that NMC-type materials offer high capacities and satisfactory kinetics but are prone to thermal instability and capacity fading over time. Conversely, LFP is valued for its exceptional stability and safety, though it provides a lower energy density —a crucial trade-off for applications like electric vehicles. The LMO spinel structure demonstrates excellent kinetics and good thermal stability, both highly desirable qualities, but suffers from low energy density and is notably susceptible to capacity fading due to manganese dissolution. LFMP improves upon the LFP structure by partially replacing iron with manganese, which increases the overall energy density while preserving the safety and stability characteristics.

Finally, LRO represents a family of promising next-generation materials, showing properties similar to NMC with higher energy densities and aiming to reduce or even eliminate cobalt due to environmental and ethical concerns. However, LRO's main

limitations are poor thermal stability, low first-cycle coulombic efficiency, and cycling-induced voltage fading.

Blending could a priori affect a number of different aspects:

i) *by applying simple **geometric** principles, combining two materials with different particle sizes—even of the same chemical composition—can directly impact packing density, thereby increasing the energy density of the electrode.*

ii) ***Chemically**, in the case of NMC-LMO blends, it has been proposed that NMC can act as a proton scavenger altering the pH around LMO as such protecting it from HF attack formed by the hydrolysis of $LiPF_6$ and as such limit the acid-mediated manganese dissolution of LMO, improving its cycle life.*

iii) ***Electrochemically**, as the potential vs. capacity profile of the blend will depend on that of the components, so that some aspects can be tailored by design to help with state of charge (SoC) estimation, which is relevant for the battery management system (BMS)*

iv) *In terms of **kinetics**, a phenomenon known as the "buffer effect" has been observed in blended electrodes, where there is an internal redistribution of lithium between components after a high-current pulse. This represents a type of synergistic interaction between the two materials the extent of which is related to the difference in kinetics between them for a given SoC.*

v) *The **thermal behavior** will also be impacted, even when batteries are at rest, due to the difference in entropy coefficients between components. Thus, temperature changes induce exchanges of lithium which may even negatively affect cycle life if frequent and of a significant magnitude.*

6.2 Methodology

To carry out the measurements, the decoupled blend three electrode cell setup was adapted from the works of Heubner et al. [1]allowing to decouple the electrochemical

activity the blend's components. The connection of the cell was slightly modified by replacing the ammeter they used with a potentiostat channel, as seen schematically below.

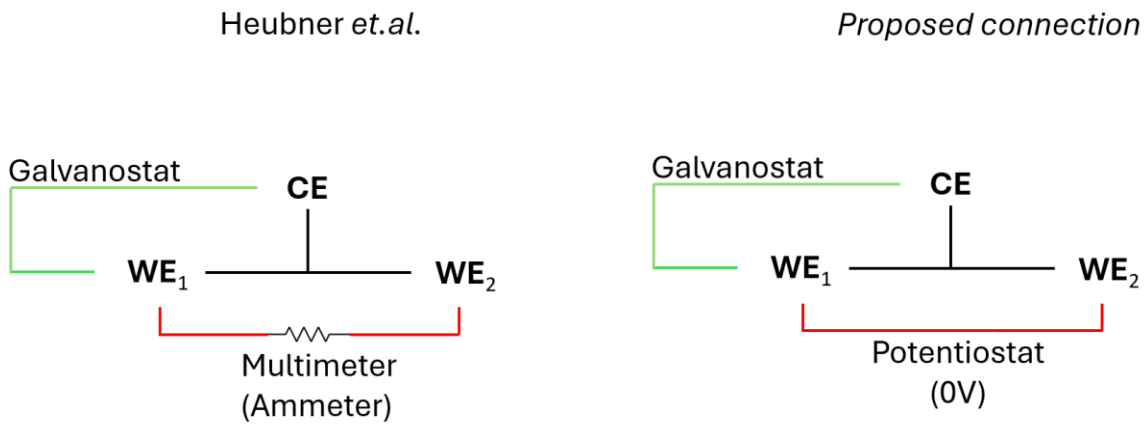

Figure 6.1: (left) Previously reported connection of decoupled cell and (right) proposed connection of the same cell, as used in this work.

In the left configuration in Figure 6.1, the shunt resistor will introduce a current-dependent voltage drop according to Ohm's law which could potentially influence the behaviour of the system. This voltage drop, including any caused by connection resistance, is commonly referred to as "burden voltage". In the method developed within this work (right), the shorting of the two working electrodes is done "actively", which would ideally produce more accurate results. To that purpose, two channels of the same instrument (Biologic VMP-3) were used, which are not fully isolated with each other and as such an error is introduced due to a leakage current between WE_2 and CE. For the setup used in this study, an equivalent resistance of 200kΩ between WE_2 and CE was measured. The validity of the setup was tested by replacing the potentiostat with a fully isolated instrument (Keithley 2400 SMU) and obtained similar results.

The second core technique in this work is operando experiments, primarily using synchrotron XRD. This approach enables parallelization of electrochemical and structural characterization, allowing the results to be mutually validated. This was especially important to assess the representativity of the results since the decoupled

blend setup lacks direct contact of the two materials. Within this framework, experimental parameters at the ALBA synchrotron (MSPD beamline) were carefully optimized to adjust the measurement time scale and reduce beam-related effects, which can be significant and result in an inhibition of the electrochemical reactions thus biasing the results achieved.[2], [3] These effects are influenced by photon energy, with higher-energy photons exerting less impact on the cells (as seen in Chapter 2) – consistent with absorption coefficients. To further mitigate these effects, in Chapter 2 cells were continuously oscillated during measurements to increase the exposure area and reduce the areal dose.

6.3 Investigation of internal dynamics in blended electrodes

One of the most relevant aspects of this work concerns the study of the effective rates in blend components, which can be very different from the cell's nominal rate. This effective rate is primarily determined by the potential vs. capacity profiles of both materials, which will be different depending on SoC. This observation relies in data included in both published works (Chapter 2 and 3) and supported by previous communications [4]. The influence can be deduced from the comparison of blends containing four representative materials with very different profiles namely: NMC (sloping profile), LFP (one plateau), LMO (two plateaus at very close potentials), LFMP (two plateaus at significantly different potentials).

In Chapter 2, employing the decoupled cell setup with all possible material pairs, the effective current in each component showed notable fluctuations. Depending on the composition and the state of charge (SoC), this current could match the cell total current or even drop to zero. This would occur when the cell voltage aligns with the reaction potential of one component with the other not having activity at that voltage, and is an important aspect to be taken into consideration when designing blend components for an application. Chapter 3 exemplifies how these values can also be modified by the relative amount of blend components, and showcases that any rate-related effect on a

material will be exacerbated for blends, as proved by synchrotron operando XRD and XAS.

This is also evident in Chapter 5 where the study was extended to the negative electrode, in this case with materials exhibiting significantly different capacities. Indeed, a 30% mass of silicon leads the graphite to experience effective rates up to 4x the cell nominal one while the effective rate for silicon increased only from 0.05C to 0.065C. If we assume that, for certain SoC, the entire current goes to one single component, then the effective rate of this component, here understood as the "electrochemical stress" experienced, will highly depend on its capacity rather than its mass. This means that a low mass fraction of a component with a low specific capacity will experience a very significant increase in its effective rate. Therefore, to balance rates in a blend, the component with the smaller weight fraction should ideally exhibit a higher specific capacity. This is especially relevant for the silicon graphite case, as reported in Chapter 5, as silicon has roughly 10 times the specific capacity of graphite. Another aspect that has been highlighted in Chapter 5 is that it becomes increasingly difficult to decouple the electrochemical performance of the components when electrode engineering plays a critical role, as in the case of pure or blended silicon electrodes. Additionally, when polarization is asymmetric between charge and discharge, the current distribution between components can vary significantly between oxidation and reduction, making it difficult to determine the optimal blend formulation.

Finally, blending with commercial delithiated materials is introduced here as an effective strategy to address the low initial coulombic efficiency of LRO. Instead of storing lithium that cannot be reincorporated into LRO after the first delithiation in the negative electrode, the approach stores this lithium within a delithiated material in the positive electrode, keeping it active and available for subsequent cycles. The choice of delithiated material should consider a reaction voltage lower than that of LRO to enhance stability during electrode preparation and storage, and an optimal amount to achieve near 100% coulombic efficiency. Preliminary operando experiments suggest a difference in the reaction mechanism of LRO that needs to be further studied. Thermal

characterization of blended electrodes soaked with electrolyte indicate an improved thermal stability.

6.4 Perspectives for further research

Cells used in everyday life, and especially the ones part of electric vehicles experience discharges far from constant current. High current pulses will induce a different polarization in each of the blend's components, which will depend on the specific current and rate, this component "feels" for the current state of charge, which as discussed earlier, will significantly fluctuate during the discharge. That alone will cause internal redistribution of lithium during relaxation, but this becomes much more relevant when one takes into account regenerative braking, a technology used in most of the modern EV's, which subjects the battery to charging pulses during vehicle deceleration. An example of such current profile, including both charge and discharge pulses is seen in Figure 6.2

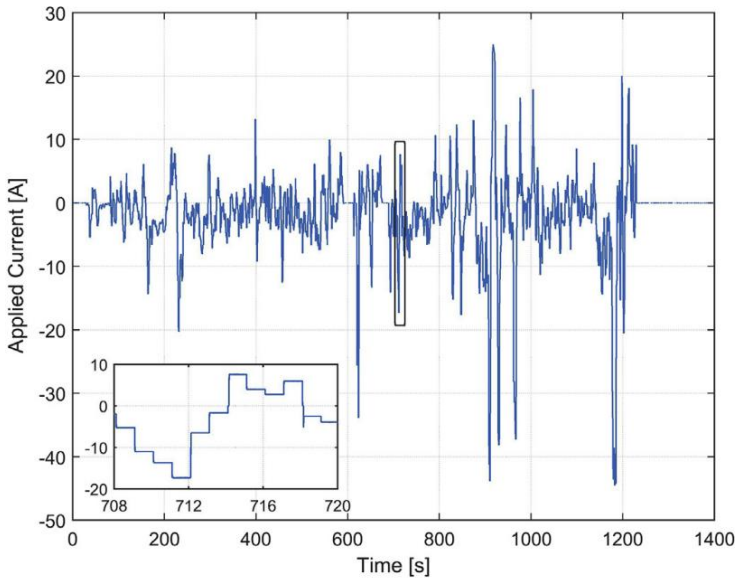

Figure 6.2: Example of battery current profile derived from an EV operating in an urban profile. [5]

Buffering of lithium takes place in positive blended electrodes but is also expected to happen in negative ones such as silicon-graphite, especially since, as discussed in

chapter 5, graphite is subjected to very high C-rates when a large amount of silicon is incorporated. This buffering, has already been witnessed in such systems[6] could potentially affect the overall performance of the electrode in pulse-like cycling. Operando XRD or XAS validation in silicon-graphite electrodes could help validating the existence and assess the extent of the observed phenomena in real electrodes. Overall, understanding lithium dynamics in both positive and negative blended electrodes in such real case scenarios could help in their design to improve both performance and lifetime in next generation lithium-ion batteries.

The present methodology can also be extended to alternative combinations of electrode materials, spanning different cell chemistries such as Na-ion.

References

[1] C. Heubner, T. Liebmann, C. Lämmel, M. Schneider, and A. Michaelis, "Insights into the buffer effect observed in blended lithium insertion electrodes," J Power Sources, vol. 363, pp. 311–316, 2017, doi: 10.1016/j.jpowsour.2017.07.108.

[2] A. P. Black et al., "Beam effects in synchrotron radiation based operando characterization of battery materials: XRD and XAS study of LiNi0.33Mn0.33Co0.33O2 and LiFePO4 electrodes.," Submitted for publication 2024.

[3] T. Jousseaume, J. F. Colin, M. Chandesris, S. Lyonnard, and S. Tardif, "How Beam Damage Can Skew Synchrotron Operando Studies of Batteries," ACS Energy Lett, vol. 8, no. 8, pp. 3323–3329, Aug. 2023, doi: 10.1021/acsenergylett.3c00815.

[4] C. Heubner, T. Liebmann, C. Lämmel, M. Schneider, and A. Michaelis, "Deconvolution of Cyclic Voltammograms for Blended Lithium Insertion Compounds by using a Model-Like Blend Electrode," ChemElectroChem, vol. 5, no. 3, pp. 425–428, Feb. 2018, doi: 10.1002/celc.201700997.

[5] T. Bruen and J. Marco, "Modelling and experimental evaluation of parallel connected lithium ion cells for an electric vehicle battery system," J Power Sources, vol. 310, pp. 91–101, Apr. 2016, doi: 10.1016/j.jpowsour.2016.01.001.

[6] C. Heubner, T. Liebmann, O. Lohrberg, S. Cangaz, S. Maletti, and A. Michaelis, "Understanding Component-Specific Contributions and Internal Dynamics in Silicon/Graphite Blended Electrodes for High-Energy Lithium-Ion Batteries," Batter Supercaps, vol. 5, no. 1, Jan. 2022, doi: 10.1002/batt.202100182.

7. Conclusions

The study of a wide set of binary blend electrodes consisting of 50:50 mixtures of different components, including $LiNi_{0.5}Mn_{0.3}Co_{0.2}O_2$ (NMC), $LiMn_2O_4$ (LMO), $LiFePO_4$ (LFP), and $LiFe_{0.35}Mn_{0.65}PO_4$ (LFMP) enabled assessing the influence of the voltage profile of the components in the extent and directionality of charge transfer between them, which is further shown to be dependent on the cell SoC and the operation temperature. The trends deduced from electrochemical experiments carried out using the decoupled blend setup were found to be in very good agreement with those derived from operando XRD on real blended electrodes in which the components are in physical contact, which evidences the representativity of this experimental approach.

Further research on NMC:LMO blends using the decoupled blend setup enabled to assess that the effective current load on each material greatly differs both as function of SoC and its relative amount. The component present in lower amount is subjected to a much higher effective current load resulting in higher electrochemical stress. This has also been confirmed through operando synchrotron diffraction and absorption experiments in real blended electrodes, which enable following the redox activity of each material, further showcasing the reliability and capability of the methodology developed within this PhD.

Blends containing a cobalt free, lithium rich layered oxide with formula $Li_{1.125}Ni_{0.312}Mn_{0.563}O_2$ with chemically delithiated active materials, namely $FePO_4$ and λ-MnO_2 were also studied, with the aim of the latter compensating for the first cycle irreversibility of the former, which is one of the handicaps for practical application. It was found that, due to the higher operation potential, blends with λ-MnO_2 resulted in direct reaction between the components. Yet, for the case of $FePO_4$, which operates at lower potential, this was not the case, and the redox mechanism was assessed by operando synchrotron X-ray diffraction. Aside enhanced first cycle coulombic efficiency, blending with $FePO_4$ was found to improve also thermal stability and capacity retention.

The decoupled blend setup was also used to study Si:graphite blends with 30% silicon, with significant differences in the effective rates on each component being observed between the lithiation and delithiation steps, which are not significantly affected by temperature. Moreover, and since fabricating electrodes with 100% silicon as active material proved challenging, the decoupled blend setup was used with pure graphite and the 30% blend as working electrodes, with the contribution of silicon being deduced by subtraction, which again showcases the usefulness of the protocols developed. In contrast to positive electrode blends, where components have more similar capacities, the substantial difference in capacity between graphite and silicon revealed significant disparities in the effective rates of each component. Therefore, another crucial factor in the rational design of blends is the capacity of the components. To achieve balanced rates within a blend, the component with the smaller weight fraction should ideally possess a higher specific capacity.

Overall, the findings reported in this PhD represent a step forward not only in the development of methodologies but also in the understanding of the behaviour of blended electrodes, which should contribute to their more rational design.